Facoltà di Ingegneria
Corso di Dottorato in Fluidodinamica
e Processi dell'Ingegneria Ambientale

Modeling the interaction of biomimetical slender structures with a fluid flow

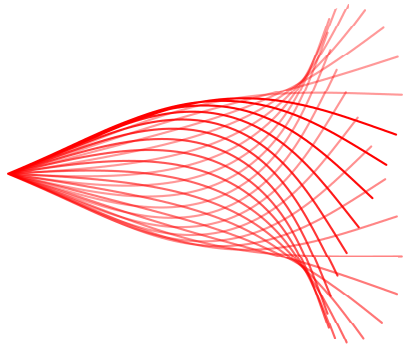

Thesis submitted for the degree of Doctor of Philosophy

Advisor:
Professor Jan O. Pralits

Candidate:
Damiano Natali

a.a 2014-2015

Modeling the interaction of biomimetical slender structures with a fluid flow

by

Damiano Natali

March 2015
Università degli Studi di Genova
Dipartimento di Ingegneria Civile,
Chimica e Ambientale
Via Montallegro 1, 16145 Genova, Italy

Tesi di Dottorato presentata pubblicamente lunedì 23 marzo 2015 alle ore 10.30 presso l'aula A9 della Facoltà di Ingegneria dell'Università degli Studi di Genova, via Montallegro 1, 16145, Genova.

To my family,
without whom nothing of this would have been possible

Abstract

Compliant and slender surface coatings are widespread in nature and commonly seen in practical applications. They have recently generated interest in the scientific community in that their features may promise interesting fluid dynamical performances.

The aim of this thesis is to explore numerically how different structural parameters of biological structures (mass, bending stiffness and permeability) affect the dynamics of these tissues when exposed to fluid flows.

In order to perform a numerical investigation a finite volume code in Matlab© has been developed. As for similar works, an Immersed Boundary (IB) approach has been exploited in order to efficiently handle elastic thin structures interacting with a viscous incompressible fluid.

The code has been tested on a hinged permeable filament flapping in an incoming uniform flow (commonly referred as the flag-in-the-wind problem). Results clearly point out the stabilizing effect of permeability on this particular type of slender structure, quantifying its effects on both the kinematics and dynamical behaviour of the filament.

Even though the code has been implemented to investigate permeability as a flow control parameter, other important applications can be tackled with the developed methodology. The first bio-engineering application has been found in the simulation of eye retinal detachment. In this case, the filament was clamped with a given angle to a moving plate simulating the eye rotation. Two different configurations were considered and compared in order to determine which case, and under what conditions, one is more prone to detach compared to the other.

Finally, the code was then exploited to investigate the dynamics of a spring-filament system similar to energy-harvesting devices. In this case, the filament was allowed to move just in the direction transversal to the flow and was connected by a spring to the equilibrium point. The aim of this study was to assess the optimal spring stiffness in order to trigger a resonant condition between the flapping of the filament and the spring itself, thus enhancing the efficiency of the device to extract energy from the flow.

Contents

1

Introduction

An object moving through a fluid is subject to an aerodynamic force arising from the fluid pressure distribution and friction between fluid particles and body surfaces. In aerodynamics it is common to decompose this force into two components: *drag* in the direction of body motion, and *lift* in the perpendicular plane.

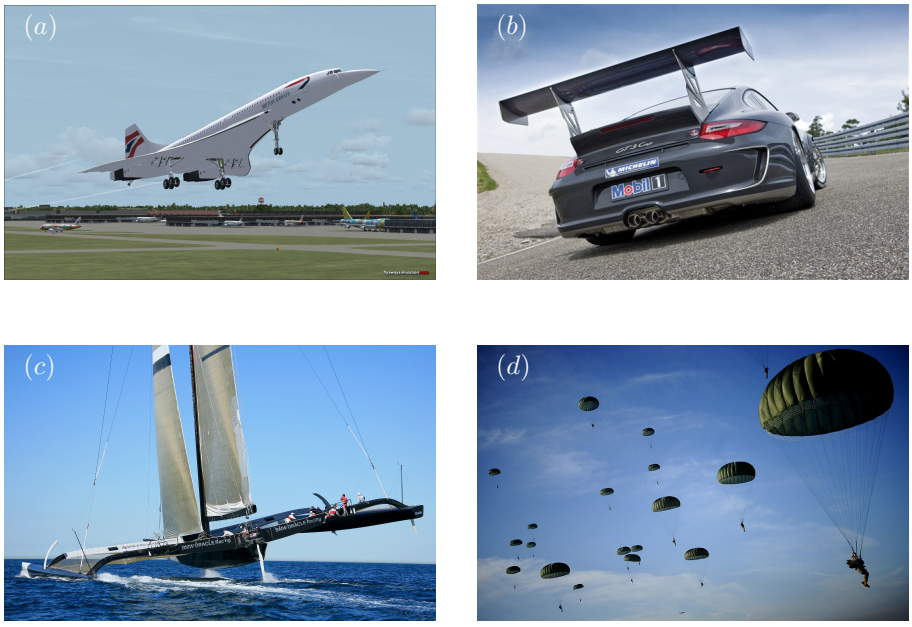

Figure 1.0.1: Aerodynamical forces in action: (a) airplanes take off thanks to the lift generated on wings, (b) the down-force on the spoiler helps racing cars adhere to the pavement, (c) hydrofoils contribute in raising the trimaran hulls out of the water, while (d) drag force helps the parachutist reaching a limited terminal falling velocity.

Lift and drag are important phenomena we all experience in everyday life (Figure 1.0.1): lift enables heavier-than-air airplanes to fly, helps better cornering in competitive cars creating enforce, and raises out of the water the hulls of racing trimarans. Lift is therefore considered a desirable effect.

On the other hand, drag is usually considered to be a negative effect: it reduces swimmers velocity in water, opposes the thrust of a car engine and causes bridges to collapse during floods. Nevertheless, without the terminal velocity of raindrops would be nearly fifty times faster, and in cases such as the functioning of parachutes drag turns out to be useful. However, in the majority of practical applications drag is something to be reduced in order to reduce fuel consumption or move faster.

1.1 History of Drag

Even though intuitive, a physical formulation of drag has been provided only recently, well after that of lift. Potential (or inviscid) theory of fluid motion (18^{th} century state-of-the-art) explains the lift force on asymmetric bodies but fails dramatically in predicting drag. In 1752 d'Alembert [1] proved that, against all experimental evidence, potential flow resulted in the prediction of zero drag on any non-lifting body (d'Alembert's paradox).

It took more than another century to provide a theoretical explanation for drag. The key idea was to look more closely at the body surface, where the fluid-solid attraction force is greater than that between the fluid particles, causing the velocity profile to have zero values with respect to the surface at the contact point (no-slip condition). The notion of *boundary layer* (Figure 1.1.1), a very thin region of fluid near a solid wall where velocity changes very quickly from the surface velocity to the free-stream velocity, was introduced by Prandtl in 1904 [2], and was a breakthrough. Prandtl's idea was to divide the flow into two regions: an inviscid outer flow region where potential theory still holds, and the boundary layer where viscous forces cannot be ignored.

Experimental evidence gives us a proportional relation between shear strain rate $\varepsilon_{ij} = \partial v_i / \partial x_j$ and shear stresses τ_{ij}. For example, Newtonian fluids are defined as those for which this dependence is linear, i.e.

$$\tau_{ij} = 2\mu\varepsilon_{ij},$$

where μ is the dynamical viscosity and is a characteristic of each fluid. Thus shear stresses are a consequence of the no-slip condition.

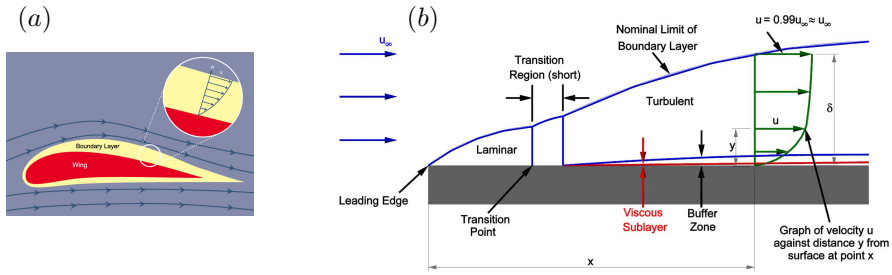

Figure 1.1.1: Schematic of boundary layer (in yellow) around a solid object (a), and boundary layer growing over a flat plate (b) with different regimes of flow (not in scale).

A stationary fluid exerts only normal pressure forces on the surface of an immersed body. Moving fluids, however, also exerts tangential shear forces on the surface because of the no-slip condition caused by viscous effects. Thus drag is, in general, due to the combined effects of pressure and wall shear forces. This comes down directly from the constitutive equation for fluids:

$$\sigma_{ij} = -p\delta_{ij} + \tau_{ij}$$

where p is the fluid pressure on the surface and τ_{ij} is called the deviatoric or viscous stress tensor.

The part of drag that is due directly to wall shear stress τ_{ij} is called *skin friction drag* since it is caused by frictional effects, and the part that is due directly to pressure p is called *pressure drag* (Figure 1.1.2),

$$F_D = F_{D,friction} + F_{D,pressure}.$$

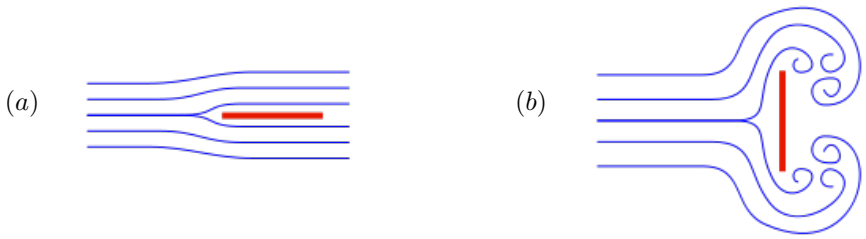

Figure 1.1.2: In the case of a flat plate aligned with the flow (a) the main part of the drag is due to friction, whereas in the case of plate perpendicular to the flow (b) the main part of the force is due to the pressure distribution around the plate.

Both skin friction and pressure drag depend upon geometrical configuration: the first one is proportional to the surface projection in the flow direction, while the second is mainly related to the frontal area (Figure 1.1.2). Therefore pressure is usually dominant for bluff bodies and small for streamlined bodies, where the friction drag prevails.

The d'Alembert paradox could eventually be explained in that potential theory does not satisfy the no-slip condition, ignoring skin drag completely. Indeed, potential theory could just predict lift and the part of drag related to pressure.

1.2 Flow control

The ability to actively or passively manipulate a flow field to effect a desired change can be numbered under the term of "flow control". In 1961 Flatt [3] defined flow control as "any mechanism or process through which the boundary layer of a fluid flow is caused to behave differently than it normally would". A particular control strategy is chosen based on the kind of flow and the control goal to be achieved. Flow-control goals are strongly, often adversely, interrelated, and there lies the challenge of making the tough compromises [41]. Typical goals of flow control are drag reduction, lift enhancement, enhancing mixing of mass, momentum or energy, suppressing the flow-induced noise, or a combination thereof. To achieve any of these end results, laminar-turbulent transition may have to be delayed or advanced, flow separation may have to be prevented or provoked, and finally turbulence levels may have to be suppressed or enhanced.

There are several possible classification schemes for flow-control methods. One is to consider energy expenditure: a control device can be active, requiring auxiliary power, or passive, requiring no further energy other than that required to generate fluid motion. Restricting the application field to drag reduction and passive control techniques, several strategies have so far been identified:

shaping the simplest method to control fluid flow around an aerodynamical surface involves the use of a suitably shaped body in order to manipulate the pressure distribution [10]. In order to postpone separation, favorable pressure gradient extends to the longitudinal location of the pressure minimum [41] (Figure 1.2.1, b),

riblets stream-wise microgrooves that act as fences to break up span-wise vortices in turbulent boundary layer and reduce the surface shear stress by

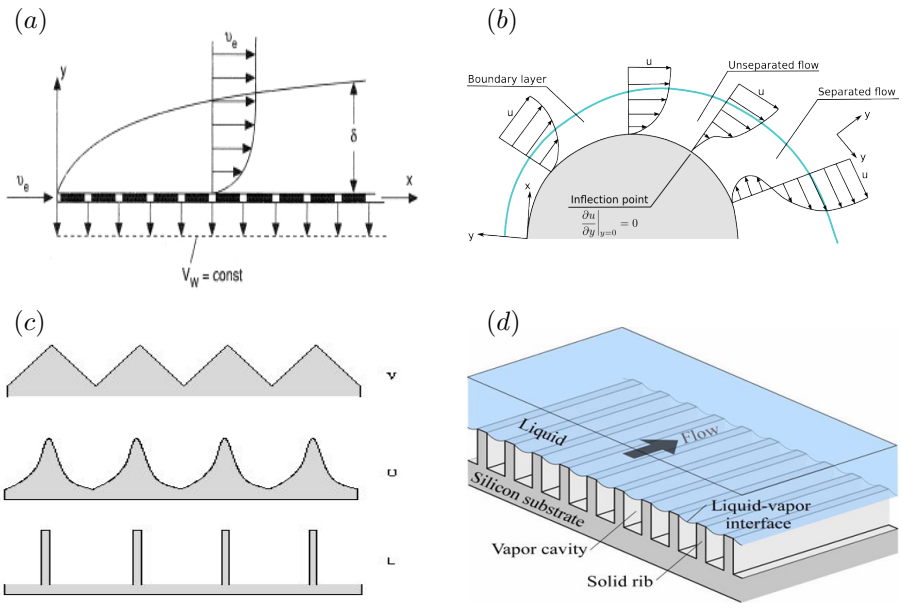

Figure 1.2.1: Different passive flow control techniques: suction surfaces for delaying transition (a), surface shaping for delaying boundary layer detachment (b), different riblet pattern (c) and super-hydrophobic surface (d).

preventing eddies from transporting high speed fluid close to the surface [42] (Figure 1.2.1, c),

turbolators A turbulent boundary layer is more resistant to separation than a laminar one, and mostly for that reason transition advancement may be desired in some situations [43]. The most common example is the single, multiple or distributed roughness elements (serrations, strips, bumps or ridges) typically placed near the airfoil's leading edge,

super-hydrophobic coatings to achieve super-hydrophobicity a surface must be structured so as to minimize the liquid-solid interactions. The crucial aspect is that of maintaining a layer of gas in between the rough wall and the liquid [17] (Figure 1.2.1, d). By hierarchically structuring the solid surface both at a micro and at a nano-scale, a sufficiently large *apparent* slip of the fluid at the wall can be achieved, thus reducing skin friction. Consider for example the micro-structure of a lotus leaf,

compliant surfaces flexible coatings whose modulus of rigidity is low enough so that surface waves are generated under the influence of the stress field in the fluid have lately drawn interest ([12, 13],for a more complete discussion, see [41], Chapter 7). The flow stabilization may be a result of altering the phase relation between the instantaneous stream-wise and normal velocity components in the viscous region, rather than changing the curvature of the mean velocity profile at the wall,

porous materials permitting flow by-pass from high- to low-pressure regions, thus modifying the pressure distribution in the near-wall region, opens new possibilities of boundary layer control, in particular where shock waves are expected [44]. This technique can be viewed as a passive suction in which mass is allowed to self-bleed, resulting in a reduced pressure gradient with delayed flow separation (Figure 1.2.1, a).

This thesis will focus on the last two items of the list, compliant surfaces and porous materials.

Some of these control techniques, such as suction, acoustic effects and plasma actuators come from the attempt to modify the fluid flow by mean of different physical phenomena. Others such as shaping, riblets, super-hydrophobic coatings and the introduction of foreign substances descend directly from the observation of nature, which provides numerous instances where drag reduction is essential for the survival of many species of avians and nektons. Here the basic assumption is that drag-reduction adaptations have evolved for improved efficiency of speed, or both, thereby aiding species survival in a Darwinian sense (for instance catching the prey or escaping from predators).

1.3 Biomimetics

Biomimetics is the field in which science seeks innovative solutions to real-life problems by taking inspiration from nature. The strength of this approach derives from the fact that every living organism has undergone a process of evolution over an extended period of time so that what we observe now is an optimized biological system whose structures and methods have adapted in order to optimize a particular or a set of different functionals.

To understand the difference between Biology and Biomimetics let us consider the well-known “flying machine” by Leonardo da Vinci. He would have been only a great biologist and painter if his admiration for the anatomy of birds and flight had only been confined to sketches and notes. His ingenious

and unconventional step was to depict "flying machines" which, he believed, would enable human beings to fly [4].

Biomimetical solutions can be found in several fields, with applications ranging from macro- to nano-scales. The Wright brothers [5] derived inspiration from observations of pigeons in flight, Swiss engineer Georges de Mestral [6] first conceptualized Velcro after removing several burdock burrs (seeds) remained stuck to his clothes and his dog's fur after returning from a hunting trip. Researchers studying a scanned a termite mound discovered a form of construction that could influence human building design [7]. Other interesting applications are the noise-reducing fuselage shape of the Bullet Train Shinkansen in Japan [9] and the application of the lotus effect [17] for realizing super-hydrophobic surfaces gifted with astonishing aerodynamical features.

Today more and more attention is devoted to biomimetical approaches to practical problems, both in academia and industry, where companies seeking new innovative products are looking at nature as an inexpensive Research and Development laboratory [8].

Human history has witnessed several cases of successful biomimetical approaches, however as pointed out in [16], two strong caveats have to be given in order to achieve a final working product. First, the environmental conditions in which the biological feature under consideration works may differ from those in which the designed device is supposed to operate, resulting in unexpected or unfavorable effects. Second, one has to be cautious about the evolutionary history of the morphology under consideration. Indeed, the investigated attribute may be simply "passed on" from ancestors without any specific significance. An indication of this situation is that where species sharing the same ancestors but living in different environments presents a similar feature. In this case the fact that the feature have evolved for one particular purpose is questionable. Another possible source of a biased perception is to expect only a single purpose for a biological feature, while multiple function is the rule in biology. For example we may be interested in the aerodynamical efficiency of a singularly shaped detail of an insect and realize only afterward that the feature was optimized for other functions, for example courtship or scaring predators. Thus, in the early stages of a biomimetical approach biologists can play a pivotal role by providing information on the evolutionary history and potential functional value of the biological morphology in question by conducting a comparative analysis of related species. In the case where this process is able to exclude other reasons, the morphology in question is likely to have a functional value in view of application to engineering systems [16].

Examples of fluid-dynamical biomimetical approaches are countless (Figure 1.3.1): the simple observation of how different species of avians and nektons

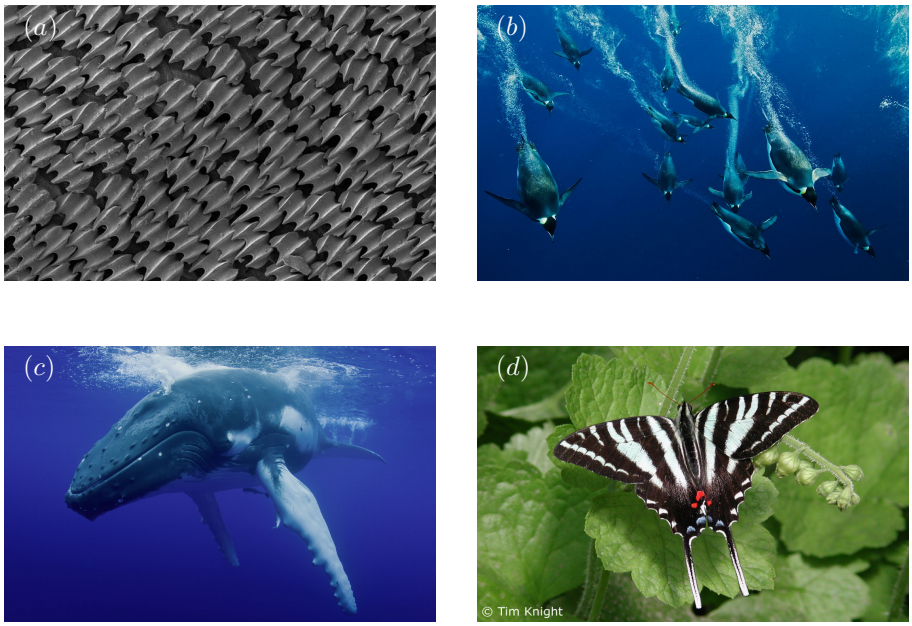

Figure 1.3.1: Shark dermal denticles arranged in in the flow direction (a), penguins surrounded by water bubbles (b), humpback whale with characteristic pectoral flippers (c) and the hindwing tails of the swallowtail butterfly (d).

control the flow around their body has provided inspiration for many applications affecting everyday life. Observation of dermal denticles of shark skin (Figure 1.3.1 (a)) took to the first application of riblets on the hull of the winner of the 1987 America's Cup yacht race, the *Star and Stripes* [41]. A video-documentation of swimming penguins clearly shows that penguins (Figure 1.3.1 (b)) exhale air before emerging at high speed from the sea. Exhaled bubbles then agglomerate around the body and remain there for several seconds [18]. Following this and other examples a lot of research is currently active in the field, mainly for the purpose of reducing the skin friction of maritime transports [19, 20]. The occurrence of "morphological complexity" in biologic surfaces can suggest a specialized shape adaptation for improved aerodynamical performances. The humpback whale flipper presents peculiar protuberances (or *tubercles*, Figure 1.3.1 (c)) located on the leading edge. CFD (Computational Fluid Dynamics) simulations [15] showed that, for regions downstream of the tubercle crest, separation was delayed almost to the trailing edge. The property of delaying stall to higher angles of attacks may explain the ability

of this kind of whale to perform such acrobatic underwater maneuverings, and it is why WhalePower [21], a venture based in Toronto, has begun integrating tubercles into the leading edges of wind-turbine and fan blades. In addition the shape of the trailing edge greatly affects the aerodynamical performance. Swallowtail butterflies (Figure 1.3.1 (d)), unlike other related species, have distinct tail-projections on the hind wings that have drawn researches' attention [16]. The aerodynamical effects of these appendages in gliding flight was investigated for their ability to keep the wing-tip vortices outboard. Further examples of intriguing biological features and their fluid-dynamical analysis can be found in [16, 11, 14, 17].

1.4 Aim of the work

The aims of this thesis are:

1. Design a numerical algorithm to take into account permeability in addition to other structural parameters (mass and bending stiffness) for which different strategies have already been proposed in several works [50, 52, 55, 66, 68].

   As for similar works, an Immersed Boundary (IB) approach has been exploited in order to handle efficiently moving objects interacting with a viscous incompressible fluid. The IB approach has a long history in modeling bio-fluidodynamical phenomena involving slender and compliant structures as it was introduced by Peskin [50] in the early 1970s to model blood flow in the heart and through heart valves. The IB formulation avoids the need for creating body-fitted meshes by making use of an Eulerian description for the fluid and a Lagrangian for the object. The two descriptions are linked together by a smoothed approximation of the Dirac Delta function.

   In order to capture the essential evolution of the phenomena while maintaining a moderate level of complexity and not involving huge computational power, the developed code considers 1-d structures and 2-d fluid flows. Such a configuration is a good representation of the physical phenomena we want to model: a slender compliant structure such as hair, a feather, or an appendage, interacts with a fluid flow that is assumed to have no variation in the third direction. The same consideration is valid for the structure: its configuration will be constant in the direction normal to the 2-d domain. Thus, three-dimensional effects cannot be taken in consideration with the present code.

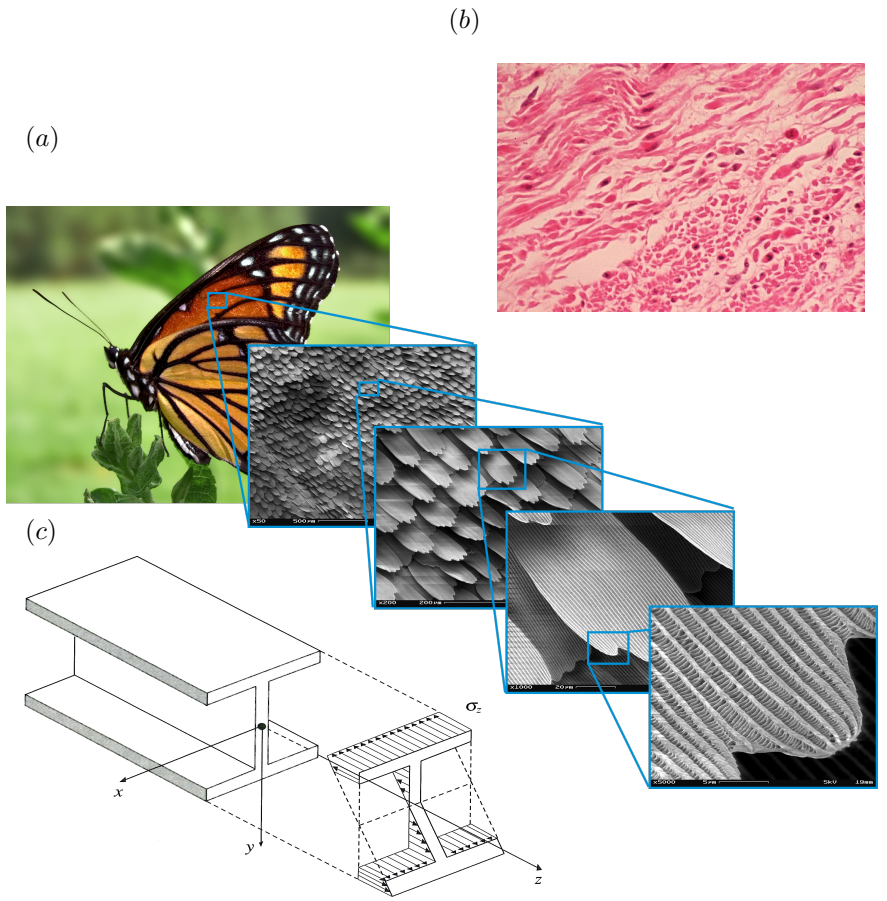

Figure 1.4.1: (a) Zoom on the wing scales of a Viceroy butterfly with clearly visible porous structures, (b) smooth muscle tissue, (c) solid stresses σ_z on the cross-section of a deformed beam. Note that the configuration of the deformed cross-section is planar, thus $\varepsilon_z = -y/R$.

2. Investigate numerically the aerodynamical performances of surfaces exhibiting properties similar to biological tissues: mass, bending stiffness and permeability.

   Throughout the work, the following mechanical properties of the surface will be taken into account:

mass per unit volume, or density, of surfaces will be considered in this work. Biological tissues exhibit different features depending on whether they belong to animals or plants and on their function and location. Contrary to this complex classification, from a mechanical point of view tissues are uniquely characterized by their density and elastic modulus. In order to estimate tissue density we look at its basic component, the cell, whose mass is composed of 70% water, more or less independently from what tissues it belongs to. Thus, it is quite common that biological tissues in water can be considered *neutrally buoyant*, i.e. with the same density of the surrounding fluid. This particular condition has important aftermath on the structural inertial term.

bending stiffness is not a material property, but it is defined for 1 and 2-d elements in order to model the third dimension effects. In the 1-d elastic string theory bending stiffness is derived from the elastic (or Young) modulus E, characteristic of the material:

$$M = \int_A \sigma_z y dA = -\frac{E}{R}\int_A y^2 dA = E\chi \int_A y^2 dA = EI_x\chi \qquad (1.4.1)$$

where A is the cross-section of the 1-d element, $\chi = -1/R$ is the local curvature, R is the curvature radius and $\int_A y^2 dA$ is the second moment inertia term of section A around x axis (cfr. Figure 1.4.1, (c)). In Equation 1.4.1, the constitutive relation $\sigma_z = E\varepsilon_z$ (with σ_z solid stresses and ε_z solid deformations) and the hypothesis of planar faces $\varepsilon_z = -y/R$ has been used.

permeability i.e. the ability of a medium to permit a fluid flow through it, comes into play in a wide variety of fields (e.g. earth science, medicine, biology, chemistry) as a consequence of voids in a solid matrix and a driving fluid pressure gradient. Ground-water flows get enriched by minerals through fractures in rock formations and blood undergoes filtration through the glomerular basement membrane of the kidneys thanks to filtration slits between cells [22, 24].

Besides tissue mass and bending stiffness, which has been extensively investigated in the literature using similar tools [66, 68, 55, 52], the novelty of this work is to take into account also the mass transfer through the connective voids of biological tissue.

Nowadays several practical issues have been solved by a biomimetical strategy involving permeability. Many chemical reactors take advantage of the permeability of some particular media in order to maximize surface area contact between fluid and solid and highways are covered with

permeable paving to maximize the asphalt drying rate. Moreover, permeability plays a central role in membrane technology, widely used in the food technology, biotechnology and pharmaceutical industries to selectively separate different components based on their size or electric charge [23].

Despite previous examples, in which permeability has been exploited for different purposes, the aim of the present work is to shed some light on how surface permeability affects aerodynamical performances.

3. Develop new control strategies borrowed from biology to significantly enhance aerodynamical performances.

   Slender and compliant bodies subject to an incoming flow exhibit a peculiar control strategy for delaying boundary layer detachment that can be defined as *self-streamlining*, ascribable to the compliant structure strategies. This feature is inherently passive in that the structure has the freedom to adapt automatically to changes in the flow. Of course, this capability depends on its inertia (mass) and bending stiffness. Intuitively, the higher the mass the longer will be the time interval in which the structure will react to changes in the flow. On the other hand, more rigid structures (i.e. higher bending stiffness) will be able to communicate local changes to the rest of the structure. While the effects of mass and bending stiffness form a well-established frame in the literature of fluid-structure interaction, the current thesis also accounts for the permeability of tissues, thus paving the way to other types of boundary layer control. By permitting a mass flow from high- to low-pressure regions the pressure distribution on the surface can be modified, thus enhancing its aerodynamical stability.

4. Realize a numerical code for the simulation of the interaction between slender structures, not necessarily permeable, and incompressible fluid flows.

   A wide range of real-world phenomena, from paper production technology to bridge construction to prosthetic heart valves, not including natural processes, exhibits slender structures interacting with a fluid force (Figure 1.4.2). Our aim is to develop a generic numerical code environment that can efficiently handle this kind of problems due to the Immersed Boundary approach.

The previously listed aims will take shape in the applications described in Chapter 6. In particular, the first application refers to the simulation of a hinged permeable filament flapping in an incoming uniform flow (commonly referred as

Figure 1.4.2: Examples of slender structures interacting with a fluid flow: prosthetic heart valves (a), cable-stayed bridge (b), wind turbine (c) and dragonfly flight (d).

the flag-in-the-wind problem), which is characterized by mass, bending stiffness and permeability. In this case the main focus was the effect of permeability regarding both the stability and the flapping dynamics. The second application regards the simulation of two different types of retinal detachment, a common pathology of the eye, in order to determine which one is more prone to further detachment. Finally, in the third application, we simulate a simple model of an energy harvesting device, trying to find the best parameter set (mass, bending stiffness and spring stiffness) in order to maximize the oscillations of the filament and thus energy extraction.

1.5 Structure of the thesis

For better readability, contents of this work has been subdivided into five modular chapters. Chapter 2 will introduce the main concepts of fluid structure interaction (FSI), while in Chapter 3 the governing equations of incompressible fluid flow will be presented along with the fractional step method, the numerical algorithm used to achieve the pressure-velocity coupling. The immersed boundary (IB) approach will be treated in detail in Chapter 4. Chapter 5 describes the implementation of a finite volume (FV) code for the direct numerical simulation (DNS) of the interaction between a fluid flow and an elastic body. Finally, code applications and numerical results will be presented and discussed in Chapter 6.

2

Fluid Structure Interaction

Fluid-structure interaction (FSI) problems arise every time a fluid flow impacts on a body surface. Depending both on the body's structural parameters and on the resolution of our study, we may want to consider the deformations of the body. These deformations, in turn, will simultaneously change both the domain and the boundary conditions of the fluid flow. Thus, a simulation that could have easily been achieved with, at most, an unsteady flow solver on a fixed domain, now requires a solver capable of simultaneously handling both structural deformations and mesh motion.

The first studies of FSI trace back to Aeroelasticity, defined by Arthur Roderick Collar [45] in 1947 as "the study of the mutual interaction that takes place within the triangle of the inertial, elastic, and aerodynamic forces acting on structural members exposed to an airstream, and the influence of this study on design."

As with every engineering discipline, FSI was both born and developed by the time people realized it was needed to solve such a problem. In particular, at the beginning of the XIX century, current technologies were ready to allow humans to fly with the first airplanes. At that time nobody knew that when a slender and flexible structure (as an aircraft wing) is subject to a fluid flow they begin to interact. Depending on the parameters, for instance the flow velocity or wing bending stiffness, this interaction can be damped or amplified, leading to catastrophic effects. The second failure of Samuel Langley's prototype plane on the Potomac has been attributed to aeroelastic effects (specifically, torsional divergence), the same as those that plagued aircraft during the First World War. As a first approximation, these problems were solved largely by trial-and-error and ad-hoc stiffening of the wing, but FSI reason for existence was outlined. In 1926 Hans Reissner published his theory of wing divergence, leading to a significant amount of further theoretical research on the subject. In the 1970's predictions of flutter and other similar aeroelastic phenomena were required in the aerospace field. Since then FSI has been successfully applied to a vast range of applications, including civil engineering (bridges and suspended cables) [25, 26, 27, 74], process engineering (nuclear reactor steam generator tube bundles, rotor dynamics, singing hydrofoils) [28, 29, 30, 31], shape optimization studies [32, 33] and a vast number of biomedical applications (arterial blood

flow, aortic heart valves, heart and ventricle, lung modeling, aortic aneurysms, snoring treatment) [34, 35, 50, 36, 37, 38, 39].

2.1 Resonance

Before discussing resonance, let us give the definition of natural frequency as the frequency at which an ideal system (i.e. with no damping) tends to oscillate in the absence of any driving force.

Mathematically speaking, natural frequencies correspond to the eigenvalues of the system matrix. Eigenvalues and eigenvectors can indeed be thought of as frequencies and modes of the free response to the initial condition of an unforced dynamical system. This can be seen in the following example.

With respect to Figure 2.1.1 we can write the dynamical equation as

$$\begin{cases} m_1\ddot{x}_1 + k_1x_1 - k_2(x_2 - x_1) = 0 \\ m_2\ddot{x}_2 + k_2(x_2 - x_1) = 0 \end{cases}, \tag{2.1.1}$$

by introducing vector $\mathbf{x} = [x_1\ x_2]^T$ we can write (2.1.1) in matrix form

$$\begin{bmatrix} m_1 & 0 \\ 0 & m_2 \end{bmatrix} \ddot{\mathbf{x}} = - \begin{bmatrix} k_1 + k_2 & -k_2 \\ -k_2 & k_2 \end{bmatrix} \mathbf{x}. \tag{2.1.2}$$

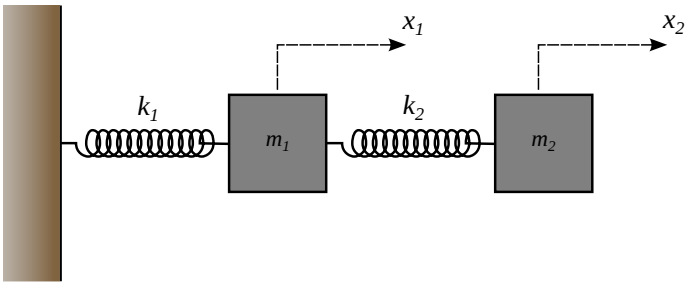

Figure 2.1.1: Dynamical system made up of two masses m_1 and m_2 linked by springs of different elastic constant k_1 and k_2 to an external wall.

The system's dynamical equation can be written $M\ddot{\mathbf{x}} = -K\mathbf{x}$. We now assume harmonic motion, i.e. that both masses oscillate with same frequency ω albeit different amplitudes $\mathbf{A}$, and write

$$\mathbf{x} = \mathbf{A}\ \exp(i\omega t), \tag{2.1.3}$$

from which we obtain

$$(K - \omega^2 M)\mathbf{A} = 0.$$

This is an eigenvalue problem for the eigenvalue ω_N (natural frequencies) and corresponding eigenvector $\mathbf{A}_N$ (natural modes). We note that discrete systems (such as the one under consideration) having N degrees of freedom, have N natural frequencies and N natural modes, that become infinite in continuous systems.

The above tells us that if we start our dynamical system from the initial condition $\mathbf{A}_N$, both masses will evolve periodically as stated in (2.1.3) with the frequency ω_N corresponding to $\mathbf{A}_N$. For a generic initial condition (2.1.3) will still hold but all frequencies and modes will come into play. In particular, as the initial condition can be seen as a linear combination of natural modes $\mathbf{A}_N$ (eigenvectors), system oscillations will be ruled by a linear combination of the corresponding natural frequencies ω_N (eigenvalues).

In general resonant frequencies ω_R and natural frequencies ω_N are not the same, since natural frequencies depend only on system parameters (i.e. the structure), while resonant frequencies also take into account the coupling with the forcing system (i.e. the fluid flow). For example, fluid flow around the wing also introduces some viscous damping in the dynamics that makes in general $\omega_R \neq \omega_N$. However, when damping is negligible the resonant frequency ω_R is approximately equal to the natural frequency of the system ω_N.

Resonance is the state of a system forced at particular frequencies, known as resonant frequencies ω_R, in which its oscillations are greater with respect to other frequencies. Specifically, a periodic driving force at a resonance frequency produces larger amplitude oscillations compared to any other frequency, no matter the magnitude of that force.

To evidence the latter, let us consider an ideal dynamical system (no damping) driven by an external periodic force. After a transient, its oscillation frequency coincides with the driving force frequency. Let us consider now the oscillation amplitudes.

Let us derive the law of motion for the unforced system (Figure 2.1.2, left). By assuming an ideal behaviour (i.e. without considering friction), its dynamical equation reads

$$m\ddot{x} = -kx.$$

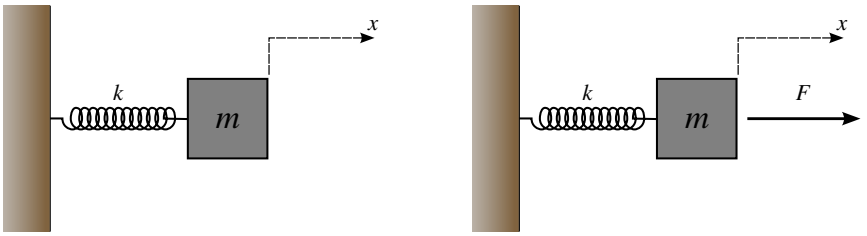

Figure 2.1.2: Unforced (left) and forced (right) spring-mass system.

As $x = 0$ is a stable fixed point, in order to trigger the motion we have to initially displace the mass. By making the following Ansatz:

$$x = A\cos(\omega_N t),$$

(where A is the mass initial displacement) we obtain

$$\omega_N = \sqrt{\frac{k}{m}},$$

where ω_N is the system natural frequency, i.e. the characteristic frequency at which it oscillates naturally, without being forced.

Now let us consider the forced system (Figure 2.1.2, right), whose dynamical equation reads

$$m\ddot{x} = -kx + F,$$

where the driving force F is assumed to be periodic with an imposed frequency ω_F:

$$F = F_0\cos(\omega_F t).$$

In this case, as stated above, the system will oscillate with the same frequency ω_F:

$$x = A\cos(\omega_F t),$$

from which we obtain

$$-Am\omega^2\cos(\omega t) = F_0\cos(\omega t) - kA\cos(\omega t)$$

and

$$A = \frac{F_0}{(k - m\omega^2)} = \frac{F_0}{m(\omega_N^2 - \omega_F^2)}$$

stating that when the forcing frequency ω_F approaches the system natural frequency ω_N, the oscillation amplitude $|A|$ diverges (Figure 2.1.3).

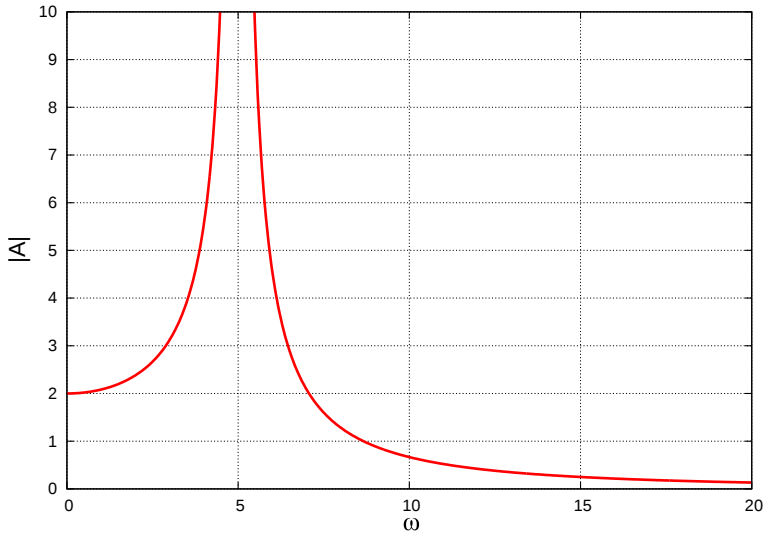

Figure 2.1.3: Theoretical oscillation amplitude magnitude as a function of the imposed driving force frequency ω_F. The peak in correspondence of natural frequency ω_N is clearly visible.

However, this theoretical prediction of oscillation amplitudes does not include energy dissipations and other forms of energy present in real-world phenomena and that avoid amplitude to diverge, even if a maximum is always present.

2.2 Flag-in-the-wind problem

The flag-in-the-wind problem has been studied theoretically, numerically and experimentally as the paradigm for the instability of an elastic structure subject to a fluid flow. This phenomenon, known as flutter, is caused by a positive feedback between the body's deflection and forcing exerted by the fluid flow. A wide spectrum of forcing frequencies are triggered by the uniform flow affecting the body, which begins to resonate when its own natural frequency has been excited.

Despite its simplicity, the system's dynamics is very rich (Figure 2.2.1): an elastic one-dimensional boundary is tethered at one end in a two-dimensional laminar flow, moving at the local velocity and exchanging forces with the surrounding fluid. Vortices are shed from the free end of the filament, transported

downstream by the flow, and are diffused by viscosity in the vortex street. As a result, the long-term motion of the filament can result both in a fixed-point stability, a limit-cycle flapping or a chaotic motion, depending on the governing parameters of the system.

Starting from Rayleigh's first theoretical approach in 1879 [65] involving the evolution of a two-dimensional vortex sheet, the stability of the flag has been enriched by inertial and structural mechanical properties and has composed one of the main subjects in the study of theoretical aeroelasticity [71, 73, 74, 75].

More recently, increasingly accurate numerical studies (most of all using an immersed boundary approach) have come to support analytical results. In particular, Zhu and Peskin [66] first pointed out the important role of length and mass on the onset of flapping, and described the bistable behavior of the flapping. Both Kim and Peskin [55] and Huang *et al.* [52] developed methods to handle massive filaments in a more efficient way. The first numerical study taking into account permeability was by Kim and Peskin [68], in which the dynamics of a massless 2-d parachute not resisting bending was investigated. Despite simplifications, the stabilizing role of permeability has been fully addressed. In the present work, we propose an innovative way for handling simultaneously permeability and bending resistance and mass which overcomes some of the major drawbacks of previous methods (see Section 4.4). A more complete report on the efforts in shedding light regarding the dynamics of slender interacting body with fluid flows may be found in Shelley and Zhang [76].

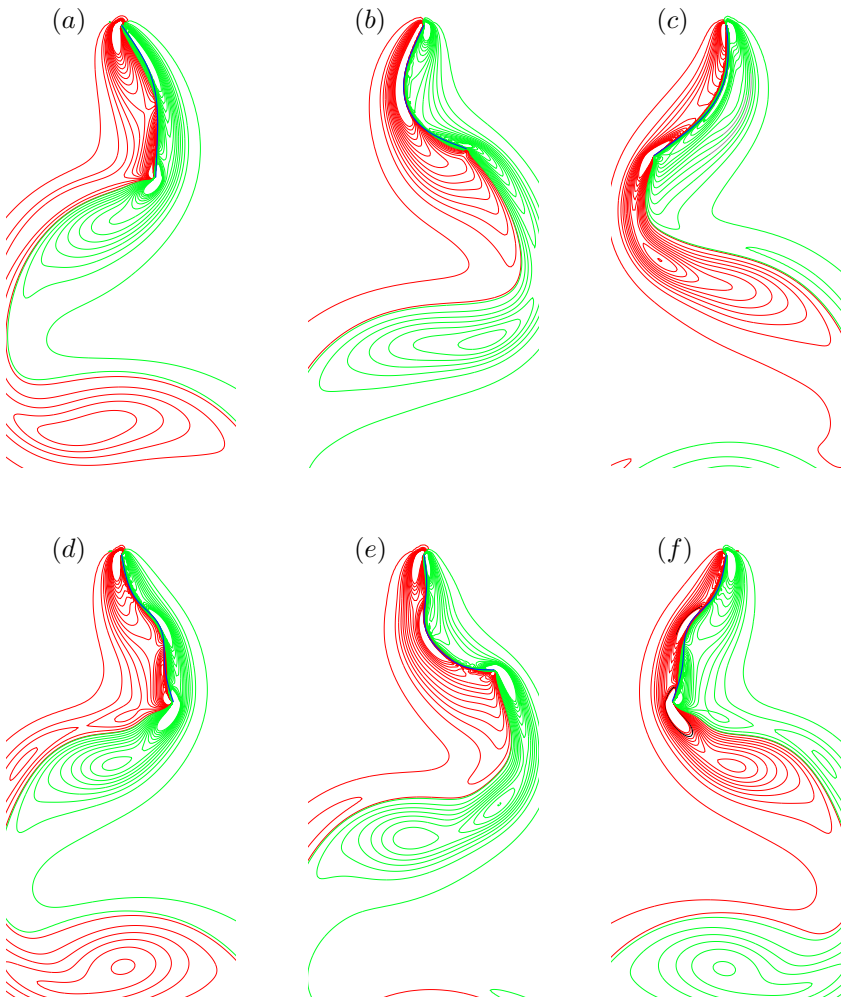

Figure 2.2.1: Vorticity iso-contours around impermeable flapping filament (in blue) at $Re = 200$ obtained with the code presented in Section 6.1. Positive vorticity are shown in red, negative in green. (a), (b) and (c) correspond to case A depicted in Figure 6.1.2, while (d), (e) and (f) refer to case B.

In order to study the time-dependent behavior of the fluid-structure coupled system, it is useful at this point to inspect the governing equations of the solid structure. Without considering the complete equations of solid mechanics we can take advantage of the fact that slender structures such as those considered here (a hair, a feather, an appendage) usually have one dimension prevailing over the others. Therefore, we can resort to the classical beam theory which describes the dynamical behavior of a beam endowed with bending stiffness and subject to a given external load.

2.3 The Euler-Bernoulli beam theory

Let us consider a 1-d beam subject to an external load $\mathbf{F}(s)$ (Figure 2.3.1, a). For engineering applications it is useful to derive an equation for the evolution of its geometrical configuration $\mathbf{X}(s)$, where s is the curvilinear abscissa.

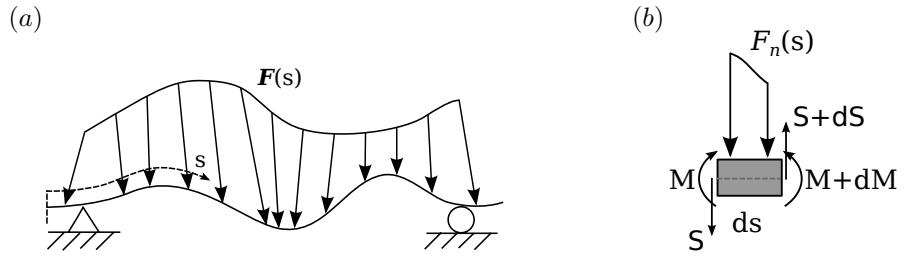

Figure 2.3.1: 1-d beam with a distributed load $\mathbf{F}(s)$ along its axis (a) and an infinitesimal element of the beam with its internal strains S and torque M(b).

We may want to consider the local normal $\mathbf{n}$ (sometimes called *curvature vector* in that it points towards the local curvature center) and tangent $\boldsymbol{\tau}$ unit vector (Figure 4.3.1), defined as

$$\boldsymbol{\tau} = \frac{\partial \mathbf{X}}{\partial s} = \phi, \quad \mathbf{n} = \frac{\frac{\partial \boldsymbol{\tau}}{\partial s}}{\left\| \frac{\partial \boldsymbol{\tau}}{\partial s} \right\|} = \frac{\frac{\partial^2 \mathbf{X}}{\partial s^2}}{\left\| \frac{\partial^2 \mathbf{X}}{\partial s^2} \right\|}$$

$\mathbf{n}$ and $\boldsymbol{\tau}$ are perpendicular to each other and, together with the binormal vector $\mathbf{b}$ (in the 3-d world) form the so-called *Frenet-Serret* or *TNB frame* (Figure 2.3.2).

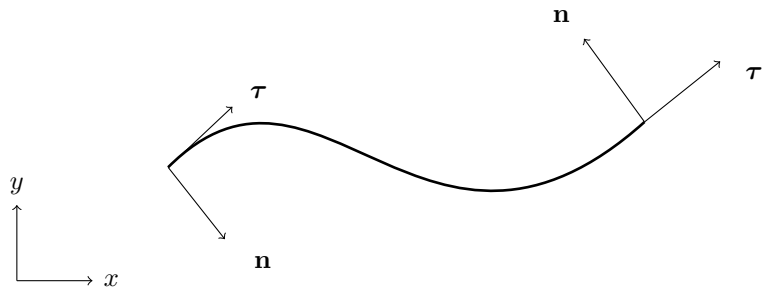

Figure 2.3.2: Local tangential $\boldsymbol{\tau}$ and normal $\mathbf{n}$ unit vectors. By definition N and T reactions are aligned with these vectors.

Usually engineers are interested in beam displacements perpendicular to its axis ($\mathbf{n}$ direction). Under the assumptions of small deformations, the normal and perpendicular problems can be decoupled. Thus, by imposing the translational and rotational equilibrium for an infinitesimal element perpendicularly loaded (Figure 2.3.1, b) and neglecting higher order infinitesimal contributions, we get the following:

$$dS = F_n(s)ds \quad ; \quad dM = -Sds$$

from which

$$\frac{dS}{ds} = F_n(s) \tag{2.3.1}$$

$$\frac{dM}{ds} = -S \tag{2.3.2}$$

Assuming that plane sections conserve their planarity and are normal to the deflected beam axis, we can express the moment M as a function of the curvature κ:

$$M = \gamma\kappa = \gamma\frac{\partial\phi}{\partial s} = -\gamma\frac{\partial^2 X_n}{\partial s^2} \tag{2.3.3}$$

where the bending stiffness $\gamma = EI$ with I moment of inertia of the beam's cross-section, E the Young modulus, κ is the curvature and ϕ is the angle of rotation of the section (defined as $\phi = -\partial X_n/\partial s$). By gathering equations (2.3.3)-(2.3.2) we can write

$$F_n(s) = \gamma\frac{\partial^4 X_n}{\partial s^4}, \tag{2.3.4}$$

which is called the *static beam equation*. In order to obtain the *dynamical beam equation* we simply add the inertial term $\partial^2 X_n/\partial t^2$:

$$\frac{\partial^2 X_n}{\partial t^2} = -\gamma\frac{\partial^4 X_n}{\partial x^4} + F_n(s) \tag{2.3.5}$$

So far we made the hypotesis of *small deformations*, i.e. that the beam displacement from the initial (undeformed) configuration are small enough not to consider the normal reaction (aligned with the beam axis) into the equation for the displacement perpendicular to the axis. When this hypothesis is no more acceptable we have to take into account also the normal reaction (i.e. tension) N. In vectorial form, equation (2.3.5) becomes

$$\frac{\partial^2 \mathbf{X}}{\partial t^2} = \frac{\partial}{\partial s}\left(N\frac{\partial \mathbf{X}}{\partial s}\right) - \gamma\frac{\partial^4 \mathbf{X}}{\partial s^4} + \mathbf{F} \tag{2.3.6}$$

We can write (2.3.6) as

$$\frac{\partial^2 \mathbf{X}}{\partial t^2} = \frac{\partial}{\partial s}\left(N\frac{\partial \mathbf{X}}{\partial s}\right) - \frac{\partial^2}{\partial s^2}\left(\gamma\left\|\frac{\partial^2 \mathbf{X}}{\partial s^2}\right\|\frac{\frac{\partial^2 \mathbf{X}}{\partial s^2}}{\left\|\frac{\partial^2 \mathbf{X}}{\partial s^2}\right\|}\right) + \mathbf{F},$$

thus, using the previous definitions of the TNB frame,

$$\frac{\partial^2 \mathbf{X}}{\partial t^2} = \frac{\partial}{\partial s}\left(N\boldsymbol{\tau}\right) - \frac{\partial^2}{\partial s^2}\left(M\mathbf{n}\right) + \mathbf{F}$$

$$\frac{\partial^2 \mathbf{X}}{\partial t^2} = \frac{\partial}{\partial s}\left(N\boldsymbol{\tau}\right) - \frac{\partial}{\partial s}\left(\frac{\partial M}{\partial s}\mathbf{n} + \frac{\partial \mathbf{n}}{\partial s}M\right) + \mathbf{F}$$

$$\frac{\partial^2 \mathbf{X}}{\partial t^2} = \frac{\partial}{\partial s}\left(N\boldsymbol{\tau}\right) - \frac{\partial}{\partial s}\left(T\mathbf{n} - \gamma\kappa^2\boldsymbol{\tau}\right) + \mathbf{F}$$

$$\frac{\partial^2 \mathbf{X}}{\partial t^2} = \frac{\partial}{\partial s}\left(N\boldsymbol{\tau}\right) - \frac{\partial}{\partial s}\left(T\mathbf{n}\right) + \mathbf{F} \tag{2.3.7}$$

that represents the dynamical equation for a beam (if $N \gg \gamma\kappa^2$).

Let us recover now the classical equilibrium equations of Solid Mechanic textbooks. From equation (2.3.7) we get

$$N\frac{\partial \boldsymbol{\tau}}{\partial s} + \boldsymbol{\tau}\frac{\partial N}{\partial s} - T\frac{\partial \mathbf{n}}{\partial s} - \frac{\partial T}{\partial s}\mathbf{n} + \mathbf{F} = 0$$

From the Frenet-Serret formulas we have

$$\frac{\partial \boldsymbol{\tau}}{\partial s} = \kappa\mathbf{n}, \quad \frac{\partial \mathbf{n}}{\partial s} = -\kappa\boldsymbol{\tau}$$

where κ is the curvature. So by substitution we get

$$N\frac{\partial \phi}{\partial s}\mathbf{n} + \boldsymbol{\tau}\frac{\partial N}{\partial s} + T\frac{\partial \phi}{\partial s}\boldsymbol{\tau} - \frac{\partial T}{\partial s}\mathbf{n} + \mathbf{F} = 0 \tag{2.3.8}$$

Equation (2.3.8) is vectorial. If we decompose it into the parallel and perpendicular components we get

$$\begin{cases} \dfrac{\partial N}{\partial s} + T\dfrac{\partial \phi}{\partial s} + F_\tau = 0 \\ \\ N\dfrac{\partial \phi}{\partial s} - \dfrac{\partial T}{\partial s} + F_n = 0 \end{cases} . \tag{2.3.9}$$

2.4 Beam dynamical analysis

Studying the beams natural modes of oscillation corresponds to finding the solution to the dynamical beam equation without the forcing term:

$$\frac{\partial^2 v}{\partial t^2} = -\gamma \frac{\partial^4 v}{\partial x^4}$$

We can solve this equation with the separation of variables technique, i.e. by supposing $v(s,t) = A(s)B(t)$, where $A(s)$ takes into account the spatial and $B(t)$ the temporal behavior of the beam. By doing so we can write

$$AB^{II} = -\gamma A^{IV} B,$$

and by dividing both members by AB we get

$$\frac{B^{II}}{B} = -\gamma \frac{A^{IV}}{A}.$$

where superscripts denote derivatives. Since the left-hand side does not depend on s and the right-hand does not depend on t both terms are constant. Let us name it c and use the temporal equation to discuss its sign:

$$B^{II} - cB = 0$$

This will result in an exponential function if $c > 0$, sinusoidal if $c < 0$, so we look at solutions for which $c < 0$. Since the system will oscillate with frequency $\sqrt{-c}$, we will replace c with $-\omega_N^2$, because they are the beam's natural frequencies. We can now focus on the equation leading to the spatial solution $A(x)$:

$$A^{IV} - k_N A = 0$$

where $k_N^4 = \omega_N^2/\gamma$. The general solution of this equation is a linear combination of trigonometric functions:

$$A(s) = C_1 \cos(k_N s) + C_2 sin(k_N s) + C_3 \cosh(k_N s) + C_4 sinh(k_N s) \tag{2.4.1}$$

where the constraints C_i are derived from the imposed boundary conditions from the particular physical problem.

In the following paragraphs we will investigate two configurations in which the beam is often found in practical applications, the clamped and the hinged beam. Thus, equation (2.4.1) will be specialized for the particular boundary conditions. Theoretical results from the next paragraphs show good agreement (see Paragraph 5.5.5) with the numerical outcome from the numerical code described in Chapter 5.

2.4.1 Clamped beam

The clamped beam (also known as cantilever) is a beam with a free end where no constraints are applied, so that it can freely deflect and rotate, and an anchored end with zero prescribed displacement and rotation. In this case the boundary conditions are the following:

- no displacement at the fixed end, i.e. $A(0) = 0$;
- no rotation at the fixed end, i.e. $A^I(0) = 0$;
- zero torque at the free end, i.e. $A^{II}(L) = 0$, see eq. (2.3.3);
- zero shear at the free end, i.e. $A^{III}(L) = 0$, see eqs. (2.3.3) and (2.3.2);

From these boundary conditions we can write a system of four equations for the four constants in (2.4.1). Since this system is homogeneous, the only way to avoid the trivial solution is to have infinite solutions (i.e. making the coefficient matrix singular):

$$\begin{cases} C_2 = -C_1 \dfrac{\cos(k_N L) + \cosh(k_N L)}{sin(k_N L) + sinh(k_N L)} \\ C_3 = -C_1 \\ C_4 = C_1 \dfrac{\cos(k_N L) + \cosh(k_N L)}{sin(k_N L) + sinh(k_N L)} \end{cases}$$

along with the singularity condition that will be used to obtain natural frequencies ω_N of the system.

$$\cos(k_N L) + \cosh(k_N L) = -1 \tag{2.4.2}$$

Solutions to the previous equation give us both the natural frequencies of the system (Table 2.4.1) along with their corresponding natural modes (Figure 2.4.1).

mode	$k_N L$	$\omega_N L^2/\sqrt{\gamma}$
1	1.8751	3.5160
2	4.6941	22.0345
3	7.8548	61.6973
4	10.9955	120.9019
5	14.1372	199.8596
6	17.2788	298.5555

Table 2.4.1: First natural frequencies of the clamped beam.

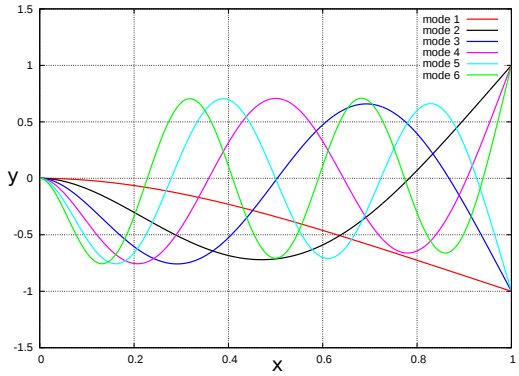

Figure 2.4.1: First natural modes of oscillations for the clamped beam normalized by the maximum amplitude.

Regarding the solution $A(s)$, i.e. the natural modes of the system, it will be defined up to a constant as expected:

$$\begin{aligned} A(s) &= C_1 \Big\{ [\cos(k_N s) - \cosh(k_N s)] \\ &+ \frac{\cos(k_N L) + \cosh(k_N L)}{\sin(k_N L) + \sinh(k_N L)} [\sinh(k_N s) - \sin(k_N x)] \Big\} \end{aligned} \tag{2.4.3}$$

2.4.2 Hinged beam

The hinged beam is similar to the clamped beam, but with the anchored end able to rotate. In this case the boundary conditions are the following:

- no displacement at the fixed end, i.e. $A(0) = 0$;

- zero torque at the fixed end, i.e. $A^{II}(0) = 0$, see eq. (2.3.3);
- zero torque at the free end, i.e. $A^{II}(L) = 0$, see eq. (2.3.3);
- zero shear at the free end, i.e. $A^{III}(L) = 0$, see eqs. (2.3.3) and (2.3.2);

From which we get

$$\begin{cases} C_1 = 0 \\ C_2 = C_4 \dfrac{\sinh(k_N L)}{\sin(k_N L)} \\ C_3 = 0 \end{cases}$$

along with the singularity condition that will be used to obtain natural frequencies ω_N of the system.

$$tan(k_N L) = tanh(k_N L)$$

As for the clamped beam, from the solution to this equation we will obtain both the natural frequencies of the system (Table 2.4.2) along with their corresponding natural modes (Figure 2.4.2). Please note that the first mode corresponds to the trivial solution $A(x) = 0$, corresponding to the first solution of the singularity condition. From a physical point of view, this corresponds to the system having one degree of instability (a rigid rotation around the anchored end).

$$A(s) = C_4 \left[\frac{\sinh(k_N L)}{\sin(k_N L)} \sin(k_N s) + \sinh(k_N s) \right] \tag{2.4.4}$$

mode	$k_N L$	$\omega_N L^2/\sqrt{\gamma}$
1	0	0
2	3.9266	15.4182
3	7.0686	49.9648
4	10.2102	104.2478
5	13.3518	178.2698
6	16.4934	272.0309

Table 2.4.2: First natural frequencies of the hinged beam normalized by the maximum amplitude.

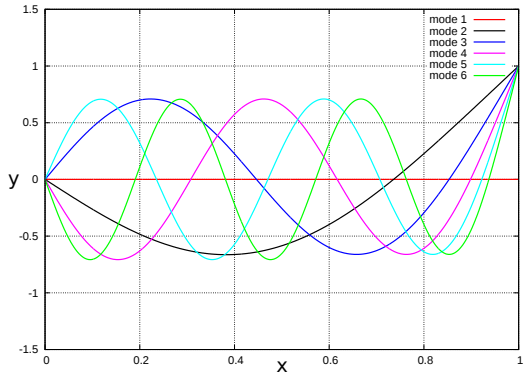

Figure 2.4.2: First natural modes of oscillations for the hinged beam.

2.5 Numerical methods for FSI

Traditionally two different ways have been introduced to achieve the two-way coupling needed for FSI: monolithic and partitioned.

In the monolithic approach a single system for the entire problem has to be formulated on the same variables and solved, thus the non-linear governing equations of both fluid and solid have to be linearized and discretized on the same mesh. Provided that the non-linearities of the subsystems can be resolved, the monolithic approach enables mathematical analysis of the coupled systems and leads to improved solution stability. Drawbacks of this approach are an higher degree of complexity of the solver even for very simple configurations and the possibility of getting an ill-conditioned system matrix due to mesh and rigidity differences between fluid and solid.

On the other hand the partitioned approach (which is by far the most used) considers separate domains for the fluid and solid (time-varying and whose union constitute the entire domain), with the possibility to discretize and solve them on different meshes using different methods (for instance finite volumes for fluid and finite elements for the solid) and solvers (linear or non-linear). The main drawback of this approach is the time lag between the solutions for fluid and for solid. As the solution of the fluid-solver system has to be consistent in terms of continuity of displacements and tensions, partitioned solvers differentiate into "weak" and "strong" coupled, where the "strength" of the coupling refers to the degree of convergence of the variables across the fluid-solid interface. In a weak

coupling there is no iteration between solvers, so that once the fluid domain is solved stresses are transferred to the solid and displacements are found. In a strong coupling algorithm, once displacements are computed the flow solver is run again on a deformed mesh and with different boundary conditions (i.e. solid velocity at the interface) with the result of finding slightly different stresses on the solid. In this way the loop continues until some convergence criteria is met. Unfortunately even the strictest convergence will lead to a time lag between the two solutions, so it is clear how loosely coupled schemes suffer from instability, while tightly coupled schemes contain computationally expansive sub-iterations.

In the present work a partitioned FSI solver has been developed in Matlab© for research purposes. This solver exploits a particular technique called immersed boundary (IB), first introduced by Peskin in 1972 [50]. The method is based on a mathematical formulation which employs a coupled Lagrangian-Eulerian formulation where information is effectively passed through a discretized version of the Dirac delta function. Since then several versions of the IB has been proposed by different authors, each with particular advantages and drawbacks. Since all of them are joined by the description of the solid geometry with a set of Lagrangian points moving in the background of an Eulerian mesh, they avoid any need for body-fitting meshes nor re-meshing (one of the most time-consuming steps of a standard FSI solver).

3

Modeling the fluid flow

The motion of a viscous incompressible flow is described by the Navier-Stokes equations, a set of partial differential equations obtained from the application of conservation of mass and momentum of a fluid flow in a given control volume,

$$\begin{cases} \dfrac{\partial \mathbf{u}}{\partial t} + \mathbf{u} \cdot \nabla \mathbf{u} = -\nabla p + \dfrac{1}{Re} \nabla^2 \mathbf{u} \\ \nabla \cdot \mathbf{u} = 0 \end{cases} , \tag{3.0.1}$$

where $\mathbf{u}$ is the velocity, p is the fluid pressure, t represents time and Re is the Reynolds number, defined as

$$Re = \frac{UL}{\nu}$$

where U and L are respectively velocity and length scales characteristic of the problem and ν is the fluid kinematic viscosity. The complete derivation of (3.0.1) can be found in every undergraduate textbook. As [40] comments, *"the Navier-Stokes equation is the cornerstone of fluid mechanics. It may look harmless enough, but it is an unsteady, nonlinear, second-order partial differential equation. If we were able to solve this equation for flows of any geometry, this book would be about half as thick."*

To date, analytical solutions of (3.0.1) are unobtainable except for very simple flow fields. Moreover, mathematicians have not yet proved that smooth solutions always exist, or that if they do exist, they have bounded energy per unit mass. This is called the *Navier-Stokes existence and smoothness problem.*

Since understanding the Navier-Stokes equations is considered to be the first step to understanding the elusive phenomenon of turbulence, the Clay Mathematics Institute made this problem one of its seven Millennium Prize problems in mathematics.

As an exact solution of (3.0.1) is not currently available, to obtain an approximate (but still useful) solution we dicretize it in a system of algebraic equations, which can then be solved on a computer. This technique is known as Computational Fluid Dynamics (CFD). In particular, the numerical simulation carried on in the present work can be defined as direct numerical simulation (DNS) since (3.0.1) are solved without recurring to the the Reynolds average technique and to any turbulence model.

Several discretization methods have been derived both before and after the birth of CFD, each of them designed with a specific application in mind. In the field of incompressible flow simulations one of the techniques for obtaining the pressure-velocity coupling of the Navier-Stokes equations is the projection method based on a multi-step time integration. In particular the Fractional Step Method has emerged for both its elegance and numerical efficiency.

3.1 The Fractional Step Method

The *Fractional Step Method* is an effective finite-difference method for solving (3.0.1). It was originally introduced by Alexandre Chorin in 1967 [46] and independently by Roger Temam [51], and afterwards improved by Perot [49] as a block LU decomposition.

This algorithm is based on the Helmholtz decomposition of any vector field $\mathbf{u}$ into a solenoidal part $\mathbf{u}_{sol}$ and an irrotational part $\mathbf{u}_{irr}$ and is based on two steps.

The Fractional Step Method has proved to be first order accurate both in time and space with general boundary conditions. A notable exception is when periodic boundary conditions are in effect, where it reaches second order accuracy both in time and space. In this thesis we shall refer to the matrix interpretation made by Perot in [49].

Let us consider the dimensionless unsteady incompressible Navier-Stokes equations (see for example [47], §1.6). Using an explicit Adams-Bashforth scheme for the non-linear convective terms and an implicit Crank-Nicholson (trapezoidal) scheme for the diffusive terms (Euler forward will be used for the first time step, see Section 5.3), (6.1.1) can be discretized in time as

$$\begin{cases} \dfrac{(\mathbf{u}^{n+1}-\mathbf{u}^{n})}{\Delta t} + \left[\dfrac{3}{2}N(\mathbf{u}^{n}) - \dfrac{1}{2}N(\mathbf{u}^{n-1})\right] = \\ = -G(p^{n+1}) + \dfrac{L(\mathbf{u}^{n+1})+L(\mathbf{u}^{n})}{2Re} + \mathrm{bc}_{mom} \\ \\ D(\mathbf{u}^{n}) = \mathrm{bc}_{cont} \end{cases} \tag{3.1.1}$$

where N, G, L and D are respectively the non-linear convective, gradient, Laplacian and divergence spatial operators. Moreover, bc_{cont} and bc_{cont} are the boundary conditions arising in the respective equations from discretization of spatial

operators near solid walls. Manipulation of (3.1.1) leads to

$$\begin{cases} \dfrac{\mathbf{u}^{n+1}}{\Delta t} - \dfrac{L(\mathbf{u}^{n+1})}{2Re} + G(p^{n+1}) = \\ = \dfrac{\mathbf{u}^{n}}{\Delta t} - \left[\dfrac{3}{2}N(\mathbf{u}^{n}) - \dfrac{1}{2}N(\mathbf{u}^{n-1})\right] + \dfrac{L(\mathbf{u}^{n})}{2Re} + \mathrm{bc}_{mom} \\ \\ D(\mathbf{u}^{n+1}) = \mathrm{bc}_{cont} \end{cases} \tag{3.1.2}$$

and having defined

$$A = \frac{1}{\Delta t} - \frac{L}{2Re} \quad ; \quad \mathbf{r}^{n} = \frac{\mathbf{u}^{n}}{\Delta t} - \left[\frac{3}{2}N(\mathbf{u}^{n}) - \frac{1}{2}N(\mathbf{u}^{n-1})\right] + \frac{L(\mathbf{u}^{n})}{2Re}$$

$$\begin{cases} A(\mathbf{u}^{n+1}) + G(p^{n+1}) = \mathbf{r}^{n} + \mathrm{bc}_{mom} \\ D(\mathbf{u}^{n}) = \mathrm{bc}_{mom} \end{cases} \tag{3.1.3}$$

The above-written system can be discretized in space by specifying the spatial operators A, G and D.

$$\begin{bmatrix} A & G \\ D & 0 \end{bmatrix} \begin{bmatrix} \mathbf{u}^{n+1} \\ p^{n+1} \end{bmatrix} = \begin{bmatrix} \mathbf{r}^{n} \\ 0 \end{bmatrix} + \begin{bmatrix} \mathrm{bc}_{mom} \\ \mathrm{bc}_{cont} \end{bmatrix} \tag{3.1.4}$$

As said in [54], *systems of the form similar to 3.1.4 are known as Karush-Kuhn-Tucker (KKT) systems that appears in constrained optimization problems in that they minimized a term similar to the kinetic energy*

$$\min_{\mathbf{u}^{n+1}} \left[\frac{1}{2}(\mathbf{u}^{n+1})^{T} A \mathbf{u}^{n+1} - (\mathbf{u}^{n+1})^{T}(\mathbf{r}^{n} + bc_{mom})\right]$$

$$s.t. \quad D\mathbf{u}^{n+1} = 0 + bc_{cont}$$

It is interesting that the discrete pressure p does not play a direct role in time advancement, but acts as a set of Lagrange multipliers to minimize the system energy and satisfy the kinematic constraint of divergence-free velocity field.

We recall here that energy conservation requires the divergence and gradient operators to be *skew-adjoint*, i.e. $G^{T} = -D$. This condition plays an important role in the choice of the spatial discretization as pointed out in Section 5.1. Equation (3.1.4) can be factored into a block LU decomposition

$$\begin{bmatrix} A & 0 \\ D & -\Delta t\ D\ G \end{bmatrix} \begin{bmatrix} I & \Delta t\ G \\ 0 & I \end{bmatrix} \begin{bmatrix} \mathbf{u}^{n+1} \\ p^{n+1} \end{bmatrix} = \begin{bmatrix} \mathbf{r}^{n} \\ 0 \end{bmatrix} + \begin{bmatrix} \mathrm{bc}_{mom} \\ \mathrm{bc}_{cont} \end{bmatrix}$$

with an error of $(\Delta t/2Re)LGp^{n+1}$ in the upper leftward term, thus making the method only first order accurate in time. However, as pointed out in [49], it

is possible to use this information to create a second-order method. Moreover, when periodic boundary conditions are in effect, the fractional method will recover second-order accuracy in time (for a more detailed discussion see [49], end of chapter 6).We can then split the large indefinite system (3.1.5a) into two smaller, far better behaved problems

$$\begin{bmatrix} A & 0 \\ D & -\Delta t\ D\ G \end{bmatrix} \begin{bmatrix} \mathbf{u}^* \\ p^{n+1} \end{bmatrix} = \begin{bmatrix} \mathbf{r}^n \\ 0 \end{bmatrix} + \begin{bmatrix} \mathrm{bc}_{mom} \\ \mathrm{bc}_{cont} \end{bmatrix} \tag{3.1.5a}$$

$$\begin{bmatrix} I & \Delta t\ G \\ 0 & I \end{bmatrix} \begin{bmatrix} \mathbf{u}^{n+1} \\ p^{n+1} \end{bmatrix} = \begin{bmatrix} \mathbf{u}^* \\ p^{n+1} \end{bmatrix} \tag{3.1.5b}$$

that can be also written as

$$\begin{aligned} A\ \mathbf{u}^* &= \mathbf{r}^n + \mathrm{bc}_{mom} \\ \Delta t\ D\ G\ p^{n+1} &= D\ \mathbf{u}^* - \mathrm{bc}_{cont} \\ \mathbf{u}^{n+1} &= \mathbf{u}^* - \Delta t\ G\ p^{n+1} \end{aligned} \tag{3.1.6}$$

Equations (3.1.6) bear a close resemblance to the traditional Fractional Step Method usually presented as a semi-discrete method for time splitting and represent the steps actually performed in the numerical code. In particular, the first equation gives the intermediate velocity $\mathbf{u}^*$ that does not satisfy the incompressibility constraint. In the second a Poisson equation has to be solved in order to get the new pressure field p^{n+1}, whereas in the third the pressure p^{n+1} is used to project the intermediate velocity $\mathbf{u}^*$ onto a space of divergence-free velocity fields to obtain the updated velocity field $\mathbf{u}^{n+1}$.

In the following paragraphs the discretization of both spatial operators and boundary conditions will be discussed. As the staggered arrangement allows all spatial operators to be evaluated through centered differences, the spatial accuracy of the method will be second order.

4

The Immersed Boundary approach

The *immersed boundary (IB)* method is a mathematical approach used for problems in which a slender structure interacts with a viscous incompressible flow. It turns out to be very effective in handling moving or deforming bodies with complex surface geometry. Peskin [50] first introduced the method in 1972 to simulate blood flow inside a heart with flexible valves. Since then it has been used in a wide variety of applications, especially in bio-fluid dynamics problems where complex geometries and immersed elastic membranes or structures are present and make traditional computational approaches difficult.

The key point of the IB approach consists of describing the flow field on a Eulerian grid, while representing the immersed surface with a set of Lagrangian points. The Eulerian grid is not required to conform to the body surface (so that it can be structured Cartesian) as the information between the two grids is passed through a discretization of the Dirac Delta function. The no-slip condition is enforced at the Lagrangian points by introducing appropriate surface forces in the Navier-Stokes equations.

Let $\mathbf{x} = (x, y) \in \Omega$ be the Cartesian physical coordinates, with Ω denoting the physical domain; let $s \in \Gamma$ be the Lagrangian curvilinear coordinate, with Γ denoting the body surface; let $\mathbf{X}(s,t) = (x(s,t), y(s,t)) \in \Gamma$ denote the physical position of each material point of curvilinear coordinate s at time t (Figure 4.0.1). The main equations of the IB method can thus be summarized as

$$\begin{cases} \dfrac{\partial \mathbf{u}}{\partial t}(\mathbf{x},t) + \mathbf{u}(\mathbf{x},t)\cdot\nabla\mathbf{u}(\mathbf{x},t) = \\ \qquad\qquad - \nabla p(\mathbf{x},t) + \dfrac{1}{Re}\nabla^2\mathbf{u}(\mathbf{x},t) + \mathbf{f}(\mathbf{x},t) \\ \nabla\cdot\mathbf{u}(\mathbf{x},t) = 0 \end{cases} \tag{4.0.1}$$

$$\mathbf{f}(\mathbf{x},t) = \int_\Gamma \mathbf{F}(s,t)\delta_h(\mathbf{x} - \mathbf{X}(s,t))ds, \tag{4.0.2}$$

$$\mathbf{U}_{ib} = \frac{\partial \mathbf{X}}{\partial t} = \int_\Omega \mathbf{u}(\mathbf{x},t)\delta_h(\mathbf{x} - \mathbf{X}(s,t))d\Omega, \tag{4.0.3}$$

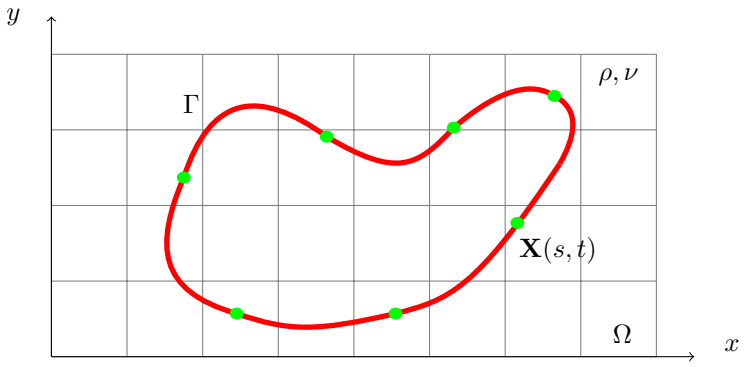

Figure 4.0.1: IB Γ (in red) described by a set of Lagrangian points $\mathbf{X}(s,t)$ (in green) in fluid region Ω with background Cartesian mesh.

where the Navier-Stokes equations describing fluid motion (4.0.1) are considered together with an artificial forcing $\mathbf{f}$ to enforce the no-slip condition and solved on the background cartesian structured mesh preserving numerical efficiency. The momentum forcing $\mathbf{f}$ derives from the convolution between the solid stress term $\mathbf{F}$ and the discretized version of Dirac Delta function δ_h (4.0.2). Analogously, the velocity of immersed boundary comes from the convolution of δ_h with the surrounding flow field (4.0.3). The convolution with the discretized Dirac Delta function δ_h is a weighted interpolation and represents an effective way to link the Lagrangian variables $\mathbf{F}$ and $\mathbf{U}_{ib}$ with their Eulerian counterparts $\mathbf{f}$ and $\mathbf{u}$. For simplicity's sake, in the following the subscript h will be dropped.

Among a wide choice of synthetic Delta functions, we made use of the one proposed by Roma in [69]:

$$\delta_h(r) = \begin{cases} \dfrac{1}{6\Delta r}\left[5 - 3\dfrac{|r|}{\Delta r} - \sqrt{1 - 3\left(1 - \dfrac{|r|}{\Delta r}\right)^2}\right] & \\ \qquad\qquad\qquad\qquad \text{if } 0.5\Delta r \le |r| \le 1.5\Delta r & \\ \dfrac{1}{3\Delta r}\left[1 + \sqrt{1 - 3\left(\dfrac{|r|}{\Delta r}\right)^2}\right] \quad \text{if } |r| \le 0.5\Delta r & \\ 0 \qquad\qquad\qquad\qquad \text{otherwise.} & \end{cases} \tag{4.0.4}$$

Starting from this basic idea, several implementations of the IB have been documented in literature. In the following we will describe in depth the three of them we used for the applications described in Chapter 6: the projection approach (Section 4.1), the original IB by Peskin and coworkers (Section 4.2) and IB by Huang, Shin and Sung (Section 4.3).

4.1 The IB projection approach

This approach was introduced by Taira & Colonius and described properly in [54], where they illustrated how their work can be seen as a valuable extension of the Fractional Step method by Chorin [46] and Temam [51] described in 3.1.

As stated in [54], *since the discretized Navier-Stokes equations (3.1.4) are observed to be a KKT system with pressure acting as a set of Lagrange multipliers to satisfy constraint, one can image appending additional algebraic constraints by increasing the number of Lagrange multipliers*, i.e. incorporate the no-slip constraint through the solid stress term $\mathbf{F}$.

In this case the IB formulation is written as

$$\frac{\partial \mathbf{u}}{\partial t}(\mathbf{x},t) + \mathbf{u}(\mathbf{x},t)\cdot\nabla\mathbf{u}(\mathbf{x},t) = -\nabla p(\mathbf{x},t) + \frac{1}{Re}\nabla^2\mathbf{u}(\mathbf{x},t) + \\ + \int_\Gamma \mathbf{F}(s,t)\delta(\mathbf{x}-\mathbf{X}(s,t))ds, \tag{4.1.1}$$

$$\nabla\cdot\mathbf{u}(\mathbf{x},t) = 0, \tag{4.1.2}$$

$$\mathbf{U}_{ib}(s,t) = \int_\Omega \mathbf{u}(\mathbf{x},t)\delta(\mathbf{x}-\mathbf{X}(s,t))d\Omega, \tag{4.1.3}$$

where $\mathbf{U}_{ib}(s,t)$ is the imposed boundary velocity, that can be either given or calculated (as for a free falling body).

As in (3.1.4), this system of equations can be summarized in a matrix form

$$\begin{bmatrix} A & G & -H \\ D & 0 & 0 \\ E & 0 & 0 \end{bmatrix} \begin{bmatrix} \mathbf{q}^{n+1} \\ p \\ \mathbf{F} \end{bmatrix} = \begin{bmatrix} \mathbf{r}^n + \mathrm{bc}_{mom} \\ \mathrm{bc}_{cont} \\ \mathbf{U}_{ib}^{n+1} \end{bmatrix} \tag{4.1.4}$$

where $H\ \mathbf{F}$ corresponds to the last term in equation (4.1.1) and $E\ \mathbf{q}^{n+1}$ is related through a scaling to the left-hand-side of the no-slip condition (4.1.3).

The advantage of this method is that one can show (see Appendix of [54]) that through ad-hoc scaling the system matrix can be made skew-adjoint as for the original Fractional Step Method in that $D = -G^T$ and $-H = E^T$. This enables us to introduce the variable $Q = [G, E^T]$ so that the system can be simplified into the KKT form:

$$\begin{bmatrix} A & G \\ Q & 0 \end{bmatrix} \begin{bmatrix} \mathbf{q}^{n+1} \\ \lambda \end{bmatrix} = \begin{bmatrix} \mathbf{r}_1 \\ \mathbf{r}_2 \end{bmatrix} \tag{4.1.5}$$

where

$$\lambda = \begin{bmatrix} \mathbf{q}^{n+1} \\ p \end{bmatrix} \quad \mathbf{r}_1 = \mathbf{r}^n + \mathrm{bc}_{mom} \quad \mathbf{r}_2 = \begin{bmatrix} \mathbf{q}^{n+1} \\ p \end{bmatrix}$$

This method can be regarded as a monolithic approach to the FSI problem as it summarizes in one linear system both fluid, structure and their interaction. The main benefit of this method is numerical stability, which enables the use of large time-steps (up to CFL[1]= 0.5). Unfortunately, this elegant formulation cannot be used for deformable bodies in that the equations do not take into account structure deformations.

4.2 The IB approach by Peskin & coworkers

4.2.1 Neutrally buoyant membrane

The original IB formulation initially presented by Peskin to study heart valves leaflets was designed to take into account a neutrally buoyant boundary (i.e. same density for fluid and membrane). For an elastic boundary its discretization was made through the introduction of a discrete number of forces acting on straight-line segments connecting specified pairs of boundary points.

Since the boundary is neutrally buoyant an equation for the force between fluid and solid $\mathbf{F}$ the equilibrium condition on an infinitesimal part of the membrane gives

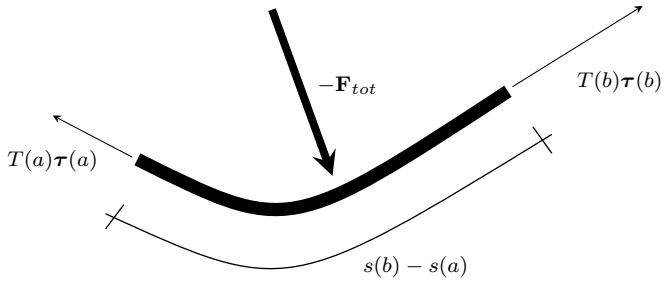

Figure 4.2.1: Equilibrium condition on a small element of membrane.

$$\sum_i F_i = 0 \Rightarrow -\mathbf{F}_{tot} + T(a)\boldsymbol{\tau}(a) + T(b)\boldsymbol{\tau}(b) = 0 \Rightarrow \int_a^b \mathbf{F}(s,t)\ d\hat{s} = [T\boldsymbol{\tau}]_a^b \tag{4.2.1}$$

[1]The Courant-Friedrichs-Lewy number, defined as $U\Delta x/\Delta t$ (where U is a representative velocity, Δx is the mesh-grid size and $\Delta t$is the time step), is a quantity of uttermost importance in CFD as it is related to the numerical stability of a temporal integration scheme

where $\boldsymbol{\tau}(s,t) = (\partial\mathbf{X}/\partial s)/\left\|\partial\mathbf{X}/\partial s\right\|$ is the unitary tangent vector to the boundary at the points b and a, respectively and $T(s,t)$ is the tension. Using the Fundamental Theorem of Calculus equation (4.2.1) can be rewritten as

$$\int_a^b \left(\mathbf{F}(s,t) - \frac{\partial T\boldsymbol{\tau}}{\partial s}\right) d\hat{s} = 0,$$

or

$$\mathbf{F}(s,t) = \frac{\partial}{\partial s}\left(T(s,t)\boldsymbol{\tau}(s,t)\right). \tag{4.2.2}$$

Assuming the reference configuration to be unstressed and that the mechanical behavior of the material is well described by a Hookean material, the tension would be

$$T(s,t) = \kappa\left(\left\|\frac{\partial\mathbf{X}}{\partial s}\right\| - 1\right) \tag{4.2.3}$$

where κ is a large numerical parameter needed to enforce the inextensibility of the boundary up to a desired value (according to literature no more than 0.1%).

The main advantage of this method is that the no-slip condition on the boundary is enforced by definition (Lagrangian points move with the local fluid velocity). As we can see by inspecting the governing equations, this method suffers from the lack of equations describing structure dynamics. In turn, this causes problems both in the enforcement of the inextensibility condition and on the resolution of solid forces. Moreover, given that Lagrangian points are connected by stiff springs, the time step for the numerical integration has to be small enough not only to satisfy the stability of the fluid solver, but also to effectively solve the spring oscillations, whose characteristic period is proportional to $\kappa^{-1/2}$, κ being the spring stiffness.

4.2.2 Massive membrane

With the massless assumption, however, we cannot approach many other problems for which the boundary mass is important (it is usually the case for elastic boundaries immersed in air). Thus, different strategies have been developed in order to overcome this issue.

Zhu & Peskin proposed a method based on a non-uniform distribution of density spread by the usual discretized Delta function, that in the dimensional form read as

$$\rho(\mathbf{x},t) = \rho_f + \int_\Gamma \rho_1\delta_h(\mathbf{x} - \mathbf{X}(s,t))ds$$

Please note that mass density ρ_1 is the structure density *in addition* to fluid density ρ_f, i.e. $\rho_1 = \rho_f - \rho_s A$ where ρ_s is the density of the structure and A is

the membrane cross-section. It is indeed in the spirit of the IB formulation to add something (the immersed boundary) to an already filled-with-fluid domain.

Unfortunately, because of the non-uniform density fast solvers such as FFT-based methods cannot be employed here.

In order to retain the use of the FFT solver, Kim & Peskin proposed an alternative way to give mass to the elastic boundary called the *penalty* immersed boundary method. To derive this method the starting equations are the same as for the method by Zhu & Peskin:

$$\rho\left(\frac{\partial \mathbf{u}}{\partial t} + \mathbf{u}\cdot\nabla\mathbf{u}\right) = -\nabla p + \mu\nabla^2\mathbf{u} + \mathbf{f}$$

$$\rho(\mathbf{x},t) = \rho_f + \int_\Gamma \rho_1 \delta_h(\mathbf{x} - \mathbf{X}(s,t))ds$$

We substitute the density definition in the momentum equation and separate the left-hand side into two terms: one involving the constant density ρ_0 and the other containing the singular part that comes from the immersed boundary. In dimensionless form we then write

$$\frac{\partial \mathbf{u}}{\partial t} + \mathbf{u}\cdot\nabla\mathbf{u} = -\nabla p + \frac{1}{Re}\nabla^2\mathbf{u} + \mathbf{f} - \int_\Gamma \frac{\rho_1}{\rho_0 L}\frac{D\mathbf{u}}{Dt}\delta_h(\mathbf{x} - \mathbf{X}(s,t))ds$$

where L is a characteristic length scale of the problem and D/Dt is the material derivative. Using another form of the no-slip condition

$$\frac{\partial^2 \mathbf{X}}{\partial t^2} = \frac{D\mathbf{u}}{Dt}$$

we can then write

$$\frac{\partial \mathbf{u}}{\partial t} + \mathbf{u}\cdot\nabla\mathbf{u} = -\nabla p + \frac{1}{Re}\nabla^2\mathbf{u} + \mathbf{f} - \mathbf{f}_D$$

$$\mathbf{f}_D = \int_\Gamma \frac{\rho_1}{\rho_0 L}\frac{\partial^2 \mathbf{X}}{\partial t^2}\delta_h(\mathbf{x} - \mathbf{X}(s,t))ds$$

where $\mathbf{f}_D$ can be interpreted as an Eulerian body force obtained by using the Dirac delta function to transform the Lagrangian expression

$$\mathbf{F}_D = \frac{\rho_1}{\rho_0 L}\frac{\partial^2 \mathbf{X}}{\partial t^2}$$

which is known as the D'Alembert force.

The key idea of this method is to split the immersed boundary conceptually into two Lagrangian components, one massless and interacting with the fluid and the other carrying mass and bounded by massless springs to the first boundary. An accurate presentation of this method is found in [55].

Advantages and drawbacks of these methods derive from the original implementation of the method by Peskin, plus an additional arbitrary parameter given by the stiffness of springs connecting the two boundaries.

4.3 The IB approach by Huang, Shin & Sung

The approach proposed by Huang, Shin & Sung [52] presents a substantial difference from the previous ones in that the dynamics of the structure is explicitly taken into consideration (thus considering directly its mass). Moreover, the inextensibility condition

$$\frac{\partial \mathbf{X}}{\partial s} \cdot \frac{\partial \mathbf{X}}{\partial s} = 1 \tag{4.3.1}$$

is fully satisfied by using the tension as a Lagrangian multiplier (in the same spirit of pressure for incompressibility). In this method the forces acting on the filament are calculated by means of Goldstein's feedback law [59]:

$$\mathbf{F} = \alpha \int_0^t (\mathbf{U}_{ib} - \frac{\partial \mathbf{X}}{\partial t}) dt' + \beta (\mathbf{U}_{ib} - \frac{\partial \mathbf{X}}{\partial t}) \tag{4.3.2}$$

where α and β are large negative constants, $\mathbf{U}_{ib}$ is the fluid velocity interpolated at the immersed boundary. This methodology, whose advantages and drawbacks will be discussed in Section 4.4.2, has also been exploited in [57, 58].

This method was developed specifically for the dynamics of a hinged or clamped filament, so it considers a massive inextensible filament described by

$$\rho_1 \frac{\partial^2 \mathbf{X}^*}{\partial t^{*2}} = \frac{\partial}{\partial s^*} \left(T^* \frac{\partial \mathbf{X}^*}{\partial s^*} \right) - \frac{\partial^2}{\partial s^{*2}} \left(\gamma^* \frac{\partial^2 \mathbf{X}^*}{\partial s^{*2}} \right) + \rho_1 \mathbf{g} - \mathbf{F}^* \tag{4.3.3}$$

surrounded by a viscous incompressible fluid described as

$$\rho_0 \left(\frac{\partial \mathbf{u}^*}{\partial t^*} + \mathbf{u}^* \cdot \nabla \mathbf{u}^* \right) = -\nabla p^* + \mu \nabla^2 \mathbf{u}^* + \mathbf{f}^* \tag{4.3.4}$$

where T^* is the tension along the filament axis, γ^* is the bending rigidity and $\mathbf{F}$ is the Lagrangian forcing exerted by the filament on the surrounding fluid (the description given in [52] at the beginning of page 2209 is incorrect on this point). As in Section 4.2, ρ_1 denotes the density difference between the filament and

the surrounding fluid, so $\rho_1 = 0$ represents the neutrally buoyant case. In the case of neutrally buoyant boundaries equation 4.3.3 loses the temporal term, so the time integration of the filament position $\mathbf{X}$ becomes harder. In this case the original approach by Peskin and coworkers (see Section 4.2) becomes preferable.

Equations (4.3.3) and (4.3.4) can be made dimensionless by introducing the following characteristic scales: the reference filament length L for length, the far-field velocity U_∞ for velocity, L/U_∞ for time, $\rho_0 U_\infty^2$ for pressure p^*, $\rho_0 U_\infty^2/L$ for the Eulerian momentum forcing $\mathbf{f}^*$, $\rho_1 U_\infty^2/L$ for the Lagrangian momentum forcing $\mathbf{F}^*$, $\rho_1 U_\infty^2$ for the tension T^* and $\rho_1 U_\infty^2 L^2$ for the bending rigidity γ^* (their dimensionless counterparts will drop the star):

$$\frac{\partial^2 \mathbf{X}}{\partial t^2} = \frac{\partial}{\partial s}\left(T\frac{\partial \mathbf{X}}{\partial s}\right) - \frac{\partial^2}{\partial s^2}\left(\gamma\frac{\partial^2 \mathbf{X}}{\partial s^2}\right) + Fr\frac{\mathbf{g}}{g} - \mathbf{F} \tag{4.3.5}$$

$$\frac{\partial \mathbf{u}}{\partial t} + \mathbf{u}\cdot\nabla\mathbf{u} = -\nabla p + \frac{1}{Re}\nabla^2\mathbf{u} + \mathbf{f} \tag{4.3.6}$$

where Fr is the Froude number defined as gL/U^2. Note that two different densities, ρ_0 and ρ_1, have been used for structure and fluid equations: this difference will be considered in the spreading from the Lagrangian to the Eulerian grid:

$$\mathbf{f}(\mathbf{x},t) = \rho\int_\Gamma \mathbf{F}(s,t)\delta(\mathbf{x}-\mathbf{X}(s,t))ds \tag{4.3.7}$$

where $\rho = \rho_1/(\rho_0 L)$ comes from the different non-dimensionalization scales chosen for Equations 4.3.4 and 4.3.3. In this method the tension force T is determined by a Poisson equation derived by inserting the constraint of inextensibility into the beam dynamical equation:

$$\frac{\partial \mathbf{X}}{\partial s}\frac{\partial^2}{\partial s^2}\left(T\frac{\partial \mathbf{X}}{\partial s}\right) = \frac{1}{2}\frac{\partial^2}{\partial t^2}\left(\frac{\partial \mathbf{X}}{\partial s}\frac{\partial \mathbf{X}}{\partial s}\right) - \frac{\partial^2 \mathbf{X}}{\partial t \partial s}\frac{\partial^2 \mathbf{X}}{\partial t \partial s} - \frac{\partial \mathbf{X}}{\partial s}\frac{\partial}{\partial s}(\mathbf{F}_b - \mathbf{F}) \tag{4.3.8}$$

Where $\mathbf{F}_b = -\frac{\partial^2}{\partial s^2}(\gamma\partial\mathbf{X}^2/\partial s^2)$ denotes the bending force. Equations (4.3.5) and (4.3.8) for filament dynamics are solved respectively for $\mathbf{X}$ and T at Lagrangian ($\bullet$) and interface ($|$) points.

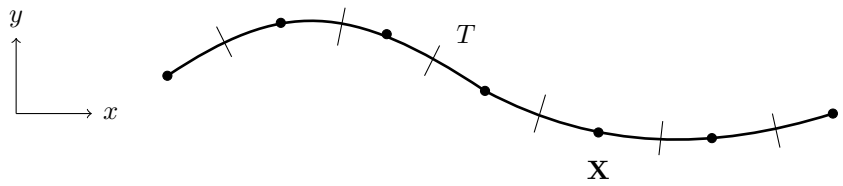

Figure 4.3.1: Filament Γ described by a set of Lagrangian points $\mathbf{X}(s,t)$.

4.4 Permeability

Besides elasticity and mass, biological tissues are characterized by permeability in that they consist of dispersed cells separated by connective voids which allow normal mass transport. Moreover, there are several technological applications of porous synthetic membranes, mostly in separation industry.

Permeability, i.e. the ability of a medium to allow a fluid flow through it, comes into play in a wide variety of fields (e.g. earth science, medicine, biology, chemistry) as a consequence of voids in a solid matrix and a driving fluid pressure gradient. Ground-water flows get enriched in minerals through fractures in rock formations and blood undergoes filtration through the glomerular basement membrane of the kidneys thanks to filtration slits between cells. Permeability plays a central role in membrane technology, widely used in the food technology, biotechnology and pharmaceutical industries to selectively separate different components based on their size or electric charge.

Despite previous examples, in which permeability has been exploited for different porpuses, this thesis is aimed at investigating how permeability affects the performances of elastic objects. As already pointed out by the work of Kim and Peskin [68], pressure redistribution from high to low pressure zones modifies the near-wake region behind bluff bodies, enhancing their stability.

In the following sections we will describe the only approach currently available in literature to include permeability in the framework of the IB method, along with the approach that has been developed during the current thesis.

4.4.1 The velocity approach

In this section we will cover the approach introduced by Kim and Peskin [68] in order to model the permeability of a parachute canopy. As this approach places itself in the IB method described in Section 4.2, the authors model permeability as a relative slip velocity in the direction normal to the boundary between the fluid and the boundary itself. In this way a normal flux through the boundary is naturally achieved, while a force reduction can be seen in an indirect way.

The need to include a no-slip velocity can be demonstrated by considering the force equilibrium on a massless token of canopy of length ds. Since there are no inertial terms, the equilibrium gives

$$(p_1 - p_2)\left|\frac{\partial \mathbf{X}}{\partial s}\right| ds + \mathbf{F}\cdot\mathbf{n} ds = 0 \tag{4.4.1}$$

Starting from the basic assumption of the validity of Darcy's law, i.e. of a linear

dependence between flux and pressure difference across the membrane through a coefficient called aerodynamic conductance γ, we get

$$\beta\gamma(p_1 - p_2)ds = \left(\mathbf{U} - \frac{\partial \mathbf{X}}{\partial t}\right) \cdot \mathbf{n} \left|\frac{\partial \mathbf{X}}{\partial s}\right| ds \tag{4.4.2}$$

where βds is the number of pores in the interval $(s, s + ds)$, while the factor $|\partial \mathbf{X}/\partial s|$ appears because, the authors say, $|\partial \mathbf{X}/\partial s|ds$ is the arc length of the segment $(s, s + ds)$. Combining equations (4.4.1) and (4.4.2) we finally get the expression for the normal component of the slip velocity on the boundary:

$$\left(\mathbf{U} - \frac{\partial \mathbf{X}}{\partial t}\right) \cdot \mathbf{n} = \frac{\beta\gamma}{|\partial \mathbf{X}/\partial s|^2} \mathbf{F} \cdot \mathbf{n} \tag{4.4.3}$$

while the authors assign a no-slip condition in the tangential direction by assuming pores oriented normal to the surface of the shell. Lacking other more elaborated model, by assuming $\beta\gamma$ proportional to $|\partial \mathbf{X}/\partial s|^2$ by a factor λ, we can rewrite

$$\frac{\partial \mathbf{X}}{\partial t} = \mathbf{U} + \lambda \left(\mathbf{F} \cdot \mathbf{n}\right) \mathbf{n} \tag{4.4.4}$$

This approach is neat and simple to implement. However except for some controlled cases equation (4.4.4) causes numerical problems when plugged into the IB formulation described in Section 4.2 since the Lagrangian quantity $\mathbf{F}$ is usually very noisy (Figure 4.4.1), thus making $\mathbf{X}$ noisier at every new time step. As in turn $\mathbf{F}$ depends on $\mathbf{X}$ through the constitutive equation of the boundary, equation (4.4.4) leads to numerical instability.

The noisy nature of $\mathbf{F}$ seems to derive from the discretization of the filament as a series of springs disconnected from one another, so that it is possible that the i^{th} spring is compressed while the $(i + 1)^{th}$ is extended. This leads to the peak-to-peak classical appareance of $\mathbf{F}$. Possible strategies to overcome this issue, such as the application of a low-pass filter, have been considered. In order not to lose or gain momentum, such filters have to preserve the integral value of $\mathbf{F}$. However, this strategy did not lead to positive results since the application of a filter added new free constants (e.g. the threshold frequency) that needed to be determined, and this approach has been discarded in favor of that described in the next section.

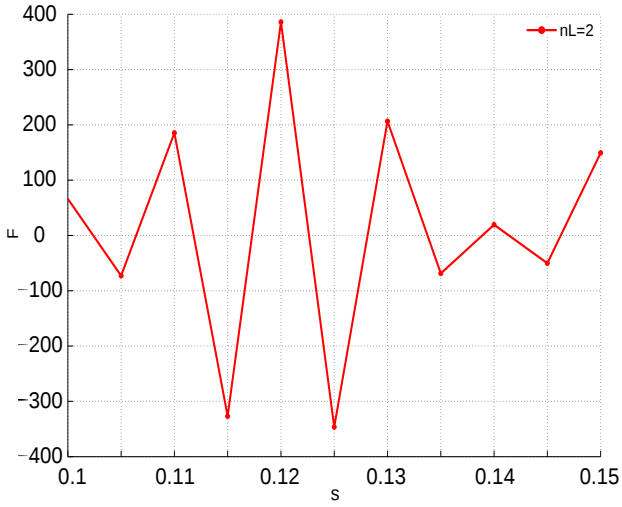

Figure 4.4.1: Lagrangian forces **F** along the curvilinear abscissa s of a simply hinged filament subject to an incoming flow. In this simulation 2 Lagrangian points per Eulerian grid were approximately used to describe the surface.

4.4.2 The force approach

Given the limitations of the velocity approach we tried to tackle the problem by using a dualistic approach based on the reduction of forces instead of velocities. In order to do so, our new approach needed to be inserted in an IB formulation different from that described in Section 4.2, and in particular we found an effective approach in the one described in 4.3.

We would like to point out the difference between the two approaches, both of which contains advantages and drawbacks. In the original approach by Peskin the no-slip condition is enforced by definition in that Lagrangian boundary points are passively transported by the surrounding fluids, and the filament is composed of stiff springs preventing Lagrangian points not getting too far away or too near. The approach of Huang, Shing and Sung, on the other hand, solves the beam dynamical equations satisfying the inextensibility constraint starting from the aerodynamical loads on the filament.

The first difference between the two approaches is that while the solid solver for Peskin [67] takes as input the point velocity $\partial\mathbf{X}/\partial t$ and returns the La-

grangian forces $\mathbf{F}$, the solid solver in the case of Huang, Shing and Sung [52] needs the Lagrangian forces as input and gives back the velocity of the filament points. The second difference is that while the approach by Peskin satisfies the no-slip condition to machine precision but fails to fulfill the inextensibility of the filament, the approach by Huang, Shing and Sung does exactly the opposite.

By placing itself in the Huang, Shing and Sung approach, we model permeability by decreasing the normal component of momentum transferred from the fluid to the filament:

$$\mathbf{F} = (1 - \lambda) \cdot (\mathbf{F}_{imp} \cdot \mathbf{n})\mathbf{n} + (\mathbf{F}_{imp} \cdot \boldsymbol{\tau})\boldsymbol{\tau} \tag{4.4.5}$$

where $\mathbf{F}_{imp}$ represents the force exerted by the fluid on an impermeable filament, $\mathbf{n}$ and $\boldsymbol{\tau}$ are the unit versor normal and tangent to the filament, while $\mathbf{F}$ is the reduced force because of permeability. Eq.(4.4.5) is physically motivated by the fact that while tangential stresses on a solid surface come from the tangential component of velocity normal derivative $(\partial\mathbf{u}/\partial\mathbf{n}) \cdot \boldsymbol{\tau}$, the normal part derives only from pressure differences across the surface, so permeability affects only this component by reducing the pressure drop.

We want to stress the duality of this approach with the one used by Peskin and coworkers since a relative slip velocity will decrease the momentum transferred to the filament, while the present approach based on the reduction of momentum will lead to a slip velocity.

5

Code description

This Chapter describes the implementation of a Finite Volume (FV) code for the Direct Numerical Simulation (DNS) of the interaction between a fluid flow and an elastic body.

The governing equations for the fluid motion (Navier-Stokes equations) are solved on a staggered grid using the fractional step method, while the interaction with the solid body is handled via an Immersed Boundary method.

Sections 5.1 represents the numerical discretization of the Fractional Step Method described in 3.1, while Saspaections 5.2 and 5.3 deal with the technical details on how spatial operators, boundary conditions and time integration are implemented in the code. An illustration of the storage system of both fields and operators is made in Section 5.4. Finally, validation cases are described in Section 5.5.

The numerical code is freely downloadable from [53].

5.1 Spatial discretization

5.1.1 Staggered grid

The set of discrete locations at which the variables are to be calculated define the so-called *numerical grid*, which is essentially a discrete representation of the geometric continuous domain in which the problem is to be solved.

The obvious choice is to evaluate all the variables (pressure and velocity) on the same set of grid points (such a grid is called *co-located*), but despite its computational advantages this arrangement leads to some significant drawbacks regarding the solution of the pressure field, given by a Poisson equation.

Since energy conservation requires $G^T = -D$, it is possible to show [47], §7.5.2 that a co-located grid approach would result in a discretization of the Poisson equation on a grid twice as coarse as the original one, and the equation would be split into four unconnected systems, one with i and j both even, one with i and j both odd, one with i even and j odd and one with i odd and j even (checkerboard pressure scheme). Each of these systems give a different solution, resulting in spurious "pressure oscillations" even with smooth velocity fields.

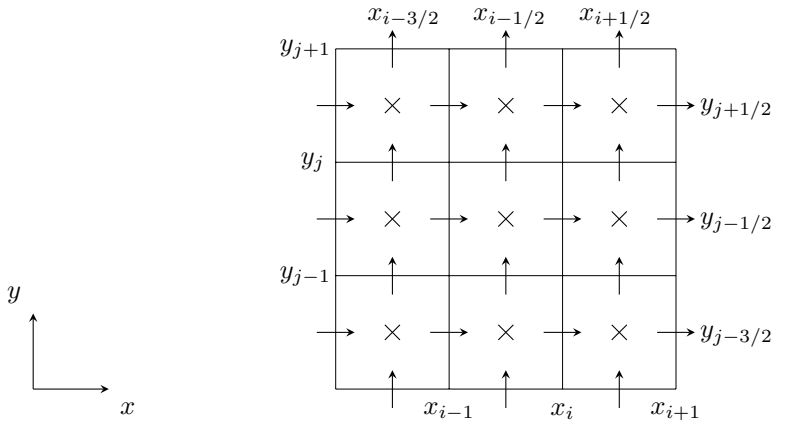

Figure 5.1.1: Staggered grid. x-velocity component u_x is evaluated at $\rightarrow$, y-velocity component u_y at $\uparrow$, whereas pressure at $\times$.

In Cartesian coordinates, the *staggered grid* introduced by Harlow and Welsh (1965) offers several advantages over the co-located grid, the biggest of which is the strong coupling between the velocities and the pressure, avoiding oscillations in pressure field. The numerical approximation on a staggered grid with central derivatives is also kinetic energy conservative, with the advantages that were discussed earlier. Moreover both the pressure and diffusion terms are very naturally approximated by central differences without interpolation, since the pressure nodes lie at cell centers and horizontal and vertical velocity components lie at the center of cell faces.

This grid choice has a few drawbacks on the data structure: depending on the particular boundary conditions, velocity and pressure fields do not have the same size and their computational domain may change. In the following description, and also in the code, we will label the face coordinates ($x_{n\pm1/2}$, $y_{n\pm1/2}$) as "geometry" and the face centers (x_n, y_n) as "center" (see Figure 5.1.1).

Stretched grid

Numerical simulations are memory-demanding and time-consuming, depending mainly on the dimension of the domain being resolved and on the resolution at which the solution is sought. Moreover, the time step is also a direct consequence of the grid resolution through the CFL number.

One possible way to speed-up the code without degrading the precision of

the solution in the region near the body comes from stretched grids. Since a good solution requires high resolution in the presence of high gradients we can design our numerical grid in order to have high resolution where needed, and making it coarse elsewhere.

The main drawback of this grid arrangement is the loss of accuracy of differential operators: it can be shown ([47], §3.3.4) that the central derivative scheme does not maintain a second-order accuracy when applied to a stretched grid but, naming *stretching factor* r the ratio between two neighbor grid spacings ($\Delta_{i+1} = r\Delta_i$), this error is proportional to $\Delta_i(r-1)$.

For this reason and in order to simplify the Eulerian-Lagrangian data transmission, the grids used here will be uniform, i.e. $r = 1$, in the region next to the body, while it will be stretched by a factor $\gtrsim 1$ far away from it.

Spatial operators

All the differential operators described in Section 3.1 need to be discretized on the numerical grid in order to be applied on a discretized field. As the mesh is structured, the fields can be stored in a regular matrix, in which the column-wise direction corresponds to the x-axis, and the row-wise direction to the y-axis. In our code, all but the non-linear operator $\mathbf{N}(\cdot) = \mathbf{u} \cdot \nabla(\cdot)$ are defined as matrices and the effect of an operator on a certain field is given by the row-column product of the two matrices.

For computational reasons it is also useful to define some interpolation operators by which we can evaluate the same variable at different locations: from cell faces (velocity nodes) to cell centers (pressure nodes) and from cell faces to cell corners. Even if other choices are possible, these operators are written in a local form (i.e. looping over the whole domain instead of considering all nodes at the same time).

Table 5.1.1 reports the action of each spatial operator including the spatial location of points on which it operates and at which it returns the output. We stress the importance of this asymmetry, since pressure gradient operators $\mathbb{G}_x$ and $\mathbb{G}_y$ (that operate at cell centers $\times$ where the pressure field p is defined) will be needed to evaluate the velocity field at cell faces ($\rightarrow$ and $\uparrow$).

Conversely, the divergence-free constraint will be evaluated at cell centers $\times$ by applying the divergence operators $\mathbb{D}_x$ and $\mathbb{D}_y$ on velocity fields u_x and u_y that are defined respectively at $\rightarrow$ and $\uparrow$. As an example, let us calculate the gradient of the pressure field p in the x direction and for simplicity let us assume periodic boundary conditions. As previously described, this operation results in the row-column product $\mathbb{G}_x p$. As stated in Table 5.1.1 and Figure 5.1.1, the pressure field is evaluated at cell centers $\times$, while its gradient along x will result on cell faces $\rightarrow$.

Operator	Operates on	Returns values at	Size
$\mathbb{D}_x$	$\rightarrow$	$\times$	$(N_x \times N_x - 1)$
$\mathbb{D}_y$	$\uparrow$	$\times$	$(N_y \times N_y - 1)$
$\mathbb{G}_x$	$\times$	$\rightarrow$	$(N_x - 1 \times N_x)$
$\mathbb{G}_y$	$\times$	$\uparrow$	$(N_y - 1 \times N_y)$
$\mathbb{L}_x$	$\rightarrow$	$\rightarrow$	$(N_x - 1 \times N_x - 1)$
$\mathbb{L}_y$	$\uparrow$	$\uparrow$	$(N_y - 1 \times N_y - 1)$

Table 5.1.1: Size of spatial operator matrices with Dirichlet Boundary conditions: p is computed at the center of the cell, while u and v respectively at the vertical and horizontal faces of the cell.

Let us call n_{gx} and n_{gy} the number of geometries and n_{cx} and n_{cy} the number of centers along x and y (refer to Section 5.1.1 for definitions), so p will have dimensions (n_{cx}, n_{cy}) and u_x (n_{gx}, n_{cy}). The operator $\mathbb{G}_x$ will then have dimensions (n_{gx}, n_{cx}). The effect of the product between the i^{th} row of $\mathbb{G}_x$ on the j^{th} column of p will be the pressure gradient in the x direction evaluated at the u_x node $(\rightarrow)$ located at the i^{th} value of geometries and at the j^{th} value of centers (Figure 5.1.2). In the following we will describe all discrete spatial operators, including the part of the code in which they come into play.

Divergence The divergence operator returns the divergence of the input velocity field $\mathbf{u} = (u, v)$. It is used to compute the known column vector of the Poisson equation in the second step of the Fractional Step Method and to check the flow incompressibility at each time step. This operator is applied at velocity nodes and returns the value at pressure nodes.

Gradient The gradient operator returns the gradient of the input pressure field p. It partially forms the known column vector $\mathbf{r}$ of the first step of the Fractional Step Method. This operator is applied at pressure nodes and returns the value at velocity nodes.

Laplacian The Laplacian operator returns the Laplacian of each component of the input velocity field $\mathbf{u} = (u, v)$. It partially forms the known column vector $\mathbf{r}$ of the first step of the Fractional Step Method. This operator is applied at velocity nodes and returns the value at the same location.

Non-linear operator The non-linear operator is written in the conservative form as

$$\begin{aligned} \mathbf{u} \cdot \nabla \mathbf{u} = u_j \frac{\partial u_i}{\partial x_j} = \frac{\partial}{\partial x_j}(u_i u_j) &= (\frac{\partial u^2}{\partial x} + \frac{\partial uv}{\partial y} \ , \ \frac{\partial uv}{\partial x} + \frac{\partial v^2}{\partial y}) \\ &\simeq (N_x, N_y)_{i,j} \end{aligned}$$

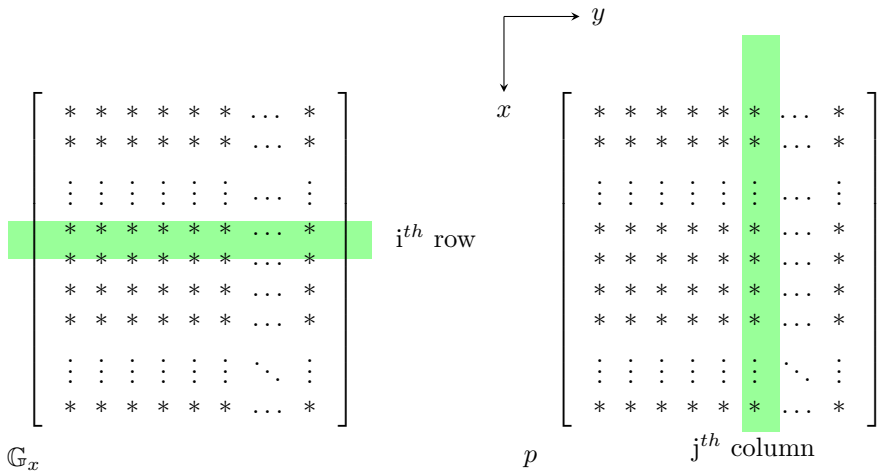

Figure 5.1.2: Action of the matrix operator to evaluate the differential operator at a particular point of a generic input field.

and is discretized with a two-step Adam-Bashforth (or with a Euler forward at the first time step), appearing in the known column vector $\mathbf{r}$ of the first step of the Fractional Step Method. The evaluation of this operator requires the interpolation of u_x and u_y at both cell centers ($\times$) and cell corners ($+$). The stencil for N_x is shown in Figure 5.1.3.

5.2 Boundary Conditions

To fully understand the reason for boundary terms to appear we need to introduce the so-called *computational domain*, the ensemble of all grid nodes at which variables are unknown.

The stencil of the spatial operators, i.e. the set of points needed to compute the value of a differential operator, usually overflow the computational domain involving nodes on the boundary or beyond. In the case of points near boundaries, stencils have to be modified in order to be considered at boundary nodes. In this way values of variables or their derivatives at boundaries, the so-called *boundary conditions* needed to solve differential equations, become part of the right-hand-side of our linear system (bc).

In the following we present the most used kinds of boundary conditions. As stated in [49], §3, by implementing boundary conditions before any splitting takes place, no boundary conditions on intermediate velocity $\mathbf{u}^*$ and p are

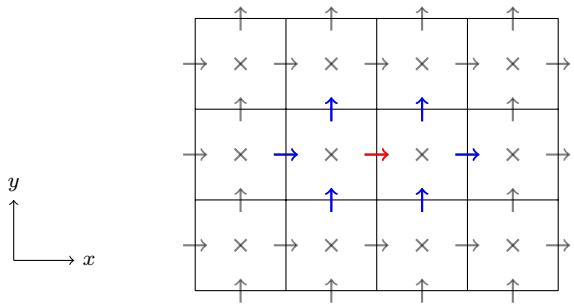

Figure 5.1.3: Non-linear operator stencil (in blue) for an x-component velocity node (in red).

required. Thus, only boundary conditions on velocity $\mathbf{u}$ are required.

In order to simulate an open flow around a flexible body, the following boundary conditions are used; Dirichlet boundary at inlet, symmetric boundary conditions at sides and convective boundary conditions at outlet. These boundary conditions are discussed in detail in the following sections.

5.2.1 Symmetry Boundary Conditions

It is sometimes useful to impose this kind of condition on boundaries through which there is no mass flux, but where no solid walls are present. This can be the case of external flows with boundaries very far from the body. This kind of condition implies

$$(\mathbf{u}\cdot\mathbf{n})_\Gamma = 0 \quad ; \quad \left.\frac{\partial(\mathbf{u}\cdot\boldsymbol{\tau})}{\partial\mathbf{n}}\right|_\Gamma = 0$$

i.e. the velocity component normal to the boundary is required to be zero (Dirichlet condition), while the normal derivative to the boundary of the tangential component is zero (Neumann condition). These are *homogeneous* boundary conditions, and generate no boundary condition vectors in the discretized equations.

5.2.2 Dirichlet Boundary Conditions

The velocity of the fluid is usually known at inlets, and therefore it is convenient to use it as a boundary condition, resulting in *inhomogeneous* Dirichlet boundary conditions.

$$\mathbf{u}|_\Gamma = f(s)$$

where s is the curvilinear coordinate of the boundary.

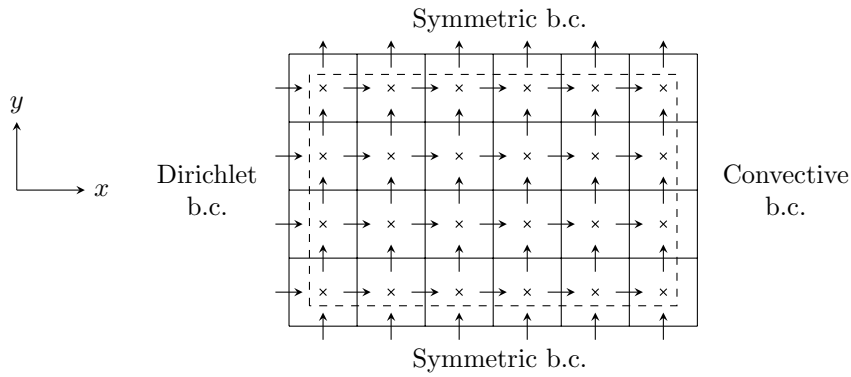

Figure 5.2.1: Staggered grid with applied boundary conditions (b). The dashed line encloses the computational domain.

5.2.3 Convective Boundary Conditions

Boundary conditions at outlets are often modeled with a homogeneous Neumann boundary condition (i.e. $\partial\mathbf{u}/\partial\mathbf{n}$) for steady simulations. However, this condition is not satisfactory in an unsteady case, where it is better to apply a *convective* boundary condition. A number of such conditions have been tried but the one that appears to work well is also one of the simplest ([47], p. 273):

$$\frac{\partial\mathbf{u}}{\partial t} + U\frac{\partial\mathbf{u}}{\partial\mathbf{n}} = 0$$

where U is a velocity independent of the location and chosen such that overall mass in the domain is conserved. This is a particular case of the Dirichlet boundary condition in which the boundary value changes in time.

In the numerical discretization the previous boundary condition can be implemented by using antime explicit time scheme:

$$\frac{\mathbf{u}_b^{n+1} - \mathbf{u}_b^n}{\Delta t} + UD(\mathbf{u})_b^n = 0$$

where D is the spatial derivative operator. Since the derivative has to be extrapolated from the computational domain, we can obtain the stencil by the *Method of Undetermined Coefficients* ([86], §1.2).

5.3 Time discretization

In computing unsteady flows, we have a fourth coordinate direction to consider: time. As with spatial coordinates, it must be discretized. We can consider the time "grid" as discrete points in a prescribed time interval, just like the spatial discretization.

The major difference between the time and the space coordinates lies in the direction of influence: whereas a force at any space location may (in elliptic problems) influence the flow anywhere else, forcing at a given instant will affect the flow only in the future, i.e. there is no backward influence. Unsteady flows are, therefore, parabolic in time, so all solution methods advance in time in a step-by-step or "marching" manner.

When trying to solve a PDE (partial differential equation) with both time and spatial derivatives, we can first evaluate all spatial operators and then treat them as forcing (known) terms: in this way we can think of the evolution in time as ruled by an ODE (ordinary differential equation) with an initial value problem.

Here we use an explicit two-point Adams-Bashforth scheme, as in [49], to evaluate convective terms and an implicit Crank-Nicholson (trapezoidal) scheme for diffusive terms (Euler forward is used for the first time step). This is because the Laplacian operator (diffusive terms) is linear, so it can be directly written in a matricial form, whereas the non-linear operator (convective term) would have required a further linearization to be inverted.

Crank-Nicholson method This method approximates the integral with a straight line interpolation between the initial and final points to construct the approximation

$$\phi^{n+1} = \phi^n + \frac{\Delta t}{2}[f(t_n, \phi_n) + f(t_{n+1}, \phi_{n+1})]$$

This method is implicit (ϕ_{n+1} appears on the right hand side) and is called two-level method because it involves the values of the unknown at only two times (ϕ_{n+1} and ϕ_n).

Two-point Adams-Bashforth method This method belongs to the so-called multipoint methods, that approximate the integral by integration of a polynomial function created via Lagrangian interpolation at a certain number of points (in this case t_n and t_{n-1}). This can be written as

$$\phi^{n+1} = \phi^n + \frac{\Delta t}{2}[3f(t_n, \phi_n) - f(t_{n-1}, \phi_{n-1})]$$

This method is explicit (ϕ_{n+1} does not appear on the right hand side) and is a three-level method because it involves the values of the unknown at

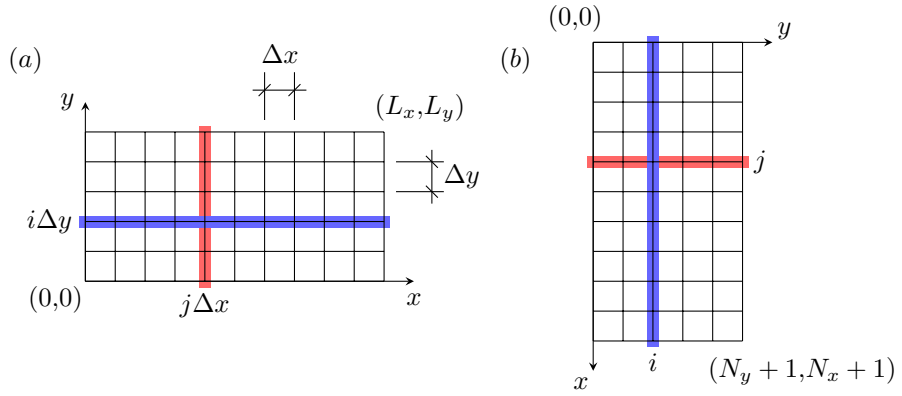

Figure 5.4.1: Computational domain (a) and data field storage in matrix form (b), where $L_x = N_x\Delta x$, $L_y = N_y\Delta y$.

three times (ϕ_{n+1}, ϕ_n and ϕ_{n-1}). The major drawback of this method is that, because it requires data from many points prior to the current one, it cannot be started using only data from initial conditions. Other methods have to be used to compute the initial time steps.

5.4 Matrix description

In order to perform operations in a simple and effective way, both data fields and spatial operators are described by matrices.

5.4.1 Data storage

Each data field is described by a matrix having the number of columns equal to the number of computational nodes along the x-direction, and the number of rows equal to number of computational nodes along the y-direction.

Depending on the particular boundary conditions we have different matrix dimensions for different data fields.

Periodic Boundary Conditions In this simple case the computational domain is the same as the physical domain, so each data field has to be evaluated at $N_x \times N_y$ computational nodes.

Dirichlet Boundary Conditions In this case the computational domain differs from the physical domain, and each data field has different computational dimensions (Table 5.4.1).

Data field	size
u	$(N_x - 1 \times N_y)$
v	$(N_x \times N_y - 1)$
cell centers (p)	$(N_x \times N_y)$
cell faces	$(N_x - 1 \times N_y - 1)$

Table 5.4.1: Dimensions of data matrices using Dirichlet Boundary Conditions, as for example in Figure 5.2.1

Spatial operator (size)	Input matrix (size)	Output matrix (size)
G_x $(N_x - 1 \times N_x)$	uu $(N_x \times N_y)$	$G_x \cdot uu$ $(N_x - 1 \times N_y)$
G_y $(N_y - 1 \times N_y)$	vv^T $(N_y \times N_x)$	$(G_y \cdot vv^T)^T$ $(N_x \times N_y - 1)$
D_x $(N_x \times N_x - 1)$	uv $(N_x - 1 \times N_y - 1)$	$D_x \cdot uv$ $(N_x \times N_y - 1)$
D_y $(N_y \times N_y - 1)$	uv^T $(N_y - 1 \times N_x - 1)$	$(D_y \cdot uv^T)^T$ $(N_x - 1 \times N_y)$
L_{ux} $(N_x - 1 \times N_x - 1)$	u $(N_x - 1 \times N_y)$	$L_{ux} \cdot u$ $(N_x - 1 \times N_y)$
L_{uy} $(N_y \times N_y)$	u^T $(N_y \times N_x - 1)$	$(L_{ux} \cdot u^T)^T$ $(N_x - 1 \times N_y)$
L_{vx} $(N_x \times N_x)$	v $(N_x \times N_y - 1)$	$L_{vx} \cdot u$ $(N_x \times N_y - 1)$
L_{vy} $(N_y - 1 \times N_y - 1)$	v^T $(N_y - 1 \times N_x)$	$(L_{vy} \cdot v^T)^T$ $(N_x \times N_y - 1)$
I_{uc} $(N_x \times N_x - 1)$	u $(N_x - 1 \times N_y)$	$I_{uc} \cdot u$ $(N_x \times N_y)$
I_{un} $(N_y - 1 \times N_y)$	u^T $(N_y \times N_x - 1)$	$(I_{un} \cdot u^T)^T$ $(N_x - 1 \times N_y - 1)$
I_{vc} $(N_y \times N_y - 1)$	v^T $(N_y - 1 \times N_x)$	$(I_{vc} \cdot v^T)^T$ $bo(N_x \times N_y)$
I_{vn} $(N_x - 1 \times N_x)$	v $(N_x \times N_y - 1)$	$I_{vn} \cdot v$ $(N_x - 1 \times N_y - 1)$

Table 5.4.2: Spatial operators size under Dirichlet Boundary Conditions.

5.4.2 Spatial operators

As described in Section 5.1, in order to solve for the flow field we have to manipulate fields with different spatial operators. Here we also define spatial operators in matrix form so that the application of a spatial operator on a data field is simply computed by a row-column multiplication.

Due to their non-linearity, the convective operators N_x and N_y cannot be described as matrices, i.e. they will not be evaluated implicitly but will be taken into account on the right hand side.

The size of each matrix depends upon the specific boundary conditions since they have to operate on the data matrices. Moreover, because of the staggered grid arrangement, it is not true in general that the original operator matrix and the resulting field matrix have the same dimension (see Table 5.4.2).

5.5 Validation

In this Section we will go through the benchmark problems that have been selected to test the validity of the code.

5.5.1 Simulation of a vortex flow field

The first validation test of the code concerns the spatial convergence rate in a simulation with periodic boundary conditions, where a second-order accuracy in both time and space is expected. The chosen problem was the simulation of the Taylor-Green array of vortices, whose time-dependent behaviour is described in a closed form as

$$u_{ref}(x,y,t) = -\cos(k_x x)\sin(k_y y)e^{-t(k_x^2+k_y^2)/Re}$$

$$v_{ref}(x,y,t) = -\sin(k_x x)\cos(k_y y)e^{-t(k_x^2+k_y^2)/Re}$$

$$p_{ref}(x,y,t) = -\frac{1}{4}[\cos(2k_x x)+\sin(2k_y y)]e^{-t(k_x^2+k_y^2)/Re}$$

that has be taken as a reference solution to compute the error ε defined as

$$\varepsilon = \|u-u_{ref}\|_\infty + \|v-v_{ref}\|_\infty \tag{5.5.1}$$

The simulation has been run with the following parameters

$$Re = 10, \quad L_x = 3, \quad L_y = 3, \quad n_x = 2^4, \quad n_y = 2^4,$$

$$\Delta t = 0.01, \quad T_{end} = 1.2$$

Results of the time convergence analysis are listed in Table 5.5.1. Figure 5.5.1 shows the same results as Table 5.5.1 compared with an analytical solution with first and second order accuracy: it is possible to see how the obtained results overlap almost exactly the second-order convergence.

Δt	ε	convergence rate
$1 \cdot 10^{-4}$	$3.5 \cdot 10^{-11}$	\
$2 \cdot 10^{-4}$	$1.4 \cdot 10^{-10}$	2.000
$4 \cdot 10^{-4}$	$5.8 \cdot 10^{-10}$	2.051
$8 \cdot 10^{-4}$	$2.3 \cdot 10^{-9}$	1.988
$1 \cdot 10^{-3}$	$3.6 \cdot 10^{-9}$	2.008
$2 \cdot 10^{-3}$	$1.5 \cdot 10^{-8}$	2.059
$4 \cdot 10^{-3}$	$5.9 \cdot 10^{-8}$	1.976
$8 \cdot 10^{-3}$	$2.3 \cdot 10^{-7}$	1.963
$1 \cdot 10^{-2}$	$3.7 \cdot 10^{-7}$	2.131
$2 \cdot 10^{-2}$	$1.5 \cdot 10^{-6}$	2.019
$4 \cdot 10^{-2}$	$5.9 \cdot 10^{-6}$	1.976
$8 \cdot 10^{-2}$	$2.4 \cdot 10^{-5}$	2.024

Table 5.5.1: Temporal convergence of the implemented code: as expected the convergence rate approximates the theoretical value of 2.

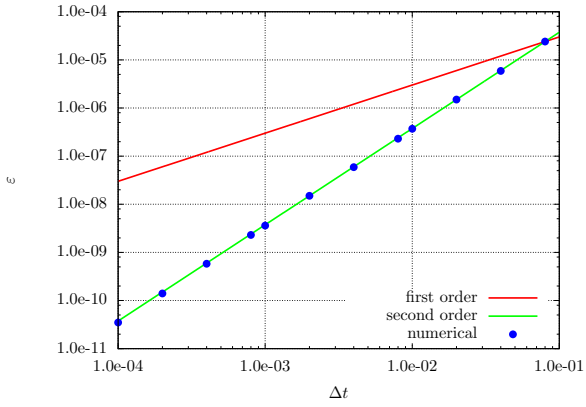

Figure 5.5.1: Temporal convergence rate of the numerical code (dots) compared with the theoretical first- and second-order error curves.

$\Delta x = \Delta y$	$n_x = n_y$	ε	convergence rate
$7.8 \cdot 10^{-3}$	128	$2.0 \cdot 10^{-5}$	\
$1.5 \cdot 10^{-2}$	64	$8.0 \cdot 10^{-5}$	2.044
$3.1 \cdot 10^{-2}$	32	$3.1 \cdot 10^{-4}$	1.949
$6.3 \cdot 10^{-2}$	16	$1.2 \cdot 10^{-3}$	1.849
$1.3 \cdot 10^{-1}$	8	$3.7 \cdot 10^{-3}$	1.628

Table 5.5.2: Spatial convergence of the implemented code: the numerical convergence rate is next to the theoretical value of 2 (see Figure 5.5.2).

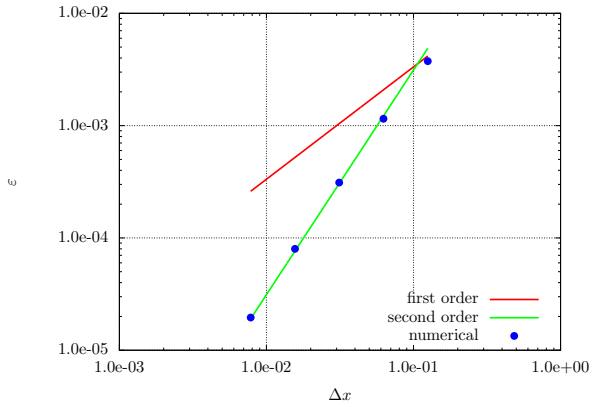

Figure 5.5.2: Spatial convergence rate of the numerical code (dots) compared with the theoretical first- and second-order error curves.

A spatial convergence analysis was also performed. As with the temporal analysis, results are listed in Table 5.5.2 and shown in Figure 5.5.2.

5.5.2 Simulation of an elastic membrane

As a second test on code reliability we compared the results of our code with the ones reported by Griffith in [48], where the dynamics of a thin, elastic and mass-less membrane immersed in a viscous incompressible fluid was performed.

The fluid is taken initially at rest and the membrane is an ellipse with semi-major axis 0.3 and semi-minor axis 0.2. After the membrane is released at time t=0, the interface undergoes damped oscillations, with period and damping depending on the stiffness κ and the Reynolds number Re. Due to the incom-

pressibility of the fluid enclosed by the membrane and the presence of fluid viscosity, the membrane relaxes towards a circular configuration with radius $\sqrt{6}/10$.

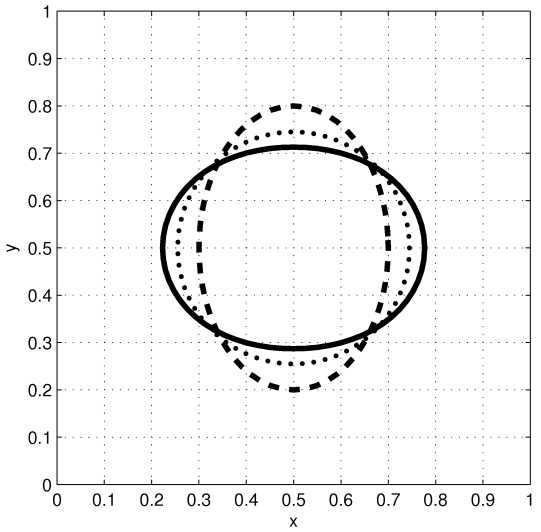

Figure 5.5.3: Membrane (continuous line) deforms from its original configuration (dashed line) towards the final configuration (dotted line).

In the simulations we considered three boundary stiffnesses ($\kappa = 1, 10, 100$) and two Reynolds numbers ($Re = 100, 1000$). We performed each computation until $t = 1.2$ dimensionless time units, which for $\kappa = 1$ corresponds to three damped oscillations. We used Cartesian grids with 16, 32 and 64 points in each coordinate direction, while the elliptic boundary was described with 64 Lagrangian points. All the simulations were conducted with CFL= 0.1. Table 5.5.3 compares the results from our numerical code with those reported in [48]. Although the accuracy is not satisfactory, over all simulations both codes, implemented with different versions of the IB, give the same order of magnitude of area losses. For this kind of test, we assumed as the measure of the accuracy of the method the percentage loss of area inside the membrane:

$$\varepsilon = \frac{|Area - Area_0|}{Area_0} \cdot 100$$

κ	Re	ε_{code}	$\varepsilon_{Griffith}$	$\lvert rel_{err}\rvert$
1	$1 \cdot 10^2$	$6.41 \cdot 10^{-2}$	$3.69 \cdot 10^{-2}$	0.269
	$1 \cdot 10^3$	$2.26 \cdot 10^{-1}$	$3.56 \cdot 10^{-1}$	0.223
10	$1 \cdot 10^2$	$3.33 \cdot 10^{-1}$	$3.95 \cdot 10^{-1}$	0.085
	$1 \cdot 10^3$	$8.90 \cdot 10^{-1}$	$1.90 \cdot 10^{0}$	0.362
100	$1 \cdot 10^2$	$2.33 \cdot 10^{0}$	$1.23 \cdot 10^{0}$	0.310
	$1 \cdot 10^3$	$3.90 \cdot 10^{0}$	$5.76 \cdot 10^{0}$	0.193

Table 5.5.3: Maximum area losses in our numerical code (ε_{code}) compared with those listed in [48]. In all the simulations the Cartesian grid was [64 × 64] and CFL= 0.1

5.5.3 Lid-driven cavity

In order to test the Dirichlet boundary condition, simulation of the so-called "regularized lid-driven cavity" has been performed. In this standard benchmark problem the fluid domain is a box of coordinates $(0 \leq x \leq 1, 0 \leq y \leq 1)$ bounded by still walls except for the top wall, sliding with a tangential velocity u defined as:

$$u(x) = \begin{cases} \sin^2\left[\dfrac{\pi x}{1-p}\right] & \text{if } x \leq \dfrac{1-p}{2} \\ 1 & \text{if } \dfrac{1-p}{2} \leq x \leq \dfrac{1+p}{2} \\ \sin^2\left[\dfrac{\pi(x-1)}{1-p}\right] & \text{otherwise.} \end{cases} \tag{5.5.2}$$

where p is the wall percentage at which $u = 1$ (Figure 5.5.4). The grid and grid size distribution used for simulations as well as velocity profiles are shown in Figure 5.5.5.

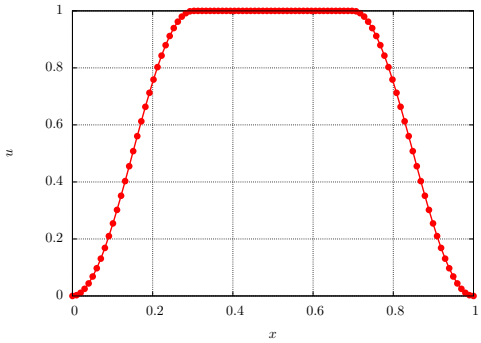

Figure 5.5.4: Regularized tangential velocity profiles along sliding wall for $p = 0.4$.

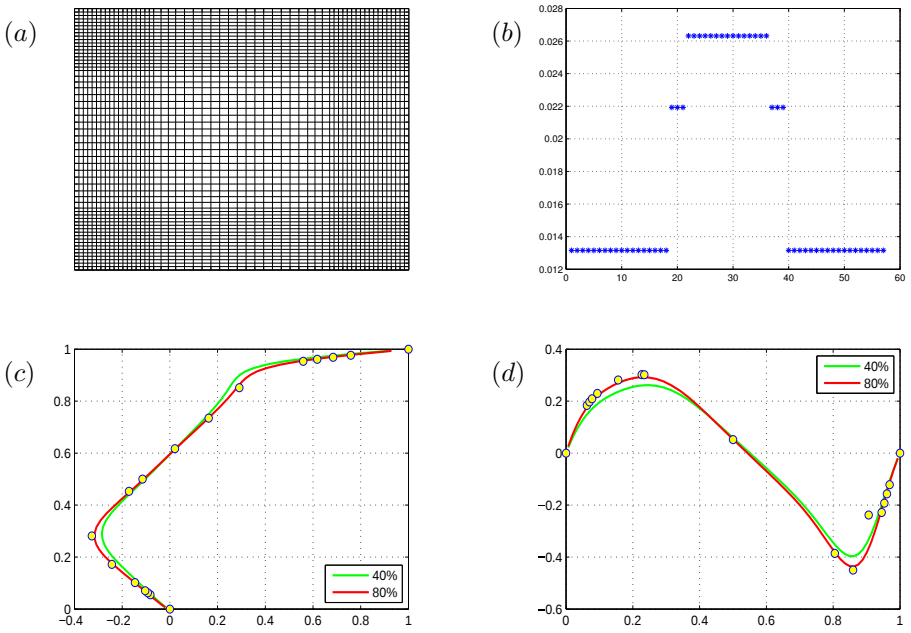

Figure 5.5.5: Stretched grid used for the simulation (a) and grid steps distribution along x (b). u (c) and v (d) velocity profiles at, respectively, $x = 0.5$ and $y = 0.5$ for different percentage of sliding wall velocity profile (Eq. (5.5.2)). Dots in (c) and (b) represent the profiles simulated in [89].

5.5.4 Parachute

In order to test the IB formulation by Peskin (see Section 4.2), a test case regarding a parachute has also been carried out for the simulation of the flux around a massless 2D opening parachute, bonded by two ropes to a pinned point. Boundary conditions in all directions are periodic, and the velocity $\mathbf{u}_0 = (u, v)$ is forced to be $\mathbf{u}_0 = (0, 1)$ at the bottom boundary. This is accomplished by applying a volume force $\mathbf{f}_0$ inside a strip Ω near the inlet:

$$\mathbf{f}_0(\mathbf{x}, t) = \begin{cases} \alpha_0(\mathbf{u}_0(t) - \mathbf{u}(\mathbf{x}, t)) & \text{if } \mathbf{x} \in \Omega \\ 0 & \text{otherwise.} \end{cases} \tag{5.5.3}$$

where α_0 is a large positive constant.

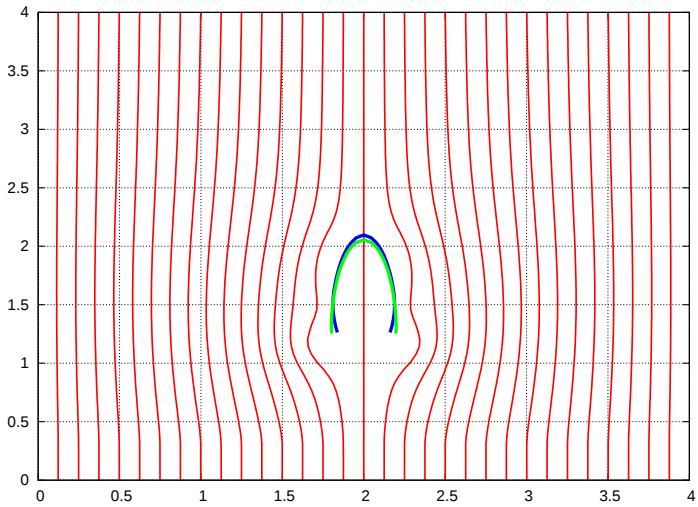

Figure 5.5.6: Streamlines (in red) around the opening parachute (in blue). The initial position of the parachute is shown in green.

Here the permeability has been simulated using the original approach proposed by Kim and Peskin [68] and described here in 4.4.2, i.e. by allowing a relative slip between the flow velocity $\mathbf{U}$ and the structure velocity $\partial\mathbf{X}/\partial t$ in the direction normal to the structure

$$\left(\mathbf{U} - \frac{\partial \mathbf{X}}{\partial t}\right) \cdot \mathbf{n} = \frac{\beta\gamma}{|\partial\mathbf{X}/\partial s|^2} \mathbf{F} \cdot \mathbf{n}$$

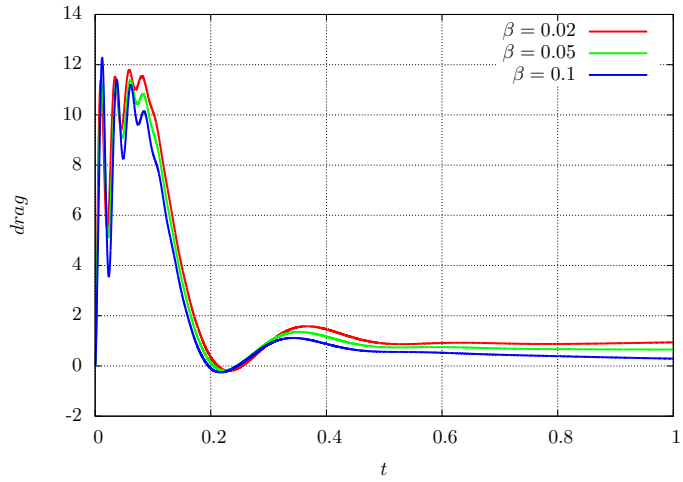

Figure 5.5.8: Time history of drag force on the pinned point.

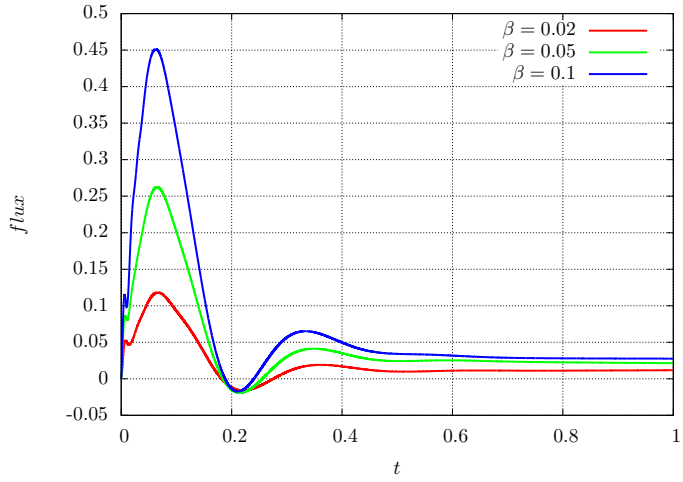

Figure 5.5.7: Time history of flux through canopy.

In the performed simulations the term $\gamma/\left|\partial\mathbf{X}/\partial s\right|^2$ has been set as a constant and equal to 1. Figure 5.5.4 depicts the streamlines around the parachute in the transient between the initial (green) and the actual (blue) configuration. Figures 5.5.7 and 5.5.8 represent respectively the flow through the canopy and the drag force on the pinned point for different values of the pore density β (the aerodynamic conductance is constant and equal to $\gamma = 1$). As expected, the flow through the canopy increases with β while the drag force decreases.

5.5.5 Beam dynamics

In order to also assess the reliability of the structural part of the code some numerical simulations of both the clamped and the hinged beam (without surrounding fluid) have been performed. For each case the initially deformed configuration was free to evolve without any external driving force, so that in the limit of small initial displacement numerical simulations give us both eigenvalues and eigenfunctions. The numerical simulations are in good agreement with the theoretical results shown in Section 2.4.

Clamped beam

In the following we show the result of the simulations of the unforced clamped beam for the first two modes. Since we want to show just one of the eigenfunctions at a time, the initial condition has been set proportional to one of the eigenfunctions depicted in Figure 2.4.1.

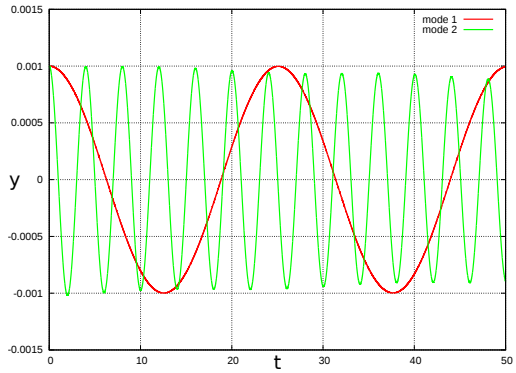

Figure 5.5.9: Time trace of displacement at the clamped beam's free end.

Looking at the displacement of a single point over time Figure (5.5.9), a sinusoidal behavior appears as expected (apart from a little damping) with frequency given in Table 5.5.4, showing a good agreement with the theoretical values shown in Table 2.4.1.

mode	T	f	$\omega_N L^2/\sqrt{\gamma}$
1	25.1381	0.0398	3.5348
2	4.0221	0.2486	22.0924

Table 5.5.4: Oscillation frequencies of simulated modes of the clamped beam.

Figures 5.5.10 and 5.5.11 show different snapshots during one oscillation period of the beam displacement (eigenfunction) respectively for the first and the second mode.

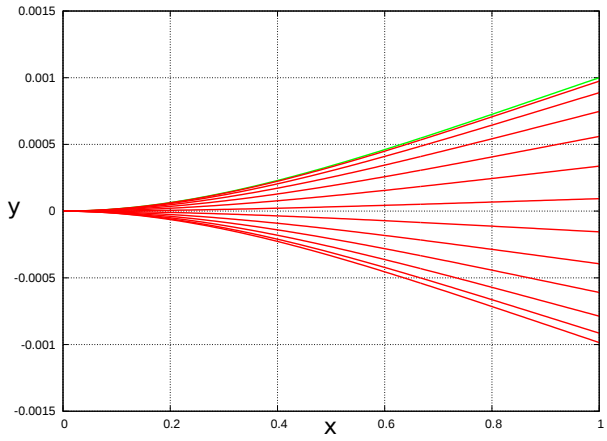

Figure 5.5.10: Beam snapshots during one oscillation. Initial condition (in green) is such that only the first oscillation mode of the clamped beam is excited.

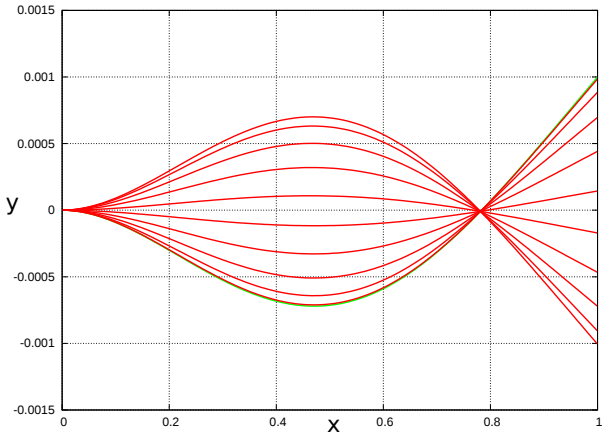

Figure 5.5.11: Beam snapshots during one oscillation. Initial condition (in green) is such that only the second oscillation mode is excited.

Hinged beam

Numerical simulations of the unforced simulation have also been performed for the hinged beam. As for the cantilever, the first two oscillation modes have been investigated.

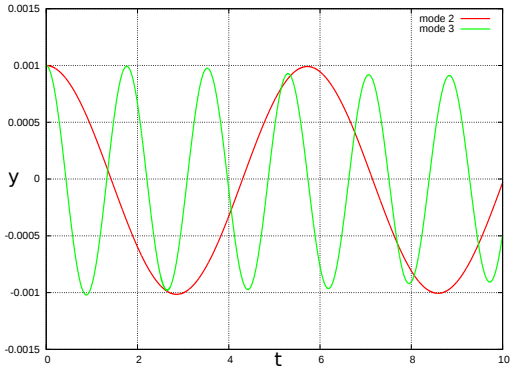

Figure 5.5.12: Time trace of displacement at the hinged beam's free end.

Looking at the displacement of a single point over time (Figure 5.5.12), a sinusoidal behavior appears as expected (apart from a little damping) with frequency reported in Table 5.5.5 showing good agreement with the theoretical values shown in Table 2.4.2.

mode	T	f	$\omega_N L^2/\sqrt{\gamma}$
2	5.7264	0.1746	15.5173
3	1.7686	0.5654	50.2415

Table 5.5.5: Oscillation frequencies of simulated modes of the hinged beam.

Figures 5.5.13 and 5.5.14 show different snapshots during one oscillation period of the beam displacement (eigenfunction), respectively, for the first and the second non-trivial oscillation mode.

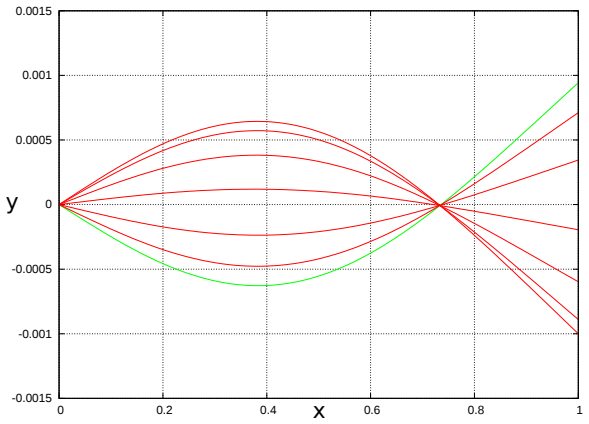

Figure 5.5.13: Beam snapshots during one oscillation. Initial condition (in green) is such that only the second oscillation of the hinged beam mode is excited.

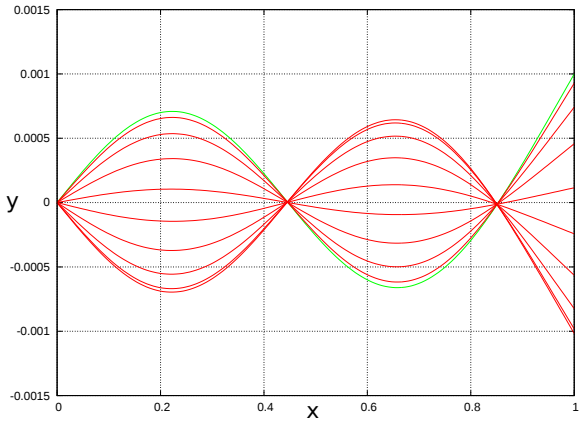

Figure 5.5.14: Beam snapshots during one oscillation. Initial condition (in green) is such that only the third oscillation mode of the hinged beam is excited.

5.5.6 Darcy's law

The physical accuracy of the results has been tested with the well-established Darcy's law by simulating a porous membrane hinged at both ends perpendicular to an incoming uniform flow (see Figure 5.5.15).

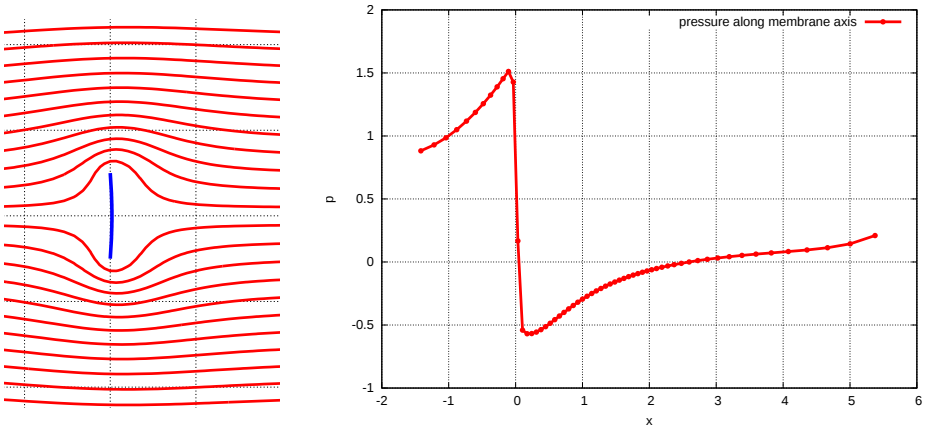

Figure 5.5.15: An inextensible membrane (left, solid line) simply supported at both ends is subject to a uniform flow from left (streamlines in dot lines) and (right) pressure profile along x. Notice the sudden pressure drop around membrane location ($x \simeq 0$) within the space of two mesh grids.

In the next subsection we will derive the theoretical relationship between Darcy's permeability coefficient k and the parameter λ used in our model, while in subsection 5.5.7 the numerical procedure and results will be shown.

Theoretical derivation of the $k - \lambda$ mapping

Darcy's law is a phenomenological relationship describing the flow in porous media in the limit of laminar flow (low Reynolds numbers). It states a linear dependence between the pressure gradient ∇p and the fluid velocity $\mathbf{U} - \mathbf{U}_{ib}$ through the so-called permeability coefficient k, that takes into account the geometry of the porous medium:

$$\mathbf{U} - \mathbf{U}_{ib} = -k\nabla p \tag{5.5.4}$$

where $\mathbf{U} - \mathbf{U}_{ib}$ is the fluid relative slip velocity across the permeable medium. In our numerical simulation the force exerted by the fluid on the filament is given by Goldstein's feedback law (6.1.2), that by neglecting the time-integral term can be written as $\mathbf{F} = \beta(\mathbf{U} - \mathbf{U}_{ib})$. Since the drag on a flat plate normal to the flow is only due to the pressure difference we can approximate

$$\frac{F}{\delta} \sim \frac{\partial p}{\partial x} \tag{5.5.5}$$

where δ is the width of the membrane, given by the "effective radius" of the Dirac delta function used by the IB method. In our case, δ has been estimated to be twice the minimum grid spacing, i.e. $\delta = 2\Delta x_{min} = 2\Delta y_{min}$. Finally, exchanging the normal direction $\mathbf{n}$ with the x-direction one obtains

$$k = -\frac{\delta}{\beta(1-\lambda)} \tag{5.5.6}$$

5.5.7 Numerical results

Several simulations were performed with different values of λ and four different Reynolds number $(2.5, 5, 7.5, 10)$. By sampling pressure immediately upstream and down-stream of the membrane along the x axis (Figure 5.5.15, left) we got the pressure gradient across the membrane, while flow measurements were obtained by interpolating the fluid velocity on the membrane.

The linear relationship between pressure gradient and the fluid flux across the membrane (Figure 5.5.16, left) is in good agreement with Darcy's law at low Reynolds numbers. Darcy's k parameter for each value of λ was thus obtained

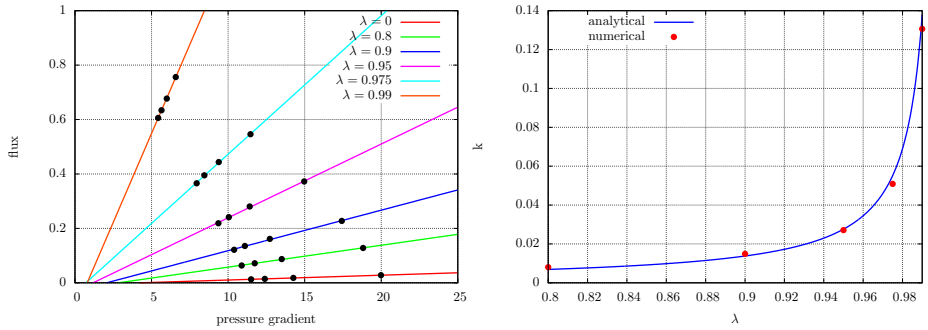

Figure 5.5.16: Linear regression of every set of simulations (dots) at different λ (left). Darcy's k is the slope of each line and comparison between analytical prediction and numerical results of the $k - \lambda$ mapping (right).

through a linear regression of the simulation results, leading to a numerical mapping curve ($\lambda - k$) (Figure 5.5.16, right) that shows good agreement with the analytical prediction curve from equation (5.5.6).

6

Applications and results

6.1 Permeable filament

Motion of deformable, slender structures immersed in an incompressible viscous fluid is commonly seen in natural phenomena, and can be found in many applications such as paper processing [91], energy harvesting [60, 62, 63] and turbulence reduction [90].

In the present paper we study numerically how permeability, a key factor in a number of both biological and technological tissues, plays a role in the dynamics of a flapping hinged filament, commonly referred to as the flag-in-the-wind problem.

6.1.1 Problem formulation and characteristic length scales

We consider a one-dimensional inextensible elastic filament of length L^*, with mass per unit length ρ_S^* and bending rigidity K_b^*, surrounded by a viscous incompressible fluid of density ρ_F^*, dynamic viscosity ν^* and velocity at inflow U_∞^*. As in [52], we also make use of the density difference $\rho_1^* = \rho_S^* - \rho_F^* A^*$, where A^* is the filament cross section area (dimensional variables with star, dimensionless without).

The dimensional governing equations (4.3.5) and (4.3.6) can be made dimensionless by using the same characteristic scales as described in Section 4.3, giving equations (6.1.6) and (6.1.1).

While section 5.5.6 contains the numerical benchmark with Darcy's law, section 6.1.2 describes the numerical method, and the numerical results are discussed in section 6.1.6. The analytical model is presented in 6.1.9, while in section 6.1.8 we try to provide a physical insight into the phenomenon. Finally conclusions are drawn in section 6.1.10.

6.1.2 Numerical model

Let $\mathbf{x} = (x, y) \in \Omega$ be the Cartesian physical coordinates, with Ω denoting the physical domain, x and y being the stream-wise and cross-stream direction, respectively; let $s \in \Gamma$ be the Lagrangian curvilinear coordinate, with Γ denoting the body surface; let $\mathbf{X}(s,t) = (X_1(s,t), X_2(s,t)) \in \Gamma$ denote the physical position of each material point of curvilinear coordinate s at time t (Figure 6.1.1). Velocity boundary conditions are: $\mathbf{u} = (U_\infty, 0)$ at Ω_{inlet}, $\partial\mathbf{u}/\partial t + U_\infty \partial\mathbf{u}/\partial\mathbf{n} = 0$ at Ω_{outlet} (convective boundary condition) and $\{\mathbf{u}\cdot\mathbf{n} = 0,\ \partial(\mathbf{u}\cdot\boldsymbol{\tau})/\partial\mathbf{n} = 0\}$ at Ω_{top} and Ω_{bottom} (symmetrical boundary condition), where $\mathbf{n}$ and $\boldsymbol{\tau}$ are, respectively, the normal and tangential directions to the boundary. Given these conditions, the governing equations can be written as:

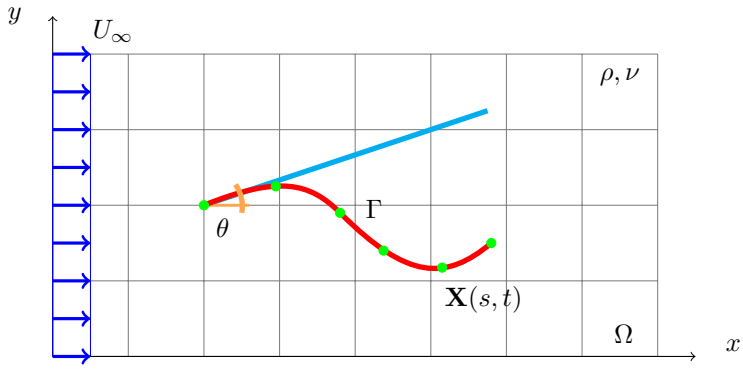

Figure 6.1.1: Filament Γ (in red) described by a set of Lagrangian points $\mathbf{X}(s,t)$ (in green). Initial configuration (in cyan) of the filament is a straight line with a certain angle of attack θ.

$$\begin{cases} \dfrac{\partial \mathbf{u}}{\partial t}(\mathbf{x},t) + \mathbf{u}(\mathbf{x},t)\cdot\nabla\mathbf{u}(\mathbf{x},t) = \\ \qquad\qquad - \nabla p(\mathbf{x},t) + \dfrac{1}{Re}\nabla^2\mathbf{u}(\mathbf{x},t) + \mathbf{f}(\mathbf{x},t) \\ \nabla\cdot\mathbf{u}(\mathbf{x},t) = 0 \end{cases} \tag{6.1.1}$$

$$\mathbf{F}_{imp} = \alpha \int_0^t (\mathbf{U}_{ib} - \frac{\partial \mathbf{X}}{\partial t})dt' + \beta(\mathbf{U}_{ib} - \frac{\partial \mathbf{X}}{\partial t}) \tag{6.1.2}$$

$$\mathbf{F} = (1-\lambda)(\mathbf{F}_{imp}\cdot\mathbf{n})\mathbf{n} + (\mathbf{F}_{imp}\cdot\boldsymbol{\tau})\boldsymbol{\tau} \tag{6.1.3}$$

$$\mathbf{f}(\mathbf{x},t) = \rho \int_\Gamma \mathbf{F}(s,t)\delta(\mathbf{x} - \mathbf{X}(s,t))ds \tag{6.1.4}$$

$$\mathbf{U}_{ib}(s,t) = \int_{\Omega} \mathbf{u}(\mathbf{x},t)\delta(\mathbf{x}-\mathbf{X}(s,t))d\Omega \tag{6.1.5}$$

$$\frac{\partial^2 \mathbf{X}}{\partial t^2} = \frac{\partial}{\partial s}\left(T\frac{\partial \mathbf{X}}{\partial s}\right) - \frac{\partial^2}{\partial s^2}\left(\gamma\frac{\partial^2 \mathbf{X}}{\partial s^2}\right) + Fr\frac{\mathbf{g}}{g} - \mathbf{F} \tag{6.1.6}$$

$$\begin{aligned} \frac{\partial \mathbf{X}}{\partial s}\frac{\partial^2}{\partial s^2}\left(T\frac{\partial \mathbf{X}}{\partial s}\right) &= \frac{1}{2}\frac{\partial^2}{\partial t^2}\left(\frac{\partial \mathbf{X}}{\partial s}\frac{\partial \mathbf{X}}{\partial s}\right) \\ &- \frac{\partial^2 \mathbf{X}}{\partial t \partial s}\frac{\partial^2 \mathbf{X}}{\partial t \partial s} - \frac{\partial \mathbf{X}}{\partial s}\frac{\partial}{\partial s}(\mathbf{F}_b - \mathbf{F}) \end{aligned} \tag{6.1.7}$$

The incompressible Navier-Stokes equations (6.1.1) are considered together with an artificial forcing $\mathbf{f}$ to enforce the no-slip condition. Hydrodynamical forces acting on a permeable filament are calculated by means of eqs. (4.4.5) and (6.1.2), where the first is the force reduction equation presented in Section 1 for taking into account permeability and the second is Goldstein's feedback law [59]. According to [59], α and β are negative constants chosen to enforce the no-slip condition up to an arbitrary small value. Throughout this work, we have used $\alpha = 0$. Equations (6.1.4) and (6.1.5) link together Eulerian and Lagrangian quantities through a convolution with a discretized version of Dirac Delta function δ (interested readers are referred to [67]). Among a wide choice of synthetic Delta functions, we made use of the one proposed by Roma in [69]. As explained in [52], the difference of density scales in the dimensional version of equations (6.1.1) and (6.1.6) (ρ_F^* and ρ_1^*, respectively), is taken into account in equation (6.1.4) through the ratio $\rho = \rho_1^*/(\rho_F^* L^*)$. Filament dynamics is considered in equation (6.1.6), known as d'Alembert elastic string equation. As shown in [52], equation (6.1.7) solves for the tension as a Lagrangian multiplier in order to enforce incompressibility and can be recovered by deriving equation (6.1.6) with respect to s and multiplying by $\partial\mathbf{X}/\partial s$. As in [56], we chose a staggered arrangement of the Lagrangian variables $\mathbf{X}$ and T (see Figure 4.3.1).

In order to solve equation (6.1.6) four boundary conditions are enforced both at the leading and at the trailing edge:

$$\mathbf{X}|_{s=0} = \mathbf{X}_{hinged}, \quad \left.\frac{\partial^2 \mathbf{X}}{\partial^2 s}\right|_{s=0} = 0, \quad \left.\frac{\partial^2 \mathbf{X}}{\partial^2 s}\right|_{s=L} = 0, \quad \left.\frac{\partial^3 \mathbf{X}}{\partial^3 s}\right|_{s=L} = 0.$$

The first and second conditions enforce the filament to be hinged to the pole $\mathbf{X}_{hinged}$, while the third and the fourth conditions state that the filament trailing edge is unloaded (zero torque and shear). Moreover, equation (6.1.7) is solved together with these conditions:

$$\left.\frac{\partial}{\partial s}\left(T\frac{\partial \mathbf{X}}{\partial s}\right)\right|_{s=0} = -Fr\frac{\mathbf{g}}{g} + \mathbf{F}, \quad T|_{s=L} = 0,$$

where the first one derives from equation (6.1.6) in the absence of acceleration and bending moment (hinged condition), while the second again comes from the unloaded free edge condition.

6.1.3 Numerical Discretization

The computational domain is an 8×8 square ranging $[-2, 6]$ in the cross-stream direction and $[-4, 4]$ in the span-wise direction as in [52]. The computational grid is uniform in an inner region close to the pinned end $(0, 0)$ of the filament ($[-0.5, 3]$ in the cross-stream direction and $[-1, 1]$ in the span-wise direction) with grid spacing $1/75$, and stretched outside with a constant stretching ratio equal to 1.1. A convergence study on grid spacing has been performed up to $1/150$, showing a relative error on flapping amplitude less than 2.5%. The filament length L is set equal to 1 and the Lagrangian grid is made up of 150 points, so that approximately 2 Lagrangian points appear in one Eulerian cell (as suggested in [55]). Boundary conditions on the velocity are $U_\infty = (1, 0)$ at the inflow, convective at the outflow and symmetric at the lateral sides. Since our computational grid for the flow is staggered, no boundary conditions for the pressure are needed. The initial configuration of the filament is a straight line inclined at a certain angle θ (Figure 6.1.1). In all the simulations the fluid kinematic viscosity ν has been calculated to give $Re = 200$.

6.1.4 Numerical scheme

To solve the incompressible Navier-Stokes equations we make use of the Fractional Step Method, a projection method originally introduced independently by Chorin [46] and Temam [51] and later refined by Perot [49]. This formulation results in a code with second-order accuracy in space and first order accuracy in time.

6.1.5 Solution Procedure

At each time step the numerical algorithm can be summarized as follow: (i) evaluation of hydrodynamical forces $\mathbf{F}$ on the filament (6.1.2), (ii) spreading of the force $\mathbf{F}$ from Lagrangian points on the Eulerian grid (6.1.4), (iii) solution of fluid flow (6.1.1), (iv) solution of filament motion (6.1.6), (6.1.7).

6.1.6 Simulations of impermeable filament

Before focusing on permeable filaments, we ran a few simulations in order to validate our numerical method against results available in literature. In particular the analytical model shown in [71] has been taken as a reference for all

numerical simulations. This model considers the beam dynamical equation with external loads given by the "slender body theory" (see Munk [72]), obtaining

$$(\rho + \rho_a)\frac{\partial^2 h}{\partial t^2} + 2\mu_a \frac{\partial}{\partial s}\frac{\partial h}{\partial t} + (\rho_a - \tau)\frac{\partial^2 h}{\partial s^2} + \gamma \frac{\partial^4 h}{\partial s^4} = 0, \tag{6.1.8}$$

having introduced the following non-dimensional quantities:

$$\rho = \frac{\rho_s}{\rho_f L}, \quad \rho_a = \frac{m_a}{\rho_f L}, \quad \tau = \frac{T}{\rho_f U^2 L}, \quad \gamma = \frac{K_b}{\rho_f U^2 L^3}$$

where ρ_s is the structure linear density, ρ_f is the fluid density, $m_a = \rho_f A$ (and therefore $\rho_a = A/L$, giving a dimensionless ratio in 2D) is the "virtual mass" considered to surround the filament cross section. We would like to point out that this equation differs slightly from (6.1.6) in that here we consider the absolute beam density ρ_s in the inertial term and not the density difference ρ_1 required by the Immersed Boundary approach.

This is a fourth order linear equation for $h(s,t)$ involving only second and fourth order derivatives, which leads to simple solutions that exhibit some interesting features. In order to perform a stability analysis, we insert in the previous equation the generic expression of a wave evolving both in time and space

$$h(s,t) = ae^{i(ks-\omega t)}$$

where a is the amplitude, k the wave number and ω the angular frequency.

In order to estimate tension, we use the solution deriving from a zero-pressure gradient boundary layer developing over a flat plate (Blasius, see [10])

$$\tau(y) = \frac{T(y)}{\rho U^2 L} = 1.3\sqrt{Re}(1 - \frac{y}{L})$$

Since the filament is assumed to be infinite, we will use the maximum value to be representative, $\tau(y=0) = 1.3Re^{-1/2}$.

Substitution of the generic solution into equation (6.1.8) yields a quadratic expression

$$\omega = \frac{\rho_a k \mp k\sqrt{(\rho + \rho_a)(1.3Re^{-1/2} + \gamma k^2) - \rho\rho_a}}{\rho + \rho_a}$$

In this case the stability of the solution is found when $Im(\omega) = 0$. This can be asserted by the evaluation of the term under the square root. In particular the stability condition can be written

$$(\rho + \frac{2}{k})(1.3Re^{-1/2} + \gamma k^2) - \frac{2\rho}{k} \geq 0,$$

from which it is possible to derive critical values for linear density, flexural stiffness and incoming velocity related to other parameters. In the previous equation we substituted $\rho_a = 2/k$ given from potential flow solution [74] ($k = 2\pi$).

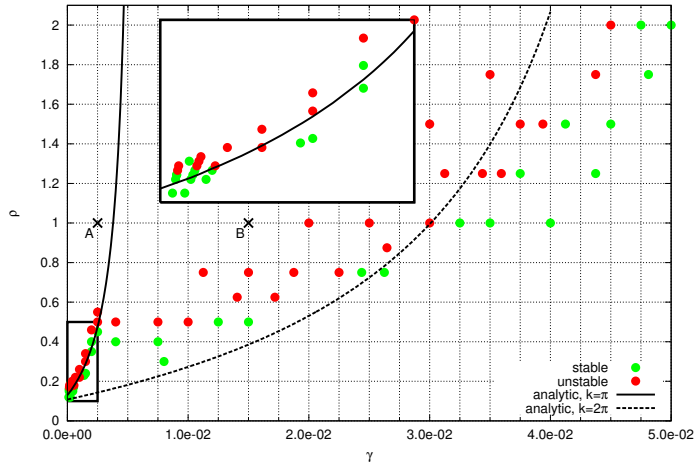

Figure 6.1.2: Comparison between analytical models and DNS simulations. The close-up refers to the rectangle near axis origin.

Numerical simulations show a good agreement with the theoretical curve up to $\gamma = 2.5 \cdot 10^{-3}$ (Figure 6.1.2), which coincides with the range of values investigated by Connel and Yue [71]. Above this critical value of the bending stiffness the agreement between the analytical model and DNS simulations deteriorates. This discrepancy can be partly explained by a modification of the filament shape as the value of γ exceeds $2.5 \cdot 10^{-3}$. In relation to Figure 6.1.2, Figure 6.1.3 depicts snapshots of the filament during a flapping cycle for two different values of γ (cases A and B, respectively), whereas in Figure 2.2.1 vorticity iso-contours for the same parameter sets are shown. Here, it can be noted that the wave number $k = 2\pi$ for $\gamma < 2.5 \cdot 10^{-3}$, while k is approximately π when $\gamma > 2.5 \cdot 10^{-3}$. Following the derivation of the model, this shape alteration leads to a variation of the added mass coefficient obtained from potential theory. The new curve drawn for $k = \pi$ matches qualitatively the DNS simulations (Figure 6.1.2). Further discrepancy between analytics and numerics may be due to the failure of the model (still based on Blasius boundary layer theory) to predict, for example, tension along filament.

In Section 6.1.9 we show a generalization of the well-established model to also account for permeability. Interestingly, the simple generalization qualitatively

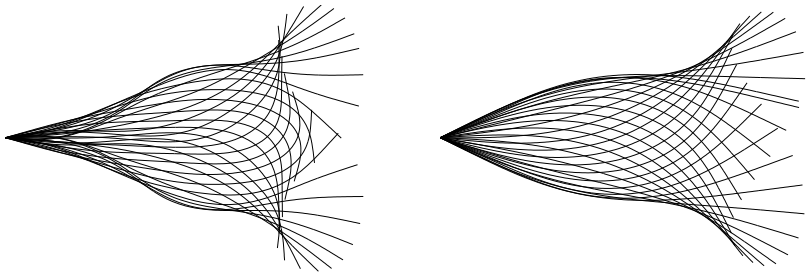

Figure 6.1.3: Snapshots of impermeable filament during one flapping cycle for case A (left) and B (right) depicted on Figure 6.1.2. While a unique concavity characterizes the behavior of the right filament, an inflection point is clearly identifiable in the left oscillations.

captures the stability effect induced by permeability. However, a quantitative comparison between our DNS results and model prediction is not satisfactory. A possible reason is that we exclude any dependency of tension τ and added mass ρ_a on the permeability and wave number. The latter is expected to depend greatly on permeability in an analogy to what is observed in a suction/blowing boundary layer.

6.1.7 Simulations of permeable filament

In order to assess the stabilizing property of permeability, several DNS simulations with different sets of parameters (γ, ρ) have been performed at $Re = 200$ and for different values of permeability λ. For the impermeable case ($\lambda = 0$) we compare the DNS results with the analytical curve obtaining a close agreement, which can be seen in Figure 6.1.4. When permeability is considered ($\lambda \neq 0$), the critical density difference ρ increases as λ increases, for a given value of bending stiffness γ. This means that the onset of instability requires a heavier filament as the permeability increases. If we consider the (ρ, γ) plane, for instance, the neutral curve shifts up when going from an impermeable to an increasingly more permeable filament (Figure 6.1.4), effectively extending the stability zone.

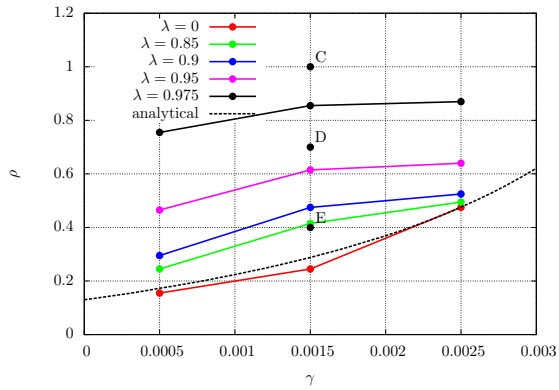

Figure 6.1.4: Neutral curve on the plane (γ, ρ) for $Re = 200$ and $\lambda = 0$. The analytical curve for $\lambda = 0$ is taken from [71], whereas dotted lines represent neutral curves for different permeabilities.

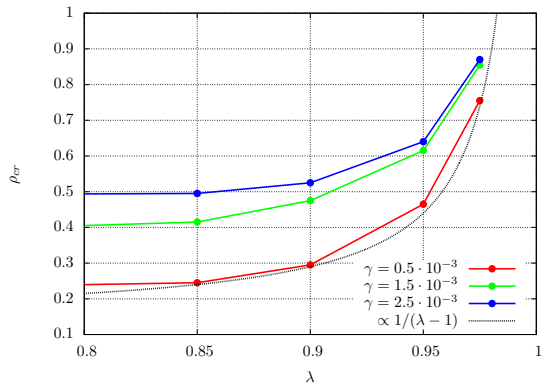

Figure 6.1.5: Critical value of ρ with λ for different values of bending stiffness γ.

Even considering parameter values far from the stability threshold (bullets C, D and E in Figure 6.1.4), permeability still shows a non-negligible effect on the dynamics of the filament: as permeability is increased both the sustained flapping amplitude and frequency (Figure 6.1.6) decrease.

Besides kinematics (Figure 6.1.6), the effects of permeability on the peak

values of the forces acting on the flapping filament have also been assessed for case C shown in Figure 6.1.4. Both lift and drag forces decrease monotonically as permeability increases (Figure 6.1.7, left). As we can see, there is an optimal value of $\lambda \simeq 0.6$ for which the aerodynamic efficiency is maximized.

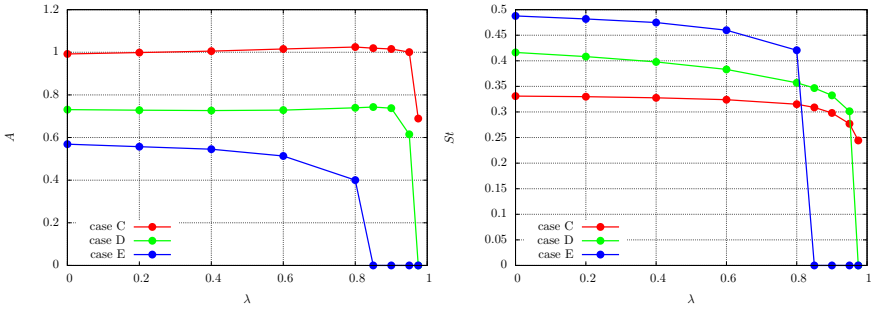

Figure 6.1.6: Oscillation amplitude and frequency as function of permeability. Each curve is drawn for different sets of parameters (γ, ρ), see Figure 6.1.4.

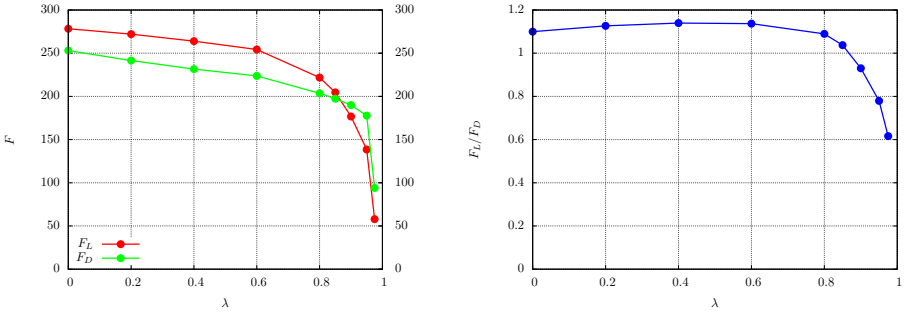

Figure 6.1.7: Lift and drag forces (left) aerodynamic efficiency (right) for case C (Figure 6.1.4), all as a function of the permeability.

In previous sections we showed quantitative results on the permeability stabilizing role on the flapping behavior of an elastic filament. In this section we will provide a simple physical mechanism at the origin of the stabilization and show that the phenomenon can be traced back to a resonance condition between porous and hydrodynamical time scales.

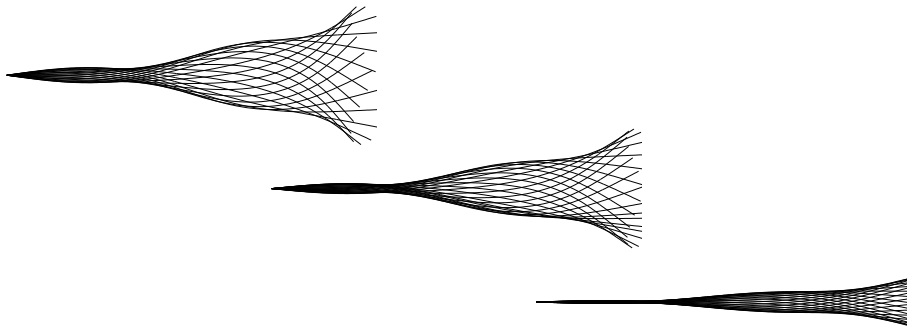

Figure 6.1.8: Snapshots of permeable filaments (respectively $\lambda = 0, 0.6, 0.8$) during one flapping cycle (case C, Figure 6.1.4 and 6.1.6).

6.1.8 The permeability time-scale

The idea is that two different mechanisms at work start to interact when their characteristic time-scales become of the same order of magnitude. Arguments of this type have been successful, e.g. to explain a symmetry breaking mechanism in fluid-structure interaction [70] as well as emergence of elastic instabilities [75, 63] and the emergence of macroscopic spatial scales at which microscopic polymers cause visco-elastic behavior [80]. In this spirit we define the *permeable time* as the characteristic time needed by mass to cross the membrane of thickness δ. Following Darcy's empirical law $\mathbf{U} - \mathbf{U}_{ib} = -k\nabla p$, we estimate this quantity to be:

$$\tau_{por} = \frac{\delta}{\|\mathbf{U} - \mathbf{U}_{ib}\|} = \frac{\delta}{k\nabla p} = \frac{\delta^2}{k\Delta p} \tag{6.1.9}$$

In order to give a quantitative value for the pressure difference across the membrane, we resort to the slender body theory [73] already used in [71, 74]

$$\Delta p = \rho_a \left(\frac{\partial}{\partial t} + U\frac{\partial}{\partial s}\right)^2 h \simeq \rho_a \left(\frac{U}{L}\right)^2 h \tag{6.1.10}$$

where ρ_a is the added mass coefficient as defined in Section 6.1.6, $(\partial/\partial t + U\partial/\partial t)$ is the convective derivative for a fluid particle near the filament and h is the vertical displacement. Inserting (5.5.6) and (6.1.10) into (6.1.9) one obtains

$$\tau_{por} = -\frac{\delta L^2 \beta(1-\lambda)}{\rho_a U^2 h}$$

Physically, this is the time it takes for the flow to flatten the pressure difference Δp across the filament.

Our aim here is to compare this characteristic time-scale with the hydrodynamical time-scale, roughly estimated as $\tau_{hdr} = L/U$, in order to assess λ critical value to have resonance between permeability and hydrodynamics:

$$\frac{\tau_{por}}{\tau_{hdr}} = -\frac{\delta L^2 \beta (1-\lambda)}{\rho_a U^2 h}\frac{U}{L} = -\frac{\delta L \beta (1-\lambda)}{\rho_a U h} \simeq 1.$$

From this expression we can derive a critical value of λ as

$$\lambda_{crt} \simeq 1 + \frac{\rho_a U h}{\delta L \beta}. \tag{6.1.11}$$

If we use the parameters given here the critical value of λ is $\simeq 0.98$, in qualitative agreement with DNS. Such a value corresponds to a permeability $k \simeq 0.06$ (see Eq. (5.5.6)). Interestingly, this result shows that the permeability stabilizing effect occurs when we are very close to $\lambda = 1$ (see Figure 6.1.6).

6.1.9 Straightforward generalization of the analytical model

Let us perform a stability analysis study on a simplified model inspired from [71]. Permeability has the overall effect of reducing the drag force of fluid by allowing a mass transfer through the body. That is to say, it reduces the force exerted by the fluid on the filament normal direction by reducing the pressure difference across the boundary.

In order to take into account permeability effects we propose to reduce the hydrodynamical forces by a factor $(1-\lambda)$

$$L(s,t) = -\rho_a (1-\lambda)(\frac{\partial}{\partial t} + U\frac{\partial}{\partial s})^2 h$$

from which, by using the same non-dimensionalization as in Section 6.1.6, we obtain

$$[\mu + (1-\alpha)\mu_a]\frac{\partial^2 h}{\partial t^2} + 2\mu_a(1-\alpha)\frac{\partial}{\partial s}\frac{\partial h}{\partial t} + [\mu_a(1-\alpha) - \tau]\frac{\partial^2 h}{\partial s^2} + \gamma\frac{\partial^4 h}{\partial s^4} = 0$$

where λ represents permeability ($\lambda = 0$ reduces to the impermeable case, $\lambda = 1$ is the limit for an infinitely permeable boundary). If we now perform a stability analysis as before, we end up with a slightly different stability condition

$$\left[\frac{2(1-\lambda)}{k} + \rho\right]\left[\gamma k^2 + \frac{1.3}{\rho\sqrt{Re}}\right] - \frac{2(1-\lambda)}{k} \geq 0 \tag{6.1.12}$$

from which it is possible to derive critical values for linear density, flexural stiffness and incoming velocity related to permeability λ and Reynolds number Re (see Figure 6.1.9).

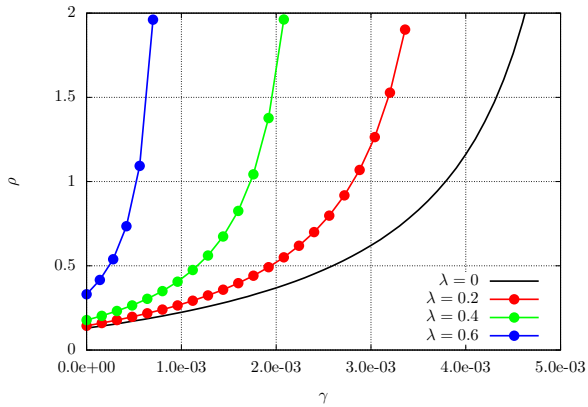

Figure 6.1.9: Neutral curves on the plane (γ, ρ) for $Re = 200$ and different values of the permeability coefficient λ.

6.1.10 Conclusions

The present work represents the initial investigation of how to take into account permeability in conjunction with mass and bending rigidity in an immersed boundary formulation through an innovative formulation. For simulations taking into account permeability, the code has been confirmed by Darcy's empirical theory in Section 5.5.6.

In order to test numerical results, the code has been benchmarked with results from classical stability analysis [71] without taking into account permeability. Results (Figure 6.1.2) show a good agreement between the theoretical prediction of the stability curve and the DNS simulations up to $\gamma = 2.5 \cdot 10^{-3}$. After this value the wave number associated with the oscillation of the filament decreases, leading to a failure of the theoretical curve.

Simulations of permeable filament (Figure 6.1.4) show that permeability increases significantly the stability zone for values of $\lambda > 0.85$. As Figure 6.1.5 shows, the critical value of the filament linear density ρ_{cr} does not vary for $\lambda < 0.85$, while above this threshold it varies as $1/(\lambda - 1)$ (Figure 6.1.5). This behavior is confirmed also by Figure 6.1.6 from which it appears that both flapping amplitude and frequency remain constant up to $\lambda \simeq 0.8$ and decrease

sharply afterward. As it comes to forces (Figure 6.1.7), both lift and drag shows a smoother dependence on permeability. It appears to be a maximum in the lift over drag ratio for $\lambda \simeq 0.6$. This particular dependence of both kinematic and dynamic quantities on permeability is also confirmed through the physical interpretation based on characteristic time scales we give in Section 6.1.8.

Moreover, in Section 6.1.9 the stability analysis developed for an impermeable flag has been extended in order to also take permeability into account. This attempt (Figure 6.1.9), matching numerical results in a qualitative way, is not able to give a good prediction of the neutral curve.

6.2 Retinal detachment

Retinal detachment is one of the common pathologies of the human eye which involves the separation of the sensory retina, a thin layer of neural tissue that lines the back of the eye, from the underlying retinal pigment epithelium [92] (Figure 6.2.1). It occurs when fluid enters the sub-retinal space through a retinal tear between the neurosensory retina and the retinal pigment epithelium, the outer layer to which the retina adheres.

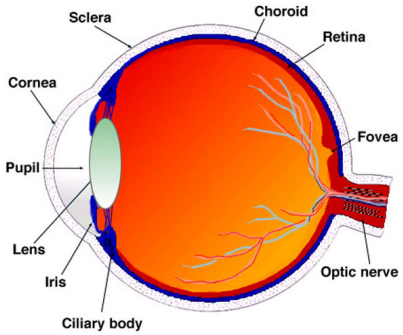

Figure 6.2.1: Vertical sagittal section of human eye.

There are numerous variations in the pathogenesis of a retinal detachment. They include developmental factors, such as myopia, that affect the overall size and shape of the globe, vitreoretinal disorders, metabolic disease, trauma, inflammation and degenerative conditions. A retinal detachment can have devastating visual consequences depending on its displacement and extent. If the detachment reaches the macula, the most sensitive part of the eye, patient

could experience a significant reduction of vision field or, in the worst cases, lose eyesight. However, the majority of retinal breaks do not result in retinal detachment. In the general population, retinal detachment occurs in about 12 out of 100,000 people (0.01% annual risk) with a lifetime risk (up to 60 years of age) of 0.6%, and is one of the most frequent causes of blindness in Western countries [93]. Retinal detachment can be divided into rhegmatogenous and nonrhegmatogenous detachment, with the first being the most common. In the first case a vitreous traction generates a break (retinal tear) while in the second case detachment occurs without any retinal breaks (Figure 6.2.2).

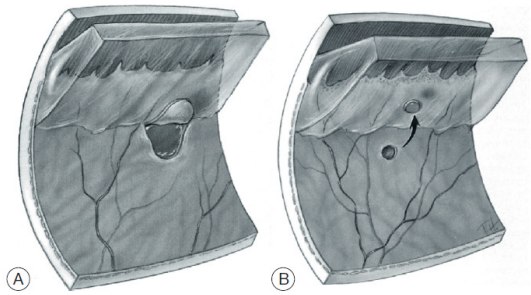

Figure 6.2.2: Irregular posterior extensions of the vitreous due to horseshoe-shaped retinal tears (A) and retinal hole with a free operculum (B).

In this application we analyze two types of rhegmatogenous detachments, called retinal tear and retinal hole. The first type occurs when a localized traction generates a break in the retinal layer, leading to the formation of a retinal flap which is free to move (Figure 6.2.2). The second type is characterized by the presence of a hole in the retinal layer, which is typically produced by localized vitroretinal traction able to remove a certain area of the retina. As the typical size of the flap is much smaller than the eye radius, in the numerical simulations we model the eye surface as a flat plate. We further simplify the model by restricting our attention to two dimensional simulations so that the "tear" case will be represented by a single filament, analogous to the one used in Section 6.1. In the simulations regarding the hole, we chose to model the three-dimensional geometrical effect with a tip-connecting spring between the two-filaments. Our final aim is to assess the forces and torques generated at the attachment points of both the "tear" and the "hole" in order to determine which type of detachment could deteriorate more easily.

6.2.1 Imposed plate motion

In order to simulate the dynamics of retinal detachment we first need to consider the characteristics of eye movements, which are the main forcing mechanisms producing flow in the vitreous chamber.

In this work we focus on the so-called saccadic motion that, due to its characteristics, is the main responsible of vitreous motion. A saccade is a fast movement of the eye, by which the eye scans the surroundings and acquires information. Physiologic characteristics of eye movements are reported in detail in Becker [88], where the basic features of these movements are discussed. In particular, saccadic rotations are characterized by:

- high initial angular acceleration (up to $30000^\circ s^2$);
- a less intense deceleration which is, however, capable of inducing a very efficient stop of the movement;
- a peak angular velocity proportional to the saccadic amplitude for small rotations up to a saturation value ranging between 400 and 600 deg s^{-2} for larger movements;
- an amplitude ranging from 0.05° (microsaccades) to $80-90^\circ$, which is the physical upper limit for eye rotations.

As referred to in [85], a saccade movement can be described through the following quantities: the saccade amplitude A, the saccade duration D, the peak angular velocity Ω_p and the acceleration time t_p, i.e. the time required to reach the peak velocity starting from rest. Becker [88] reports that the relationship between saccade duration and saccade amplitude is very well described by the following linear law:

$$D = D_0 + dA$$

in the range $5^\circ < A < 50^\circ$, where d approximately assumes the value of $0.0025s\ deg^{-1}$ and the intercept D_0 typically ranges between 0.02 and $0.03s$. D is measured in seconds and A in degrees. The average angular velocity during a saccadic movement is defined as $\bar{\Omega} = A/D$ and measurements suggest that the ratio $\Omega_p/\bar{\Omega}$ between the peak and the mean velocities attains a fairly constant value. Becker [88] suggests the constant value of 1.64. Finally, the experimental data show that small amplitude saccades (smaller than 10°) follow an almost symmetrical time law, the acceleration time t_p being approximately 0.45 D. The dimensionless quantity t_p/D varies linearly with increasing saccade amplitudes to the value of $t_p/D \simeq 0.25$ for saccades of 50°.

Repetto et al. [85] proposed to describe the time law $\theta(t)$ describing the angular eye displacement θ in time by making use of a simple fifth order degree polynomial function of the form

$$\theta(t) = c_0 + c_1 t + c_2 t^2 + c_3 t^3 + c_4 t^4 + c_5 t^5$$

where the coefficients c_i are computed by imposing the following constraints: $\theta(0) = 0$, $\theta(D) = A$, $\dot{\theta}(0) = 0$, $\dot{\theta}(D) = 0$, $\dot{\theta}(t_p) = \Omega_p$ and $\ddot{\theta}(t_p) = 0$ where D, Ω_p and t_p are evaluated by using the previous relationships. The resulting functions $\theta(t)$ and $d\theta/dt$ are shown in Figure 6.2.3 in terms of position $r\ \theta$ and velocity $r\ d\theta/dt$ (where r is the eye radius) and they satisfactorily reproduce the main features of real saccadic movements.

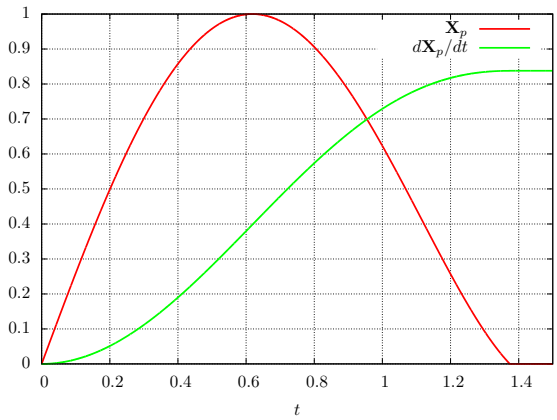

Figure 6.2.3: Plate position $\mathbf{X}_p = r\theta$ (red) and velocity $d\mathbf{X}_p/dt = r\ d\theta/dt$ (green) as function of time (Figure 6.2.4).

Besides the "tear" and the "hole" configuration we also performed additional simulations addressed as "periodic tear" similar to the "tear" case but in which the motion of the wall is assumed periodic in time:

$$\mathbf{X}_p(t) = r\theta(t) = \bar{a}\sin(2\pi\bar{f})$$

6.2.2 Numerical discretization

In the following we describe both the set-up and results from simulations regarding the "tear" and "hole" configurations. For problem formulation and characteristic length scales the reader may refer to Section 6.1.1. In all simulations

the Reynolds number has been set constant and equal to 114.6 and the effect of gravity has been neglected. In the case of the "tear" and the "hole" we consider the filaments to have different non-dimensional lengths ($L^* = 0.75, 1, 1.25$) and the same non-dimensional bending stiffness ($1 \cdot 10^{-1}$), while in the case of "periodic tear" the same length but different non-dimensional bending stiffness ($K_b^* = 1 \cdot 10^{-1}, 2.5 \cdot 10^{-1}, 5 \cdot 10^{-1}$) and non-dimensional frequency has been considered. In all the simulations the fluid kinematic viscosity ν has been calculated to give $Re = 114.6$.

We let $\mathbf{x} = (x, y) \in \Omega$ be the Cartesian physical coordinates, with Ω denoting the physical domain; let $s \in \Gamma$ be the Lagrangian curvilinear coordinate, with Γ denoting the body surface; let $\mathbf{X}(s,t) = (X_1(s,t), X_2(s,t)) \in \Gamma$ denote the physical position of each material point of curvilinear coordinate s at time t. Given these assumptions, the governing equations are the same as described in Section 6.1.2.

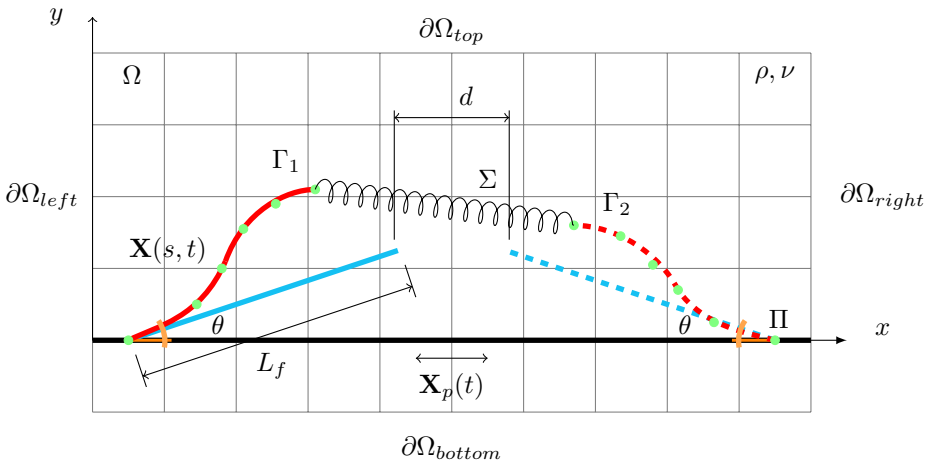

Figure 6.2.4: Filament Γ_1 (in red, initial condition in cyan) is clamped to an underlying plate Π at a certain angle θ and is described by a set of Lagrangian points $\mathbf{X}(s,t)$ (in green). Plate Π is animated with a prescribed motion $\mathbf{X}_p(t)$. In the "hole" case filament Γ_2 is also considered, bounded by spring Σ to Γ_1 with initial distance d.

The incompressible Naviers-Stokes equations of motion (6.1.1) are considered together with an artificial forcing $\mathbf{f}$ to enforce the no-slip condition on the filaments. Hydrodynamical forces acting on the filaments are calculated by means of eq. (6.1.2), known as the Goldstein feedback law. Filament dynamics is considered in equations (6.1.6) and (4.3.8).

Since the filament is clamped to a moving plate with a given angle θ (see Figure 6.2.4), equation (6.1.6) needs to be solved along with proper boundary conditions both at the clamped and at the free edge:

$$\mathbf{X}|_{s=0} = \mathbf{X}_p(t), \quad \left.\frac{\partial \mathbf{X}}{\partial s}\right|_{s=0} = (\cos\theta, \sin\theta)\,, \quad \left.\frac{\partial^2 \mathbf{X}}{\partial^2 s}\right|_{s=L} = 0, \quad \left.\frac{\partial^3 \mathbf{X}}{\partial^3 s}\right|_{s=L} = 0.$$

The first and second conditions enforce the filament to follow the underlying moving plate and to be clamped with a given angle θ, while the third condition state that the bending moment and shear at the free edge is zero. The latter condition is true in both the "tear" and "hole" case. The two cases are different in that for the "tear" case no further forces other than the hydrodynamical ones are applied at the free edge, while in the hole case the free edges are subject to an additional force $\pm k_\Sigma(\mathbf{X}_1|_{s=L} - \mathbf{X}_2|_{s=L})$ (depending on the filament) modeling the tip-connecting spring. On the other hand, equation (6.1.7) is solved together with the conditions:

$$\frac{\partial}{\partial s}\left(T\frac{\partial \mathbf{X}}{\partial s}\right)_{s=0} = \mathbf{F} + \mathbf{F_b} + A_P, \quad T|_{s=L} = 0,$$

where A_p is the plate acceleration. The first one derives from equation (6.1.6) while the second comes again from the unloaded free edge condition. This condition is maintained also in the "hole" case in the absence of a better estimate of the spring tension. The main observables of this work are the forces and moments at the clamped edge of the filaments, defined as:

$$\mathbf{F}_c = (T\boldsymbol{\tau} + S\mathbf{n})_{s=0}\,, \quad M_c = (\kappa\gamma)_{s=0} \tag{6.2.1}$$

where $\boldsymbol{\tau}$ and $\mathbf{n}$ are the local normal and tangential unit vectors while κ is the curvature of the filament at the clamped edge (see Section 2.3). In this way, the computed force $\mathbf{F}_c$ and torque M_c are those exerted by the filament on the plate.

The computational domain is an $5 \cdot 2.5$ rectangle ranging $[-1, 4]$ in the direction parallel to the plate and $[0, 2.5]$ in the normal direction in the "tear" case. For the "hole" the domain is slightly bigger ranging from -2 to 4. Velocity boundary conditions (Figure 6.2.4) are: periodic between Ω_{right} and Ω_{left} and $\{\mathbf{u}\cdot\mathbf{n} = 0,\ \partial(\mathbf{u}\cdot\boldsymbol{\tau})/\partial\mathbf{n} = 0\}$ at Ω_{top} and Ω_{bottom} (symmetrical boundary condition), where $\mathbf{n}$ and $\boldsymbol{\tau}$ are respectively the normal and tangential directions to the boundary. As the plate is modeled as an immersed boundary, all of its points have to be inside the domain in the y direction ($[0.2 - 3/80, 0.2]$), while it spans all the domain in the x direction because of the periodic boundary conditions from left to right. Along the plate the computational grid is uniform

with grid spacing 1/60, while in the normal direction it is uniform in the region $[0, 1.5]$ with grid spacing 1/40 and stretched outside with a constant stretching ratio equal to 1.1.

Furthermore, the dimensionless quantity $\rho = \rho_1^*/(\rho_F^* L^*)$ defined in Section 6.1 has been set $= 1 \cdot 10^{-2}$, from which

$$\frac{\rho_S^* - \rho_F^* A^*}{\rho_F^* A^*} = \rho \frac{L^*}{A^*} = 0.3$$

as the filament cross-section A^* has been estimated (as in Section 5.5.6) to be equal to the support of the Dirac Delta function support, i.e. $2\Delta x$, thus giving $L^*/A^* = 30$. This means that the simulated filament is 30% heavier than the surrounding fluid.

The filament length L is set equal to 1 and the Lagrangian grid is made up of 120 points, so that approximately 2 Lagrangian points appear in one Eulerian cell. Velocity boundary conditions are the no-slip boundary condition at the plate (whose motion has been taken from [85]), periodic conditions at the sides and slip boundary conditions at the top (see Figure 6.2.4). Since the computational grid for the flow is staggered, no boundary conditions for the pressure are needed. The initial configuration of the filament is a straight line clamped at a certain angle θ with respect to the plate. In the case of the hole a second filament symmetrical to the first one is considered, tethered to this one by a spring Σ with stiffness k_Σ (Figure 6.2.4). The numerical scheme and solution procedure are the same as those described in Sections 6.1.4 and 6.1.5.

6.2.3 Tear case

In these simulations we investigate the behavior of a single clamped filament ("tear", see Figure 6.2.2, A), and evaluate the forces and moment transmitted to the plate. In all graphs time is scaled with D, the saccade duration, so that the temporal interval of motion is given for $(0 \leq t/D \leq 1)$. Snapshots of the dynamics of the single filament are shown in Figure 6.2.5. Between time 0 and $t/D \simeq 0.5$ the plate accelerates from the initial configuration causing the stationary fluid to impact on the filament. This gives raise to a buckling effect on the filament, which bends. When the plate stops at $t/D = 1$ both the stored bending energy and the inertia of the fluid make the filament continue its motion until, after some oscillations, it goes back to its resting straight position.

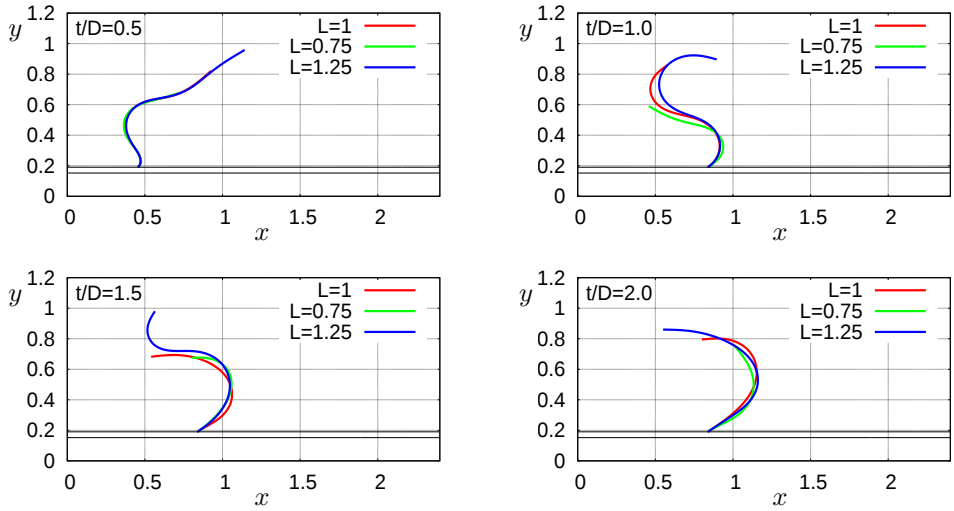

Figure 6.2.5: Dynamics of the single clamped filament during the plate motion at different times.

First we study the sensitivity of the dynamical response at the attachment point on the filament length. In order to investigate the trend, we simulate three different lengths L (0.75, 1 and 1.25). Figures 6.2.6-6.2.8 describe the evolution of the clamping forces $\mathbf{F}_c$ and moment M_c in time, while Figure 6.2.12 (left column) shows that both $\mathbf{F}_c$ and M_c increase in absolute value with the filament length. It can be noted (Figures 6.2.6 to 6.2.11) that both forces and moments increase from zero, reach the peak value nearly at the same time, i.e. at the velocity peak time and return to zero after the plate stops.

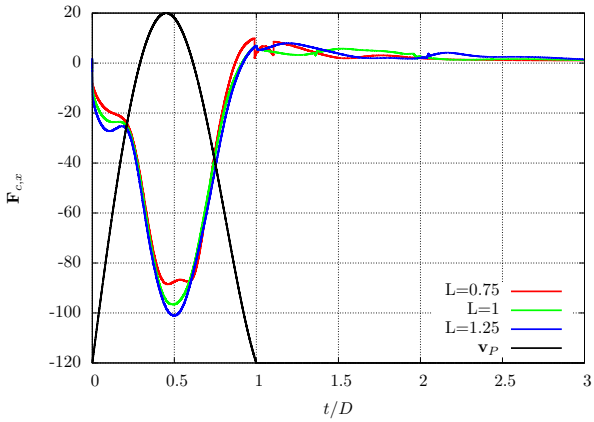

Figure 6.2.6: Time history of the x-force component acting at the attachment point of the filament for different filament lengths. The velocity of the plate is in black.

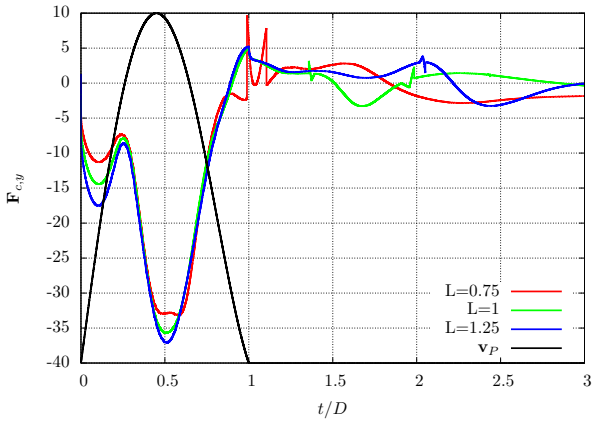

Figure 6.2.7: Time history of the y-force component acting at the attachment point of the filament for different filament lengths. The velocity of the plate is in black.

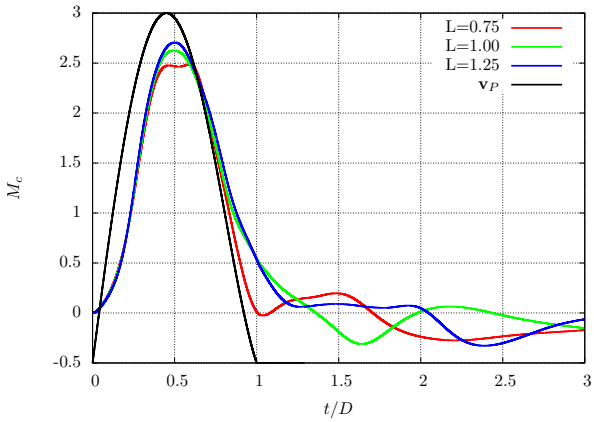

Figure 6.2.8: Time history of the moment acting at the attachment point of the filament for different filament lengths. The velocity of the plate is in black.

In order to study the influence of the clamping angle on the dynamical response of the plate we simulate three different angles (27°, 30° and 33.56°) given a fixed filament length, $L = 1$. In Figures 6.2.9-6.2.11 we show the evolution of the clamping forces $\mathbf{F}_c$ and moment M_c with time, while Figure 6.2.12 (right column) summarizes the influence of the clamping angle θ on the absolute peak values of both $\mathbf{F}_c$ and M_c: the x component of the force does not show any appreciable variation, while the y component of the force and the moment increase with the angle. As in the case of varying the filament length both forces and moments have their peak value at the time of maximum plate velocity.

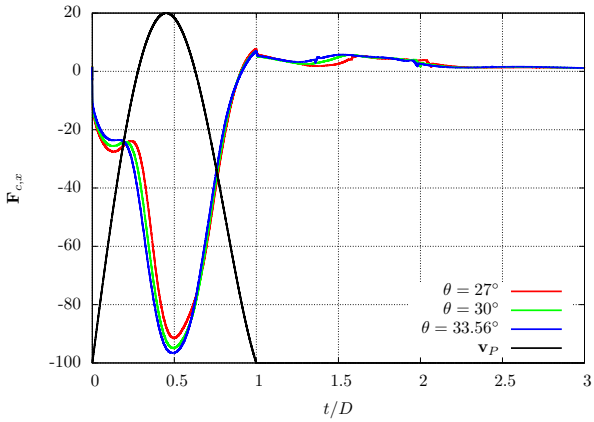

Figure 6.2.9: Time history of the x-force component acting at the attachment point of the filament for different clamping angles. The velocity of the plate is in black.

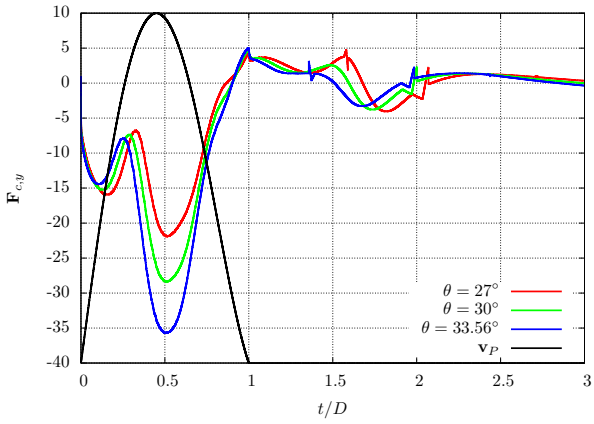

Figure 6.2.10: Time history of the y-force component acting at the attachment point of the filament for different clamping angles. The velocity of the plate is in black.

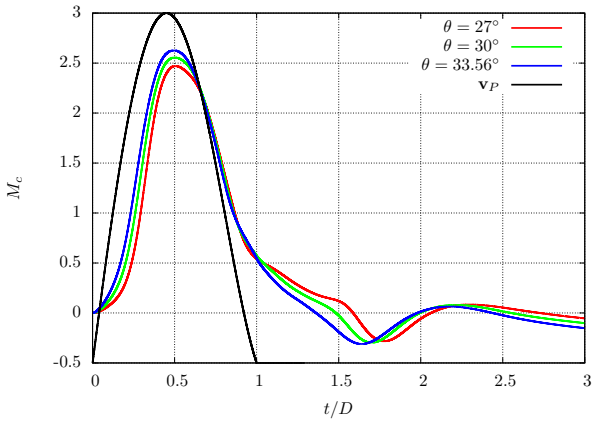

Figure 6.2.11: Time history of the moment acting at the attachment point of the filament for different clamping angles. The velocity of the plate is in black.

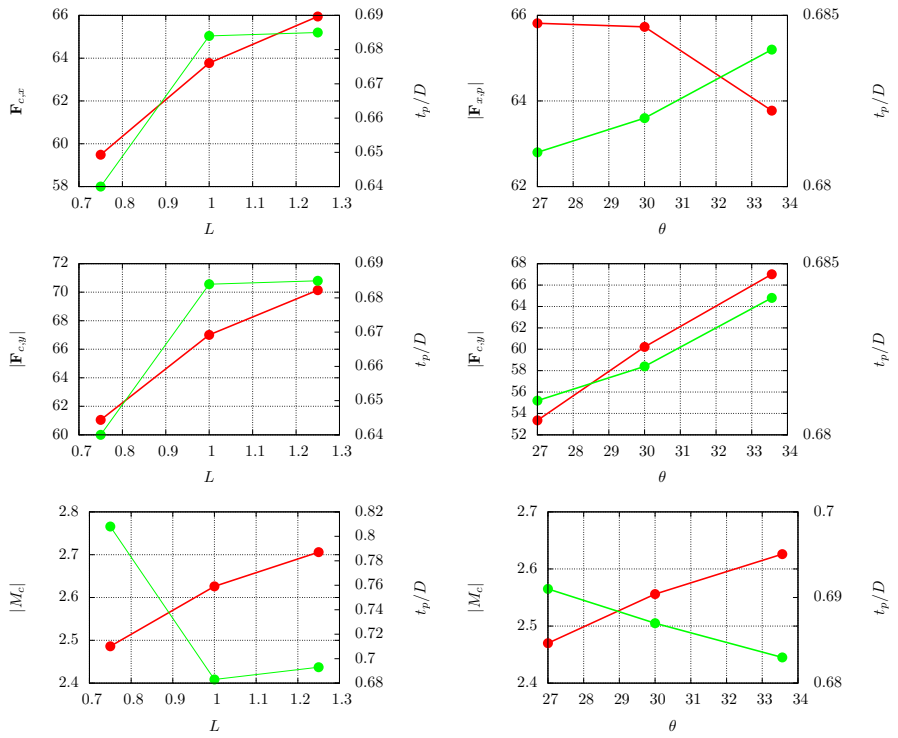

Figure 6.2.12: Peak values of force $|\mathbf{F}_c|$ and moment $|M_c|$ (in red) and corresponding time (in green) for the "tear" case. The left column shows the values for different filament length L, while in the right column the clamping angle θ varies.

6.2.4 Hole case

In this section we show results for the case of two filaments the tips of which are linked by a spring of given stiffness k_Σ ("hole", see Figure 6.2.2, B). As for the "tear" case, time is scaled with the saccade duration D, so that the plate is in motion for $(0 \leq t/D \leq 1)$. Snapshots of the dynamics of the single filament are shown in Figure 6.2.13.

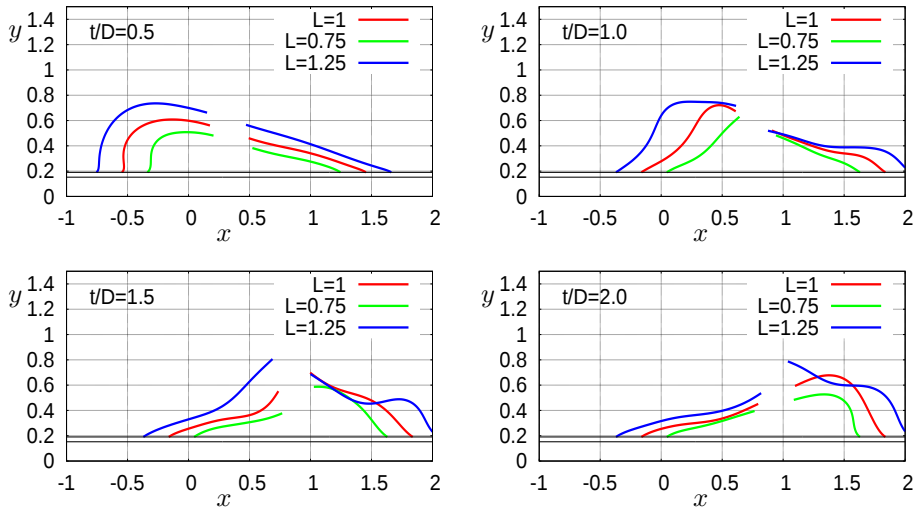

Figure 6.2.13: Dynamics of the linked clamped filaments during the plate motion at different times.

In the following we show the time history of the forces and moments transmitted by both filaments (continuous line for the right filament, dots for the left filament) to the plate. Similarly to the "tear" case, in all simulations both forces and moments follows the evolution of the plate velocity, reaching their peak approximately at the same time and then decaying to zero when the plate comes to rest. During the plate acceleration (Figure 6.2.13, $t/D = 0.5$) the pressure inside the hole rises, causing both filaments to stretch. Depending on the clamping angle, the tension T causes the x-component of the force $\mathbf{F}_c$ (Equation (6.2.1)) on the plate to be negative for the right filament and positive for the left filament, while the y-component and the moment is positive for both filaments (Figures 6.2.14-6.2.16). In all simulations the attachment point at the base of the right filament turns out to transmit the highest clamping force $\mathbf{F}_c$ to the plate, while the left one produces the highest clamping torque M_c.

Similar to the "tear" case, we study the sensitivity of the dynamical response at the attachment point on the filaments length. In order to investigate the trend, we simulate three different lengths L (0.75, 1 and 1.25, Figures 6.2.14 - 6.2.16). As the filament length increases (Figures 6.2.20 and 6.2.21, left column) the peak value of the force components shows a maximum for length $L = 1$, while the moment increases monotonically. Furthermore, differently from the "tear" case, here the peak time of forces and moment grows with the filament length.

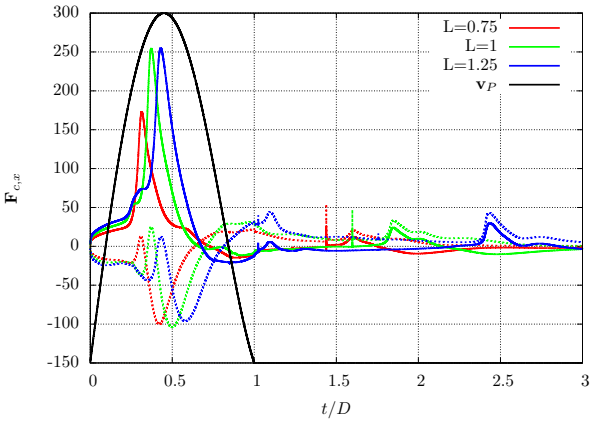

Figure 6.2.14: Time history of the x-force component acting at the attachment point of the right (line) and left (dots) filament for different filament lengths. The velocity of the plate is in black.

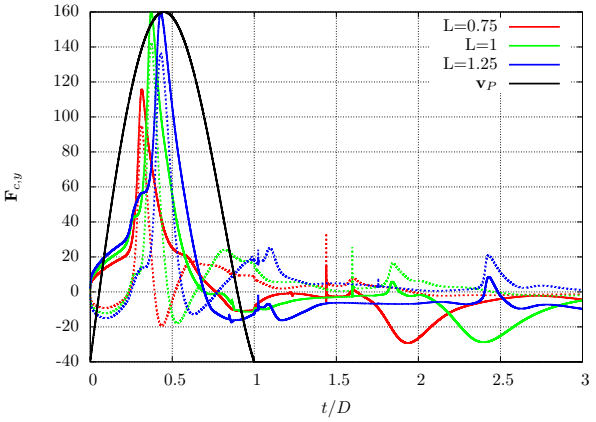

Figure 6.2.15: Time history of the y-force component acting at the attachment point of the right (line) and left (dots) filament for different filament lengths. The velocity of the plate is in black.

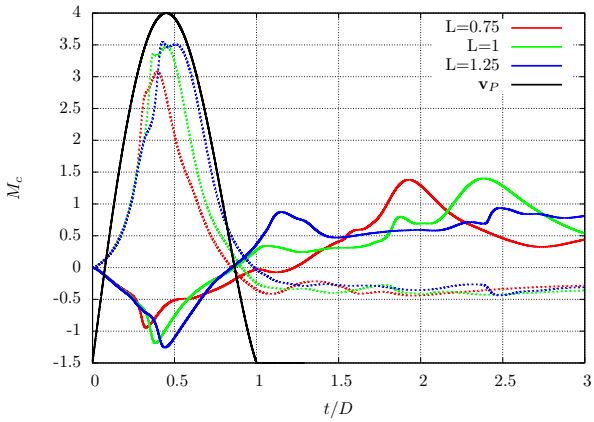

Figure 6.2.16: Time history of the moment acting at the attachment point of the right (line) and left (dots) filament for different filament lengths. The velocity of the plate is in black.

Analogously in Figures 6.2.17-6.2.19 we show the evolution of the clamping forces and moments as we change the inter-tip distance. From the results (Figures 6.2.20 and 6.2.21, right column) we notice that this parameter has little or no effect on the dynamical response at the attachment point (neither as peak value nor as peak time).

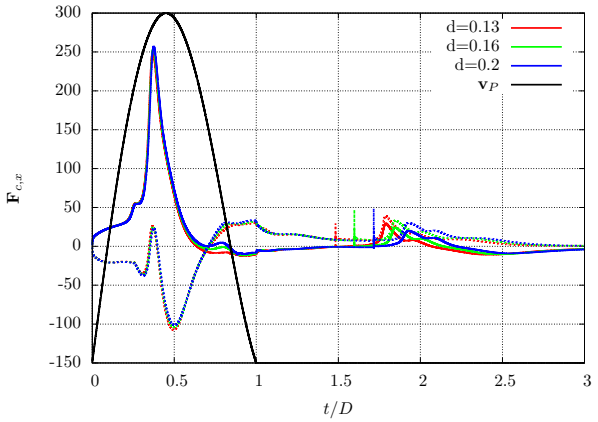

Figure 6.2.17: Time history of the x-force component acting at the attachment point of the right (line) and left (dots) filament for different inter-tip distances. The velocity of the plate is in black.

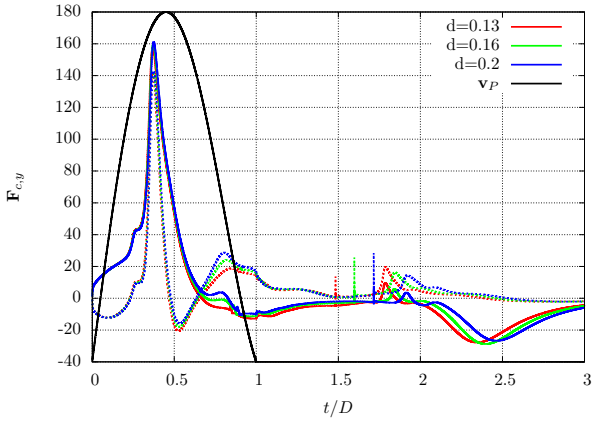

Figure 6.2.18: Time history of the y-force component acting at the attachment point of the right (line) and left (dots) filament for different inter-tip distances. The velocity of the plate is in black.

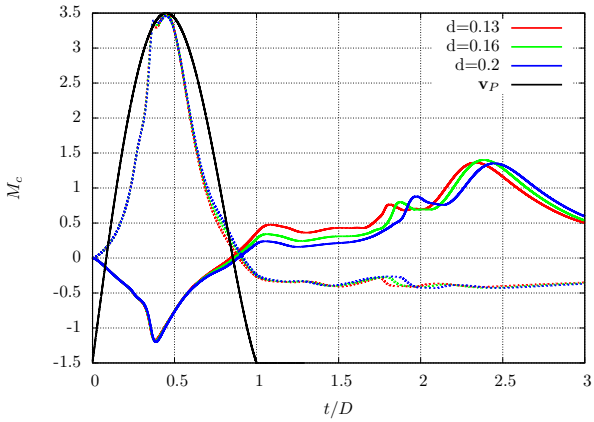

Figure 6.2.19: Time history of the moment acting at the attachment point of the right (line) and left (dots) filament for different inter-tip distances. The velocity of the plate is in black.

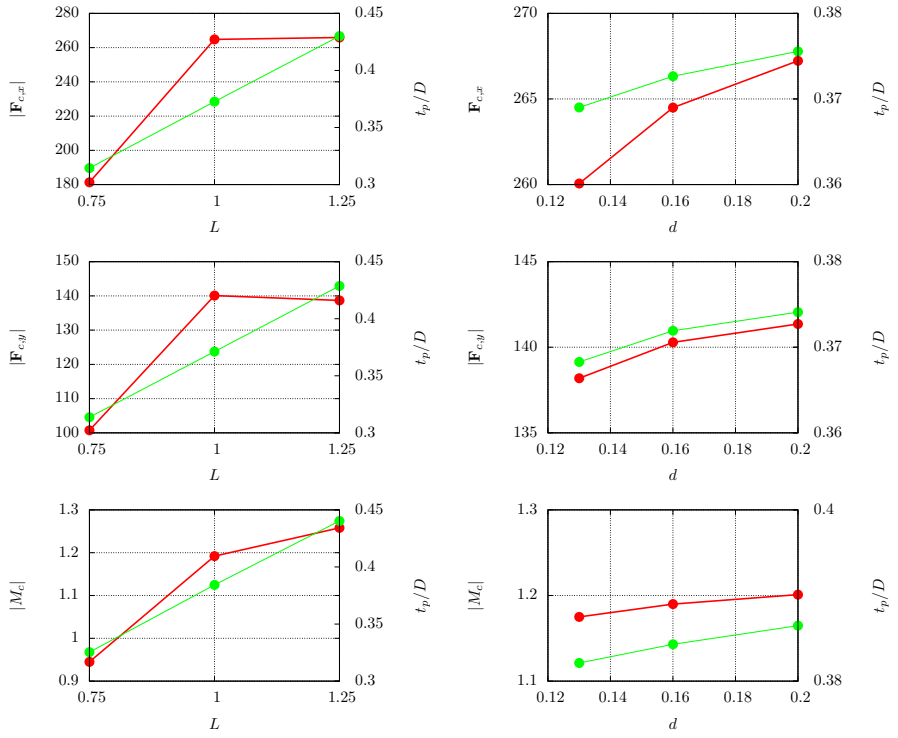

Figure 6.2.20: Peak values of force $|\mathbf{F}_c|$ and moment $|M_c|$ (in red) and corresponding time (in green) for the right filament in the "hole" case. The left column shows the values for different filament length L, while in the right column the inter-tip distance d varies.

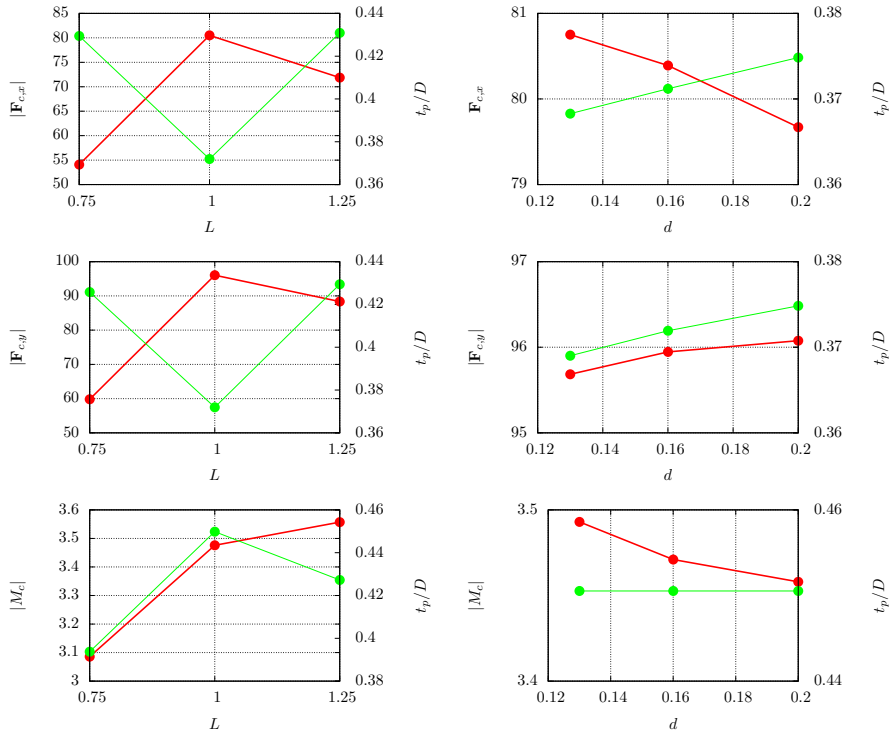

Figure 6.2.21: Peak values (in red) of force component $|\mathbf{F}_{c,x}|$ (first row), $|\mathbf{F}_{c,y}|$ (second row), and moment $|M_c|$ and corresponding time (in green) for the left filament in the "hole" case. The left column shows the values for different filament length L, while in the right column the inter-tip distance d varies.

6.2.5 Periodic tear case

In the following images we show the results from the simulations involving the same clamped filament as in the "tear" case but assuming periodic motion of the plate

$$\mathbf{X}_p(t) = r\theta(t) = \bar{a}\sin(2\pi\bar{f}).$$

In this analysis, we investigate how the filament bending stiffness ($\gamma = 1 \cdot 10^{-2}, 2.5 \cdot 10^{-2}, 5 \cdot 10^{-2}$) and the plate oscillation frequency ($f = \bar{f}, 0.5\bar{f}, 0.25\bar{f}$) effect the force and moment at the attachment point and the filament tip displacement. Both the amplitude $\bar{a}$ and the dimensionless frequency $\bar{f} \simeq 2.507$ (scaled with L/U) has been chosen so that the maximum acceleration is the

same as in the "tear" and "hole" cases. Snapshots of the filament dynamics clamped to a plate with oscillation frequency equal to $\bar{f}$ are shown in Figure 6.2.22.

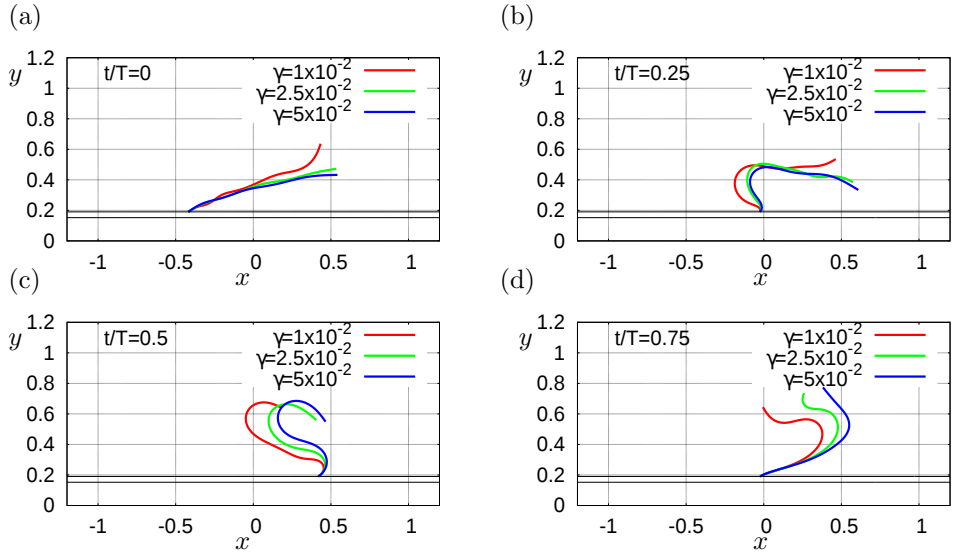

Figure 6.2.22: Dynamics of the single clamped filament during the oscillating plate motion at different times. The trajectory of the filament tip is shown in Figure 6.2.23.

In Figure 6.2.23 we show the filament tip trajectory for different values of the bending stiffness γ. The double-lobed shape of the curves comes from the plate motion. Points labeled with "0" correspond to the instant where the plate is at the leftmost location (considered here to be the beginning of the periodic cycle), at "0.25" it reaches the maximum positive velocity, at "0.5" is at the rightmost location and at the "0.75" has the maximum negative velocity. During each time-loop, the filament shows a non-symmetric behavior due to the clamping angle being different from π. In particular at the beginning of the loop (Figure 6.2.22, (a)) the filament is nearly completely extended and the plate is still. As the plate accelerates rightward a buckling instability appears in the structure, leading to the formation of a traveling wave at the root of the filament (Figure 6.2.22, (b)). As the plate motion continues rightward the traveling wave causes the filament tip to move leftward (Figure 6.2.22, (c)). Once the traveling wave reaches the filament free end it generates the so-called "bullwhip effect" [111] (Figure 6.2.22, (c)), causing the tip velocity direction to change abruptly. As the bending stiffness increases the left lobe in Figure 6.2.23 shrinks, showing

that the "bullwhip effect" becomes sharper as the bending stiffness increases.

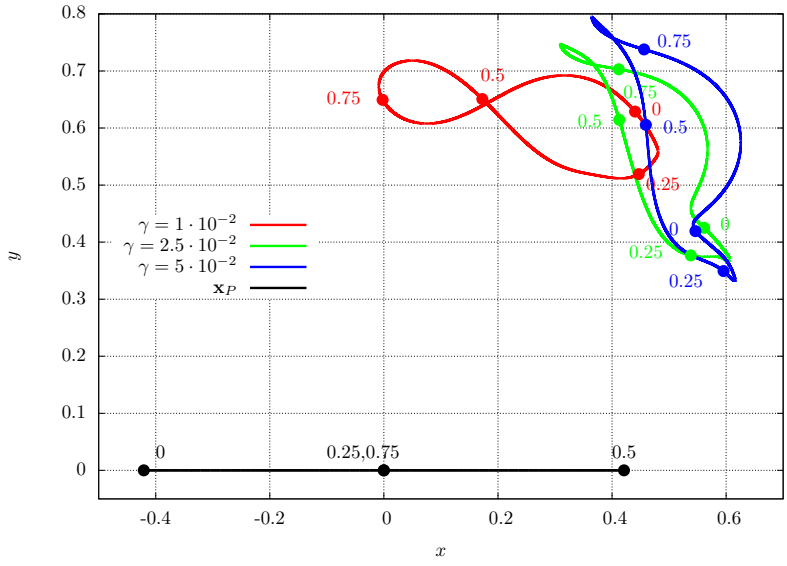

Figure 6.2.23: Trajectory of the filament tip for different bending stiffness and of the plate (black). The colored dots indicate the simulation time (as indicated in Figure 6.2.22 and 6.2.24-6.2.26).

In the following graphics the time history of the force and torque at the attachment point will be shown for different plate oscillation frequency f and bending stiffness γ. In all graphs time is scaled with the period associated to the corresponding frequency $T = 2\pi/f$.

Figures 6.2.24-6.2.26 describe the time-history of the force and moment at the attachment point for frequency $\bar{f}$ and different filament bending stiffness. Here the "bullwhip effect" is visible in the wiggles generated during the negative velocity peak, while the buckling is responsible for the local peak just after the midpoint of the cycle.

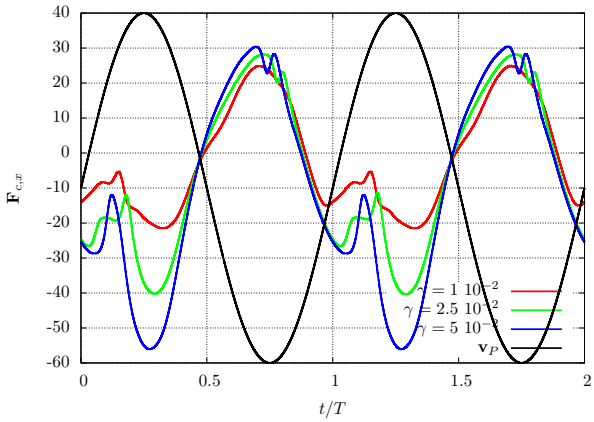

Figure 6.2.24: Time history of the x-force component acting at the attachment point of the filament for different bending stiffness and plate oscillation frequency $\bar{f}$. The velocity of the plate is in black.

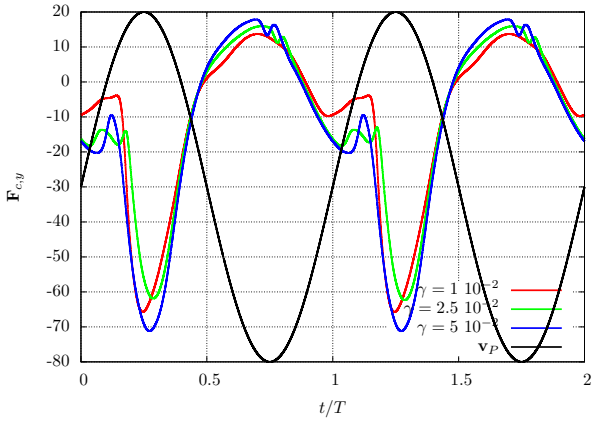

Figure 6.2.25: Time history of the y-force component acting at the attachment point of the filament for different bending stiffness and plate oscillation frequency $\bar{f}$. The velocity of the plate is in black.

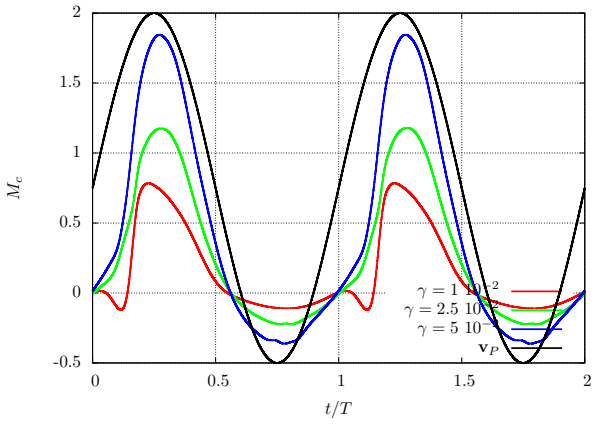

Figure 6.2.26: Time history of the moment acting at the attachment point of the filament for different bending stiffness and plate oscillation frequency $\bar{f}$. The velocity of the plate is in black.

Figures 6.2.27-6.2.29 describe the time-history of the force and moment at the attachment point for frequency $0.5\bar{f}$ and different filament bending stiffness.

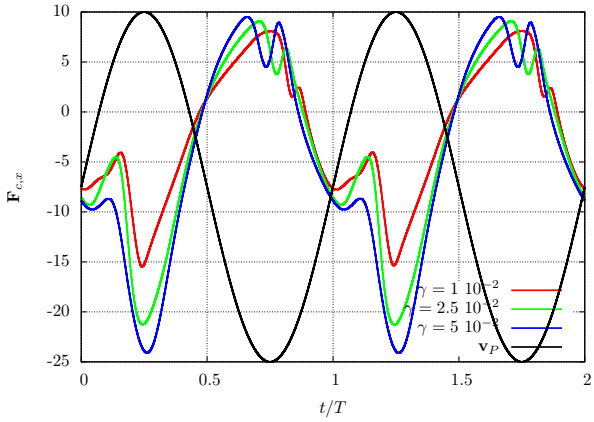

Figure 6.2.27: Time history of the x-force component acting at the attachment point of the filament for different bending stiffness and plate oscillation frequency $0.5\bar{f}$. The velocity of the plate is in black.

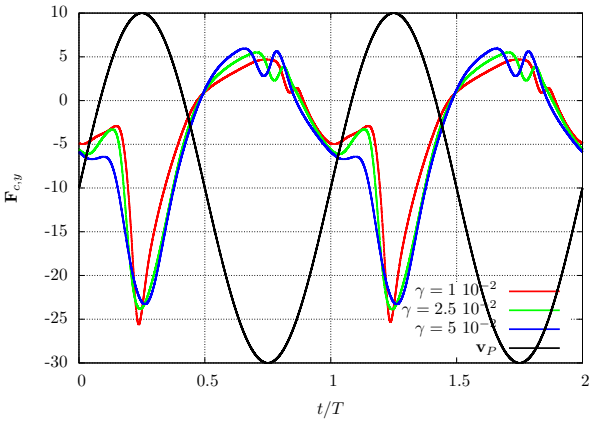

Figure 6.2.28: Time history of the y-force component acting at the attachment point of the filament for different bending stiffness and plate oscillation frequency $0.5\bar{f}$. The velocity of the plate is in black.

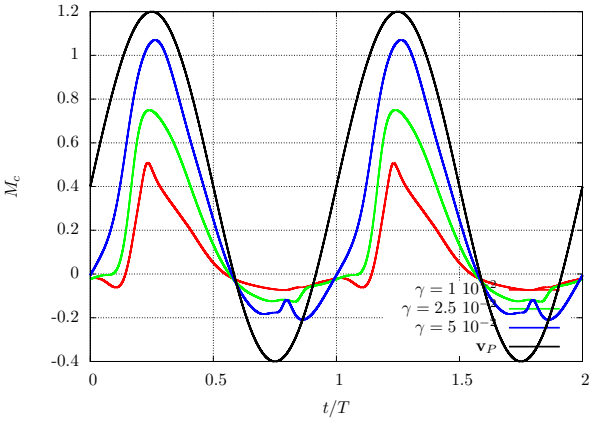

Figure 6.2.29: Time history of the moment acting at the attachment point of the filament for different bending stiffness and plate oscillation frequency $0.5\bar{f}$. The velocity of the plate is in black.

Figures 6.2.30-6.2.32 describe the time-history of the force and moment at the attachment point for frequency $0.25\bar{f}$ and different filament bending stiffness.

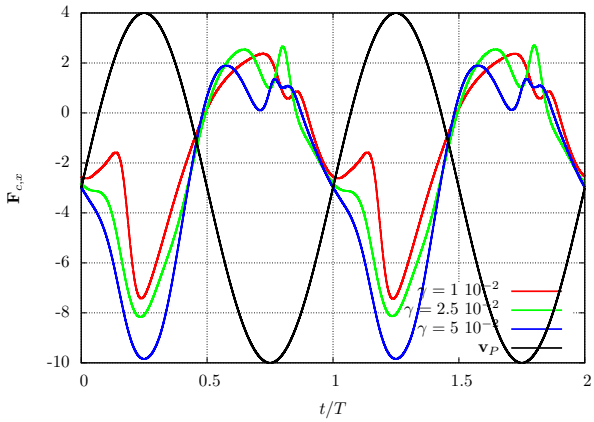

Figure 6.2.30: Time history of the x-force component acting at the attachment point of the filament for different bending stiffness and plate oscillation frequency $0.25\bar{f}$. The velocity of the plate is in black.

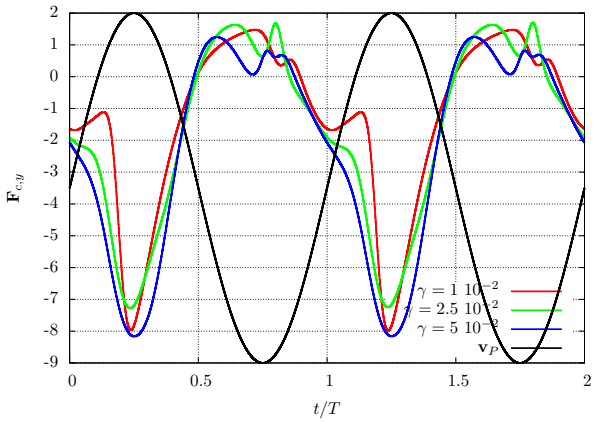

Figure 6.2.31: Time history of the y-force component acting at the attachment point of the filament for different bending stiffness and plate oscillation frequency $0.25\bar{f}$. The velocity of the plate is in black.

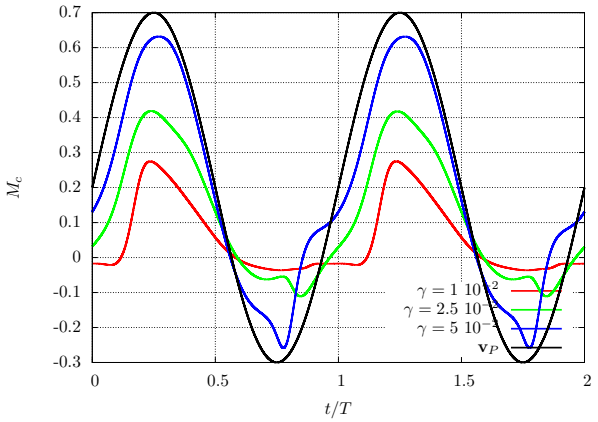

Figure 6.2.32: Time history of the moment acting at the attachment point of the filament for different bending stiffness and plate oscillation frequency $0.25\bar{f}$. The velocity of the plate is in black.

In Figure 6.2.33 we show the variation of the force and torque peak values and their corresponding times as the bending stiffness (right column) and plate oscillation frequency (left column) varies. Apart from the y-component of the force $\mathbf{F}_c$ whose dependency of γ is not univocal, the x-component of $\mathbf{F}_c$ and moment M_c increases with the oscillation frequency and the bending stiffness (left column). The peak time of both $\mathbf{F}_c$ and M_c does not vary substantially (right column), in that generally all peaks are generated during the rightward maximum acceleration of the plate (approximately at the first quarter of the cycle). The only substantial variation is in the peak time of the x-component of $\mathbf{F}_c$ (Figure 6.2.33, right column, top) as the peak value for the parameters $\gamma = 1 \cdot 10^{-2}$ and $f/\bar{f} = 1$ (unlike all the others) appears to be during the leftward acceleration of the plate (approximately at the third quarter of the cycle, Figure 6.2.24, red curve).

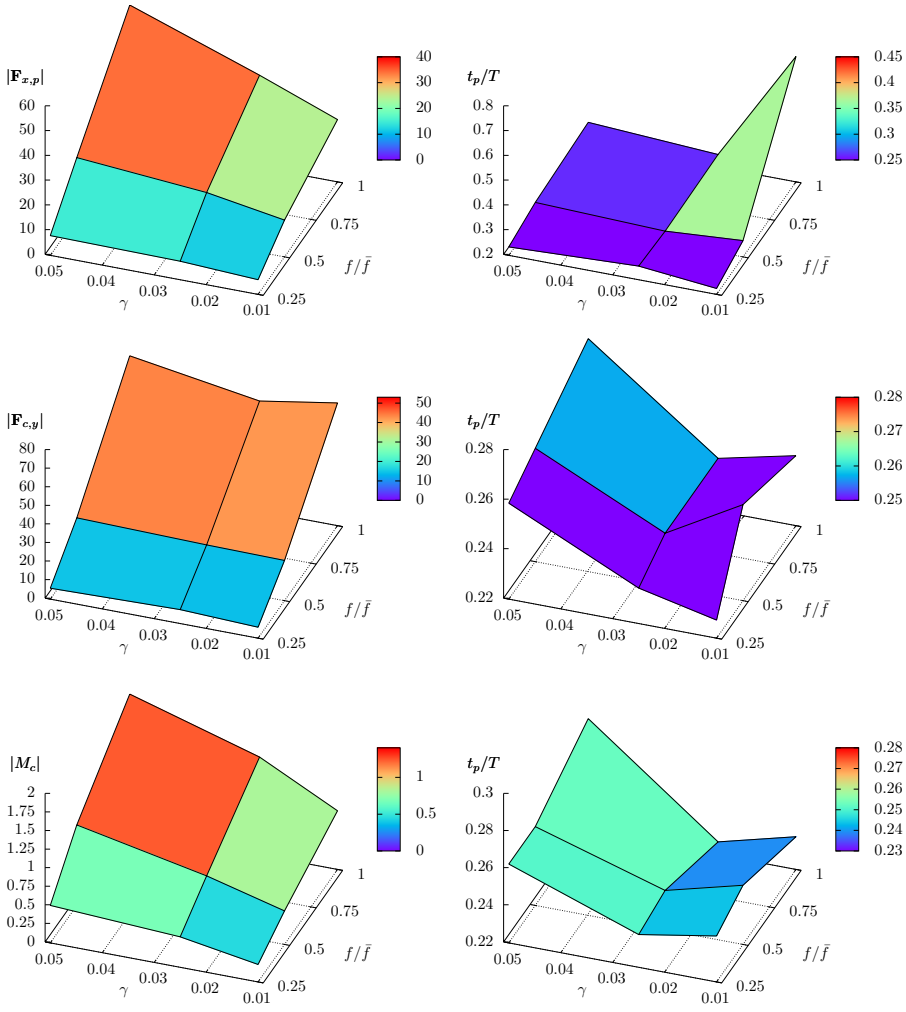

Figure 6.2.33: Surface plots of the peak values (right column) of force components $|\mathbf{F}_{c,x}|$ (first row), $|\mathbf{F}_{c,x}|$ (second row) and moment $|M_c|$ (third row) and their corresponding time t_P/T (left column) for the "periodic" case as a function of the bending stiffness γ and of the plate oscillation frequency $f/\bar{f}$.

6.2.6 Tendency to detachment

In order to study the detachment propension of the clamping force $\mathbf{F}_C$ and torque M_C exerted by the filament on the underneath substrate, we borrow from Geotechnics the simple model of a foundation on elastic soil proposed by Winkler [94]. It assumes the soil medium as a system of identical but mutually independent, closely spaced, discrete and linearly elastic springs (Figure 6.2.34).

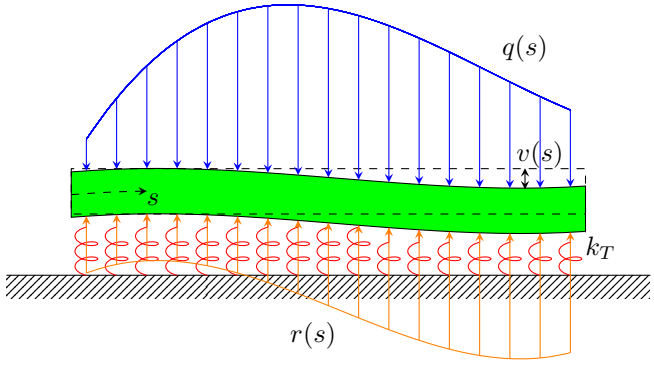

Figure 6.2.34: Foundation beam (in green) subject to an external load $q(s)$ (in blue), s being the curvilinear abscissa, and supported by elastic spring of stiffness k_T (in red). The soil reaction $r(s)$ (in orange) is proportional to the foundation displacement $v(s)$.

In this way the soil reaction $r(s)$ (in orange) is proportional to the foundation displacement $v(s)$ through the spring stiffness constant K:

$$r(s) = k_T\, v(s)$$

In our specific case the foundation beam, representing the retina, will be considered as semi-infinite, and the external load will be applied at the finite end (Figure 6.2.35).

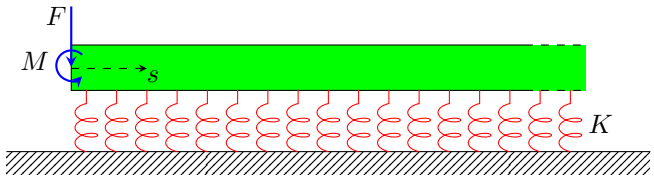

Figure 6.2.35: Semi-infinite foundation beam (in green) subject to a punctual force F and torque M at the finite end.

For this particular case there is an analytical solution for the dimensionless displacement $v(s)$, and consequently for the soil reaction $r(s)$.

$$\begin{aligned} v(s) &= \frac{e^{-\alpha s}}{2\alpha^3\gamma}\left[(\alpha M + F)\,cos\,(\alpha s) - \alpha M sin\,(\alpha s)\right] \\ &= \frac{e^{-\alpha s}}{2\alpha^3\gamma}\{\alpha M\left[cos\,(\alpha s) - sin\,(\alpha s)\right] + F cos\,(\alpha s)\} \end{aligned}$$

where F and M are the punctual force and torque applied at the beam finite end, γ is the beam bending stiffness and α is the characteristic wavelength defined as

$$\alpha^4 = \frac{k_T\,\ell}{4\gamma}. \tag{6.2.2}$$

where ℓ is the width of the beam. Figure 6.2.36 shows the substrate displacement in the "tear" configuration for typical values of the parameters ($F = 70, M = 2.5, \gamma = 0.1, \alpha = 50$).

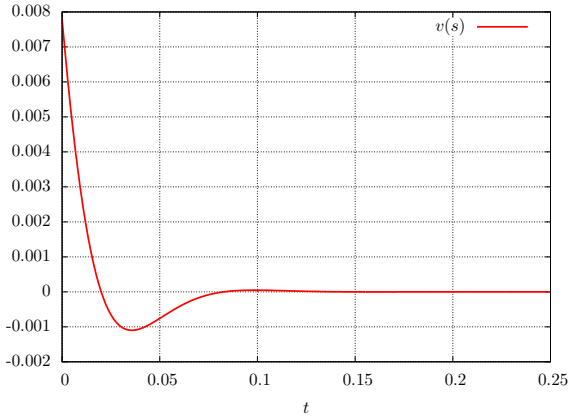

Figure 6.2.36: Winkler beam displacement for typical values of external loads ($F = 70, M = 2.5$) and system parameters ($\gamma = 0.1, \alpha = 50$) recorded in the tear case.

As it is defined, $v(s)$ is positive for negative displacements. We define as *tendency to detachment* d the negative displacement at the free end ($s = 0$), thus

$$d = -\min(v|_{s=0}, 0) = -\min(\frac{\alpha M + F}{2\alpha^3\gamma}, 0). \tag{6.2.3}$$

The parameter α is the ratio between the stiffness of the substrate and the bending stiffness of the beam. Since the substrate can be though to be more rigid than the filament, we can assume α to be "large". Figure 6.2.37 shows the maximum tendency to detachment in time for the tear and hole configuration and ratio between them for $L = 1$ and $\theta = 33.56°$. Since α multiplies the torque M, as $\alpha \to +\infty$ the ratio between the tear case and the hole left filament converges to 1.22, the ratio between the maximum torque for the respective cases.

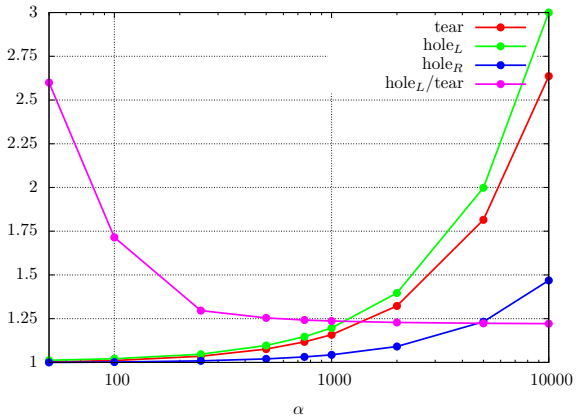

Figure 6.2.37: Tendency to detachment in the tear and hole configuration and ratio between them for $L = 1$ and $\theta = 33.56°$. As $\alpha \to +\infty$ the ratio between the tear case and the hole left filament converges to 1.22, the ratio between the maximum torque for the respective cases.

Regarding a suitable estimate for α (equation 6.2.2), we could think of k_T to be related to the Young modulus E of the retina. Since

$$r(s) = E_T\,\varepsilon = E_T \frac{v(s)}{h_c}$$

where h_c is the height of the compressible layer, it follows that $E_T = k_T h_c$, thus

$$\alpha^4 = \frac{E_T\,\ell}{4h_c\gamma}$$

and since $\gamma = EI$, where I is the area moments of inertia of the filament cross

section (assumed to be a square),

$$\alpha^4 = \frac{E_T\,\ell}{4h_c E_T I} = \frac{\ell}{4h_c \dfrac{h^3\ell}{12}} = \frac{3}{h_c h^3}$$

and, with the further assumption $h_c = h$, we get $\alpha^4 = 3/h^4$. As in our simulations $h = 1/30$ we get $\alpha \simeq 40$. In the following we will make use of this value.

6.2.7 External loads and detachment

In Figures 6.2.38 - 6.2.40 we show the tendency to detachment d in time for the tear and hole configuration for $L = 1$ and $\theta = 33.56°$. The force normal to the substrate F to be inserted in (6.2.3) has been calculated as

$$F = T\sin\theta + S\cos\theta \tag{6.2.4}$$

where T and S are respectively the tension and the shear internal reaction of the filament at the clamping point. Tendency to detachment curves $d_{\alpha=\ldots}$ have been scaled with the maximum tendency to detachment in time for the tear configuration. Positive force F and torque M have a detaching effect. Results clearly shows that the tendency to detachment in the hole case is $\simeq 3.15$ times bigger (peak in the left filament at approximately 0.51, Figure 6.2.39)

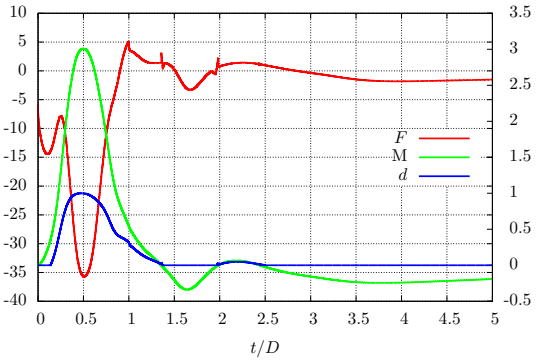

Figure 6.2.38: Punctual loads (F, M, on the left) and tendency to detachment (d, on the right) in the tear case (normalized to 1 as the reference case).

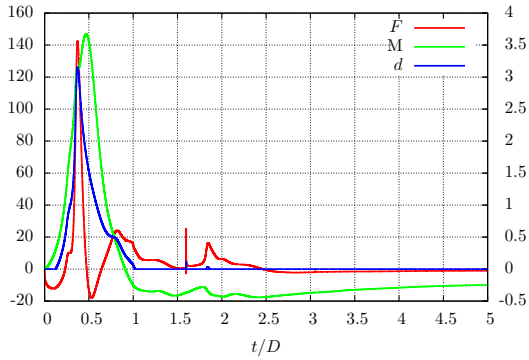

Figure 6.2.39: Punctual loads (F, M, on the left) and tendency to detachment (d, on the right) in the hole case, left filament (scaled with the maximum tendency to detachment in time for the tear configuration).

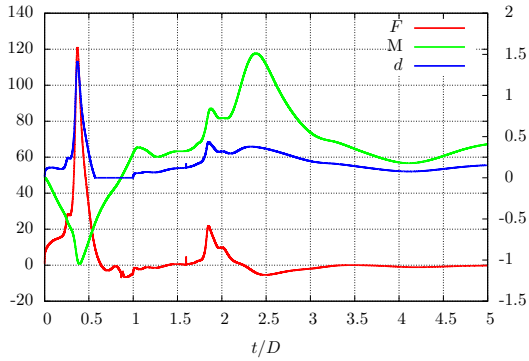

Figure 6.2.40: Punctual loads (F, M, on the left) and tendency to detachment (d, on the right) in the hole case, right filament (scaled with the maximum tendency to detachment in time for the tear configuration).

6.2.8 Tear-hole comparison

Figure 6.2.41 summarizes the tendency to detachment for the tear and hole case for $L = 1$ and $\theta = 33.56°$. Results have been scaled with the maximum tendency to detachment in time for the tear configuration.

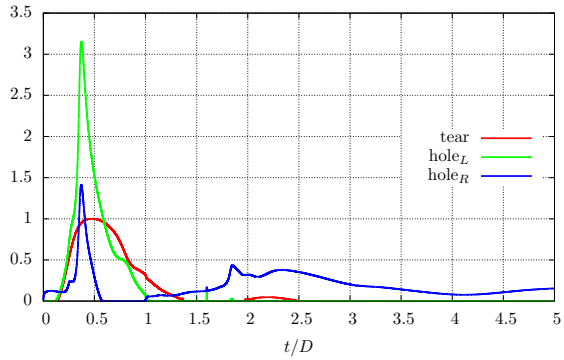

Figure 6.2.41: Tendency to detachment for the tear and hole case (right and left filaments) scaled with the maximum tendency to detachment in time for the tear configuration. Simulations for $L = 1$ and $\theta = 33.56°$.

Figures 6.2.42 and 6.2.43 respectively reports the maximum tendency to detachment in time for $L = 0.75$ and $L = 1.25$ for angle $\theta = 33.56°$.

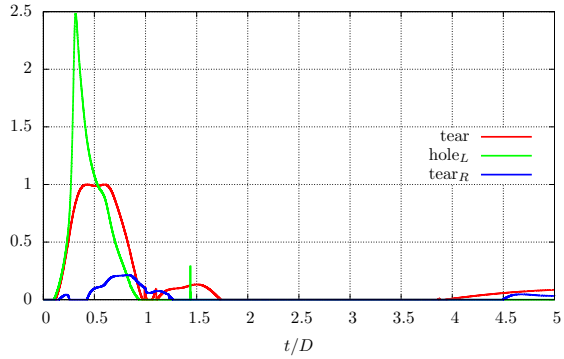

Figure 6.2.42: Tendency to detachment for the tear and hole case (right and left filaments) scaled with the maximum tendency to detachment in time for the tear configuration. Simulations for $L = 0.75$ and $\theta = 33.56°$.

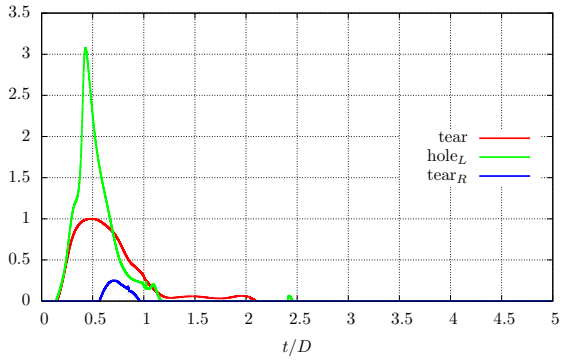

Figure 6.2.43: Tendency to detachment for the tear and hole case (right and left filaments) scaled with the maximum tendency to detachment in time for the tear configuration. Simulations for $L = 1.25$ and $\theta = 33.56°$.

In this study the plate motion is from left to right, thus the hole upwind side is represented by the right filament, while the left is on the downwind side. As the downwind part of the hole is the most stressed part, we will consider it as representative of the whole configuration. Figure 6.2.44 reports the ratio between the maximum tendency to detachment between the hole and tear configuration for different filament lengths L and $\theta = 33.56°$.

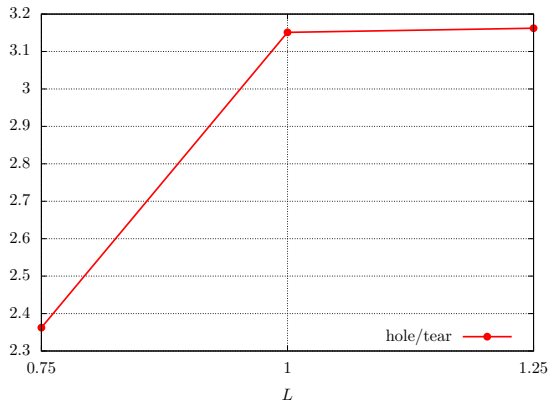

Figure 6.2.44: Ratio between the maximum tendency to detachment between the hole and tear configuration for different filament lengths L and $\theta = 33.56°$.

6.2.9 Tear comparison

Figure 6.2.45 summarizes the tendency to detachment for different tear lengths ($\theta = 33.56°$), while Figure 6.2.46 describes the tendency to detachment for different tear clamping angles θ (and $L = 1$).

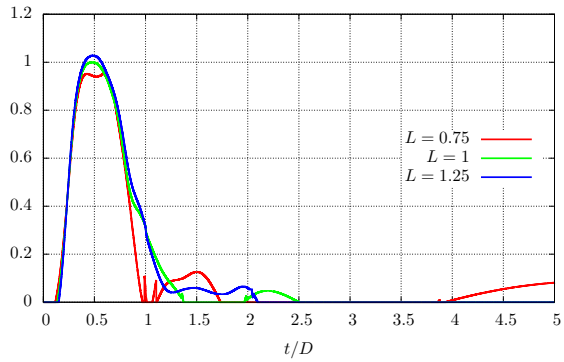

Figure 6.2.45: Tendency to detachment for the tear case with different lengths and $\theta = 33.56°$. Results have been scaled with the maximum tendency to detachment in time for $L = 1$.

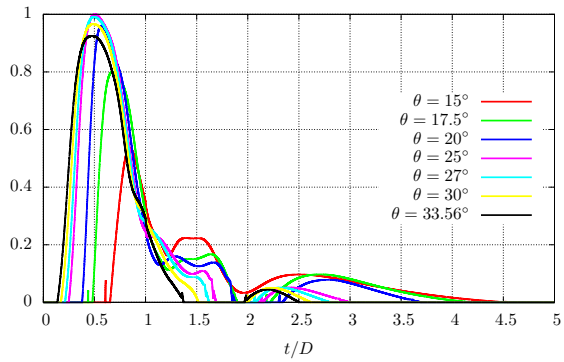

Figure 6.2.46: Tendency to detachment for the tear case with different clamping angles and $L = 1$. Results have been scaled with the maximum tendency to detachment in time for $\theta = 25°$.

Figure 6.2.47 reports the peaks of previous figures.

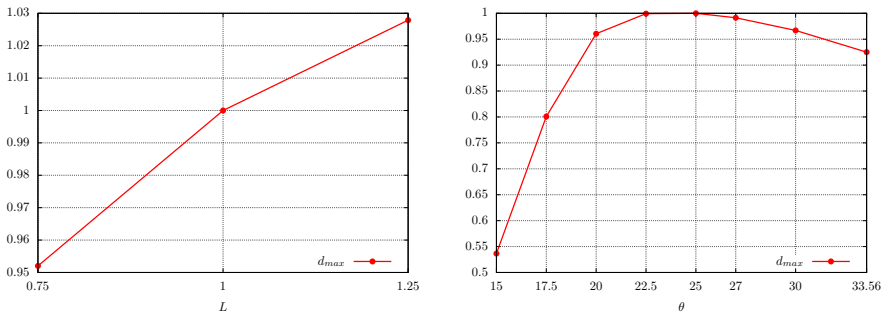

Figure 6.2.47: Maximum values of the tendency to detachment d for the tear case for different filament lengths L and $\theta = 33.56°$ (left), and for different θ and $L = 1$ (right).

6.2.10 Hole comparison

Figure 6.2.48 summarizes the tendency to detachment for different filament lengths (inter-tip distance $\Delta = 0.1\bar{6}$) while Figures 6.2.49 describes the tendency to detachment for different inter-tip distance and $L = 1$.

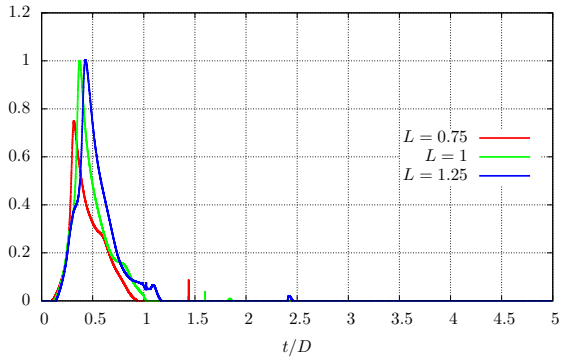

Figure 6.2.48: Tendency to detachment for the hole case (left filament) with different lengths and inter-tip distance equal to $0.1\bar{6}$. Results have been scaled with the maximum tendency to detachment in time for $L = 1$.

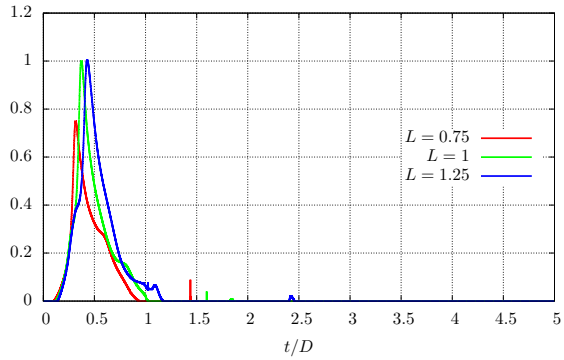

Figure 6.2.49: Tendency to detachment for the hole case (left filament) with different inter-tip distance and $L = 1$. Results have been scaled with the maximum tendency to detachment in time for $d = 0.1\bar{6}$.

Figure 6.2.50 reports the peaks of previous figures.

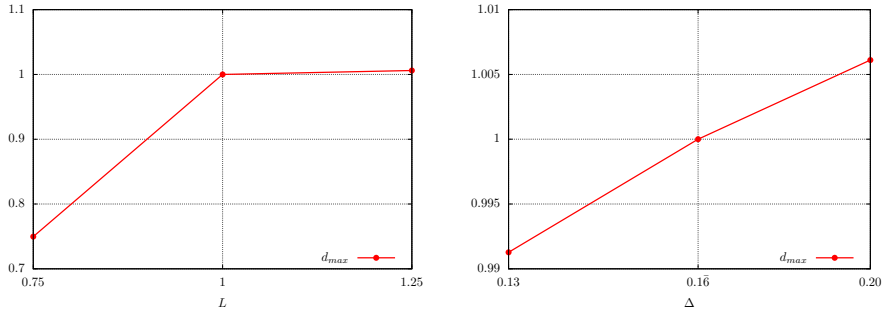

Figure 6.2.50: Maximum values of the tendency to detach d for the hole case for different filament lengths L and $\Delta = 0.1\bar{6}$ (left), and for different Δ and $L = 1$ (right).

6.2.11 Conclusions

In this study the dynamics of retinal breaks both the "tear" and the "hole" configuration, have been analyzed. Moreover, the "tear" case has also been studied in the case of a plate with periodic motion ("periodic tear").

Regarding the "tear" configuration, both the influence of filament length and clamping angle have been considered. Results (Figure 6.2.12) show that both

the clamping force $\mathbf{F}_c$ and moment M_c increase with the filament length. On the other hand, as the clamping angle increases the y-component of the force decreases while the other observed quantities increase.

Simulations of the "hole" case show that the right filament exerts on the plate the highest clamping force $\mathbf{F}_c$ to the plate, while the left one produces the highest clamping torque M_c.

The comparison of the "tear" and "hole" configurations show that the "hole" configuration generates peak values of both clamping force $\mathbf{F}_c$ and torque M_c higher than in the "tear" case. With the same bending stiffness $\gamma = 1 \cdot 10^{-1}$ and length $L = 1$, the ratio of the peak values is ~ 4 for the x-component of the force, ~ 2 for the y-component and $\simeq 1.32$ for the torque.

In the case of "periodic tear" (Figure 6.2.23) an interesting phenomena, also know as the "bullwhip effect", has been observed. In this configuration the influence of both the filament bending stiffness γ and the plate oscillation frequency has been investigated. From the results of the clamping force $\mathbf{F}_c$ and torque M_c during an entire plate oscillation (Figure 6.2.33) it appears that the peak values increase almost univocally with both bending stiffness and oscillation frequency.

6.3 Energy harvesting

Recent technical developments have opened the way to a wide spectrum of devices able to capture small amounts of energy from the environment and transform them into electrical energy. Energy harvesting (also known as power harvesting or energy scavenging) is the process by which energy is derived from environmental sources (e.g. solar power, thermal energy, wind energy, salinity gradients and kinetic energy), captured and stored. Even if energy harvesters are able to extract free and clean energy its amount, although often limited, can be suitable for small devices such as wearable electronics or wireless sensor networks, possibly scattered in inaccessible locations (Figure 6.3.1, d). Moreover a "free" energy source, maintenance-free and available throughout the lifetime of the application, can be more reliable than wall plugs or batteries [96]. Furthermore, energy harvesting can be used as an alternative energy source to supplement a primary power source and to enhance the reliability of the overall system and prevent power interruptions. All energy harvesting systems require as fundamental components:

- an energy source,
- an energy conversion device,
- an end application.

Energy is everywhere in the environment surrounding us under different forms [96] and different strategies for its extraction have been designed so far, mainly in regard to mechanical, thermal and electromagnetic energy. Mechanical energy can be extracted from natural forces such as wind or water flow, or by recovering energy from vibrations, mechanical stresses and strains. On the other hand, thermal energy can be obtained from the sun, or by intercepting wasted energy from plants or heaters, and by exploiting thermal gradients. Due to radio and television broadcasting, there is a large amount of electromagnetic energy in the environment. Moreover, electromagnetic energy is also emitted from any electric/electronic device and even from the sun.

Energy conversion devices vary depending on the exploited energy source, with electromagnetic energy being the easiest to be transformed into electrical energy. Mechanical energy can be converted by means of piezoelectric crystals [98] or dielectric elastomers [99], a polymer also known as "dielectric elastomer transducer", that generates a small electrical potential difference when deformed. Depending on the application, mechanical energy can also be converted by using an electromagnetic generator exploiting induction [100]. Solar energy is stored by means of photovoltaic cells [102], while thermal gradients can be exploited by using thermoelectric generators or the pyroelectric effect [101]. Other forms of energy (i.e. when the source is the wind or a water body) cannot be directly transformed into electricity but need to be first converted into some transitional form (usually mechanical energy) [103].
Many real life applications requiring low energy power nowadays rely on energy harvesting devices. The Seiko Watch Corporation was successful in building a Thermic watch powered entirely by exploiting the thermal gradient between the wearer's body and the external environment (Figure 6.3.1, a) [97]. The power extracted by this device is of the order of μW due to limited thermal gradients used, but thermoelectric generators can be applied to a broad range of applications where thermal gradients occur (e.g. pipes carrying hot exhaust gases in power plants), generating power up to 1 kW [104]. In particular, Thermal Electronics Corp. [105] has recently designed a device able to produce $\sim$ 50 W with a thermal gradient of $\sim 90°$ (Figure 6.3.1, b).

Several energy harvesting devices able to convert mechanical energy have been successfully designed. Solepower, a new-born company spin-off of the Carnegie Mellon University, has designed a small generator to be embedded in a shoe sole [106] that create electricity with every step. Energy is stored in a battery placed in a holster upon the shoelaces that, when charged, can be used to recharge almost any pocket device (Figure 6.3.1, c).

(a)

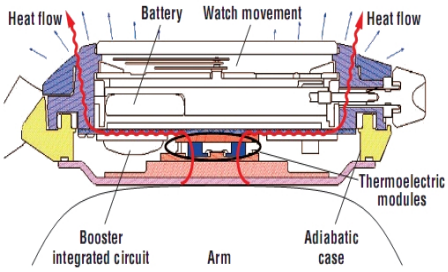

(b)

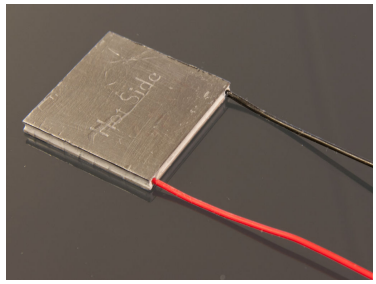

(c)

(d)

Figure 6.3.1: Energy harvesting applications: Seiko Thermic wristwatch using the Peltier-Seebeck effect (a), TEG generating electricity from temperature difference (b), SolePower EnSole producing energy from mechanical compression (c) and a solar panel powering the remote sensor located at a several-meter high location (d).

Mankind has extracted energy from wind and water for a long time [110, 109]. The earliest evidence of wind and watermills traces back to Greece in the 3rd century B.C., and since then they have become widespread around the world. At first, their their main task was to convert wind or water energy into rotational energy used to grind grain, however following technological improvements they have also been successfully applied to crush mining materials, saw wood and forge tools. Nowadays the same technology of ancient wind and water mills is used in modern wind farms and hydroelectric power stations to produce renewable energy (Figure 6.3.2, a). In 2009, the world relied on renewable sources for around 13.1% of its primary energy supply, according to International Energy Agency (IEA) statistics. In particular, global wind power capacity was 238 GW at the end of 2011, up from just 18 GW at the end of 2000, with an average growth rate of over 25% over the past five years [95]. As a general rule, wind generators require a constant wind speed of 16 km/h or greater, while water

turbines are usually installed concurrently with a water jump of the order of $\sim$ 10 m.

Due to the previous requirements the installation of both wind and water turbines (Figure 6.3.2, b) are restricted to only a few sites. To overcome this limitation, new technologies to exploit the energy of air and water have been developed. In 2002 the Ocean Power Technologies, Inc. applied for a patent for "a piezoelectric power generator, particularly for use in a flowing fluid stream. Is is comprised of an elongated, flexible central layer of a dielectric material having, spaced axially along opposite sides thereof, a plurality of separate piezoelectric elements. Each element is formed from a portion of a continuous layer of a piezoelectric layer extending along each opposite side of the central layer, sandwiched between a pair of electrodes unique to each piezoelectric element" [107]. This device, commonly referred to as a "water eel", converts the energy of the incoming water flux into mechanical energy under the form of stresses and strain, and then into electricity by means of piezoelectric elements (Figure 6.3.2, c). Analogously, a team of researchers from the Università di Genova have proposed an innovative flapping wing system to harvest energy from the motion of fluid [62, 64]. This device consists of a wing attached to two fixed points by means of two elastometers, so that in the presence of a fluid flow the wing begins to oscillate and consequently the elastometers to stretch, producing electrical energy (Figure 6.3.2, d). In the last two examples of energy harvesting the energy source was provided by the fluid motion. As stated previously, this kind of energy cannot be directly transformed into electricity but needs firstly to be converted into a more suitable form, i.e. mechanical energy. This transformation can be done in a more or less efficient way depending on the parameters of the problem. While a resonant coupling mechanism between fluid and structure has previously been regarded as a potential carrier of system failure, here the generation of self-sustained, possibly large-amplitude motion of the structure is highly desirable.

The application of flapping wings to extract energy from uniform flows was first proposed by McKinney and DeLaurier [60]. Flapping energy harvesters can be devided into the following three categories with respect to the activating mechanism of the device [61]:

- forced pitching and heaving motions (fully-activated),
- forced pitching and induced heaving motions (semi-activated),
- self-sustained pitching and heaving motions (self-sustained).

(a) (b)

(c) (d)

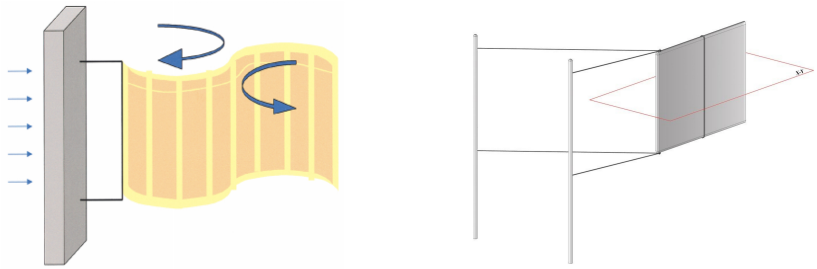

Figure 6.3.2: Traditional windmill in front of a modern wind farm (a), Francis turbine for hydroelectric power generation (b) and schematics of the water-eel and of the flapping wing energy harvesters (c-d).

While the first two categories consume some energy to control the heaving and/or pitching motion in order to maximize the harvested energy, the last class is not endowed with an imposed motion (i.e. no external energy is needed) againts a minor extracted energy. In particular, the device under study in this application belongs to the self-sustained category.

In this Section the code described in Chapter 5 has been successfully applied to the numerical investigation of the behavior of a spring-filament oscillator, very similar to the flapping wing energy harvester [62] (Figure 6.3.2, d). In particular, here we consider an impermeable 2D filament with mass and bending stiffness hinged to a pole linked by two elastometers to external fixed boundaries (not considered in the flow simulations). The filament is subject to a uniform flow and its leading edge is forced to move only in the direction normal to the incoming flow (see Figure 6.3.3). For the mathematical formulation and characteristic length scales see to Section 6.1.1.

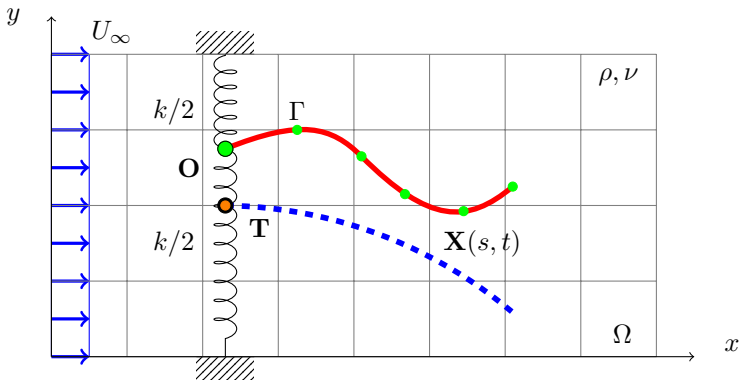

Figure 6.3.3: Filament Γ is hinged (initial condition in dashed blue line) to point **O**, constrained to move only in vertical direction and linked by two springs of stiffness $k/2$ to external fixed boundaries (not considered in the flow simulations).

As in the case of the "water eel" and the flapping wing harvester, the main idea to increase the efficiency of the device is to trigger a resonant condition between the elastic structure and the fluid flow. In this condition the motion of the leading edge is expected to produce the highest amount of energy.

6.3.1 Numerical model

Let $\mathbf{x} = (x, y) \in \Omega$ be the Cartesian physical coordinates, with Ω denoting the physical domain; let $s \in \Gamma$ be the Lagrangian curvilinear coordinate, with Γ denoting the body surface; let $\mathbf{X}(s,t) = (X_1(s,t), X_2(s,t)) \in \Gamma$ denote the physical position of each material point of curvilinear coordinate s at time t.

The governing equations for this problem are those presented in Section 6.1.2 (not considering permeability) with different boundary conditions. In particular, the equations describing the dynamics of the beam have to consider the presence of a concentrated spring force on the filament leading edge. Simple dynamical considerations tell us that the system in Figure 6.3.3 is exactly the same as one filament linked to target point **T** by a spring of doubled stiffness k. Filament dynamics is considered in equations (6.1.6) along with the boundary conditions

$$\mathbf{X}|_{s=0} = \mathbf{X}_O, \quad \left.\frac{\partial^2 \mathbf{X}}{\partial^2 s}\right|_{s=0} = 0, \quad \left.\frac{\partial^2 \mathbf{X}}{\partial^2 s}\right|_{s=L} = 0,$$

$$\left.\frac{\partial^3 \mathbf{X}}{\partial^3 s}\right|_{s=L} = 0, \quad \mathbf{X}_O \cdot x = \mathbf{X}_T \cdot x.$$

The first condition enforce the filament to follow the motion of the pole while the second derives from the hinged condition at the leading edge. The third and the fourth conditions state that the filament trailing edge is unloaded. The last condition forces the leading edge to move only in the vertical direction. On the other hand, tension in the filament is solved through equation (4.3.8) with the following conditions

$$\frac{\partial}{\partial s}\left(T\frac{\partial \mathbf{X}}{\partial s}\right)_{s=0} = -Fr\frac{\mathbf{g}}{g} + \mathbf{F} + \mathbf{F_b} + A_O, \quad T|_{s=L} = 0, \mathbf{F}_k|_{s=0} = k(\mathbf{O} - \mathbf{T}),$$

where A_O is the acceleration of the leading edge. The first one derives from equation (6.1.6), while the second again comes from the unloaded free edge condition. Finally the third considers the concentrated spring force at the leading edge to be proportional through the bending stiffness k to the displacement between the filament current leading edge and the target point.

6.3.2 Numerical Discretization

The computational domain is an 8×8 square ranging $[-2, 6]$ in the stream-wise direction and $[-4, 4]$ in the span-wise direction as in [52]. The computational grid is uniform in an inner region close to the pinned end $(0, 0)$ of the filament ($[-0.5, 3]$ in the stream-wise direction and $[-1, 1]$ in the span-wise direction) with grid spacing $1/200$ and stretched outside with a constant stretching ratio equal to 1.1. The filament length L is set equal to 1 and the Lagrangian grid is made up of 150 points, so that approximately 2 Lagrangian points appear in one Eulerian cell (as suggested in [55]). Boundary conditions on velocity are $U_\infty = (1, 0)$ at inflow, convective at outflow and symmetric at lateral sides. Since the computational grid for the flow is staggered, no boundary conditions for the pressure are needed. The initial configuration of the filament is a circular arc θ with leading edge in the resting point $\mathbf{T}$ (Figure 6.3.3, blue dashed line). Numerical scheme and solution procedure are the same of those described in 6.1.4 and 6.1.5. In all the simulations the fluid kinematic viscosity ν has been calculated to give $Re = 200$.

6.3.3 Numerical results

The first result is the identification of the optimal spring stiffness k in order to trigger a resonant condition between the flapping of the filament and the spring itself. Several simulations have been performed varying the spring stiffness k while keeping the other parameters of the problem constant and equal to

$$U = 1, \quad L = 1, \quad Re = 200, \quad \rho = 1.5, \quad \gamma = 1 \cdot 10^{-3}.$$

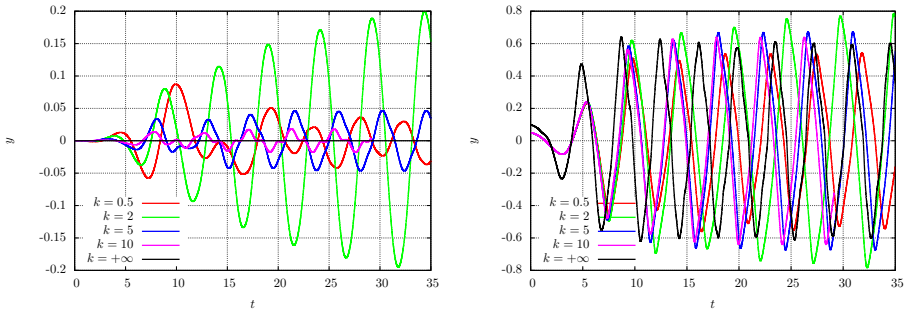

Figure 6.3.4: Time history of the y coordinate of the leading (left) and trailing (right) edge of the filament for different spring stiffness k.

Figures 6.3.4 shows the evolution in time of the leading (left) and the trailing (right) edge y coordinate, while Figure 6.3.5 shows the flapping amplitude (left) and frequency (right) of the leading and trailing edge once a stable oscillation state is reached. Results for $k \to +\infty$ were obtained by simulating a filament hinged to a fixed point as in Section 6.1.

Figure 6.3.5 clearly shows a non-symmetrical peak for $k = 1.3$ and then converges to the results obtained for the hinged filament ($k \to +\infty$), i.e. $f \simeq 0.267$ and $A_{pp} \simeq 1.27$. The resonant condition for $k = 1.3$ is associated with a sudden increase of the flapping amplitudes and drop of the flapping frequencies in both the trailing and leading edges.

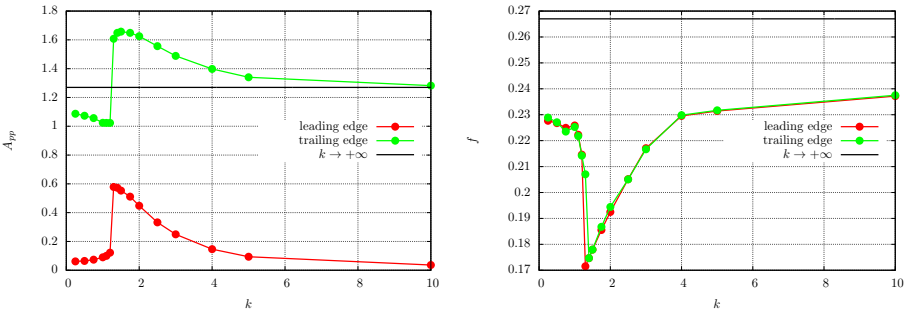

Figure 6.3.5: Flapping peak-to-peak amplitude (left) and frequency (right) of the leading and trailing edge once a stable oscillation state is reached. The solid line represents the peak-to-peak amplitude and flapping frequency of the hinged filament, i.e. $k \to +\infty$

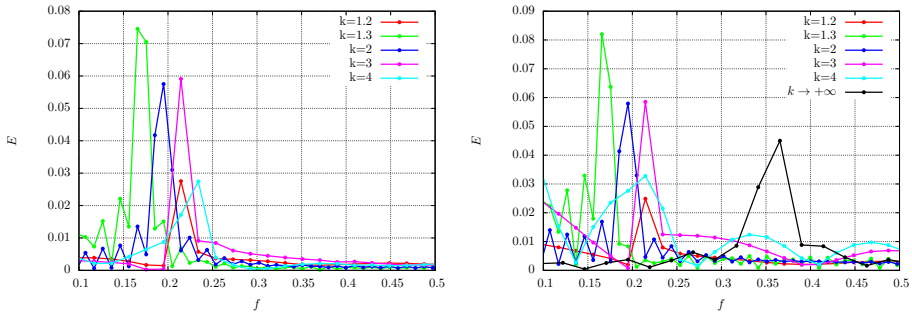

Figure 6.3.6: Frequency spectra for the leading (left) and trailing (right) edge. In the right graphics the spectrum for the case $k \to +\infty$ is also shown.

In Figure 6.3.6 the frequency spectra for both the leading (left) and the trailing (right) edge are shown. According to Figure 6.3.5 (right), the lock-in frequency at which the spring-filament system oscillates experiences a sudden drop at the occurence of the resonant condition (consider the peaks for $k = 1.2$ and $k = 1.3$), then it slowly increases. We investigate now what happens by changing the Reynolds number (i.e. the velocity of the incoming flow) varies.

As shown in Figures 6.3.7 and 6.3.8 stiffer springs will need higher Reynolds-number flow to resonate, and their resonant condition will be linked with smaller amplitude and higher frequency. Interestingly, once the resonance threshold has been exceeded the behavior of the particular spring-filament system does not change with the Reynolds number.

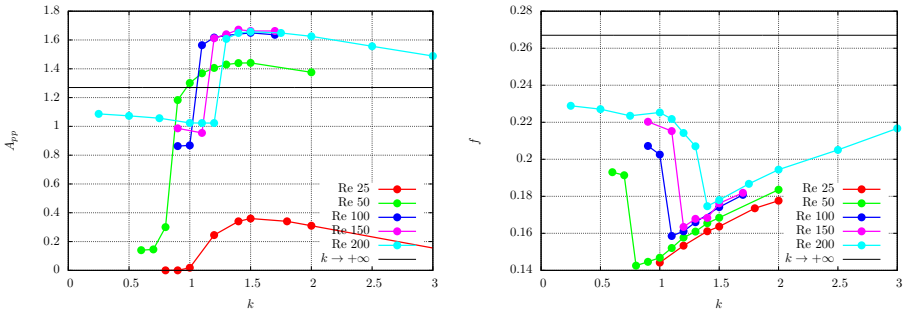

Figure 6.3.8: Flapping peak-to-peak amplitude (left) and frequency (right) of the trailing edge for different Reynolds numbers.

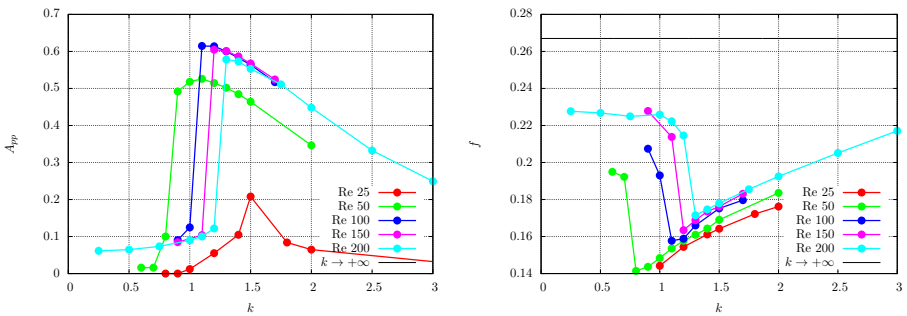

Figure 6.3.7: Flapping peak-to-peak amplitude (left) and frequency (right) of the leading edge for different Reynolds numbers.

The fact that higher Reynolds-number flows trigger a resonant condition in stiffer springs can also be demonstrated by following the theoretical reasoning in Section 2.

The natural pulsatance ω_N for a mass-spring system is

$$\omega_N = \sqrt{\frac{k}{m}}, \tag{6.3.1}$$

and

$$A = \frac{F_0}{m(\omega_N^2 - \omega_F^2)}, \tag{6.3.2}$$

i.e. $k \propto \omega_N^2$ and the oscillation amplitude has an asymptote as $\omega_N = \omega_F$, where ω_F is the pulsatance driving frequency. In this respect, the reader is

recommended to compare the numerical results shown in Figure 6.3.5 (left, red curve) and the theoretical curve in Figure 2.1.3. Table 6.3.1 shows the pulsatance ω_F of a hinged filament (as described in Section 6.1) subject to different Reynolds-number flows and the corresponding spring stiffness optimal value.

Re	$\omega_F = \omega_N$	k_{peak}
100	1.571	1
125	1.599	1.1
150	1.653	1.3
200	1.680	1.5

Table 6.3.1: Pulsatance of a hinged filament (similar to that described in Section 6.1) subject to different Reynolds-number flows and corresponding k_{peak} values.

The pulsatance of the hydrodynamical forces ω_F acting on the filament increases with the Reynolds number, thus there will be a particular Reynolds number for which $\omega_F = \omega_N$ is denoted by the oscillation amplitude maximum (Figure 6.3.7). As predicted by equation (6.3.1), Figure 6.3.9 shows the quadratic relation between the natural oscillation pulsatance ω_N and the optimal spring stiffness k_{peak}.

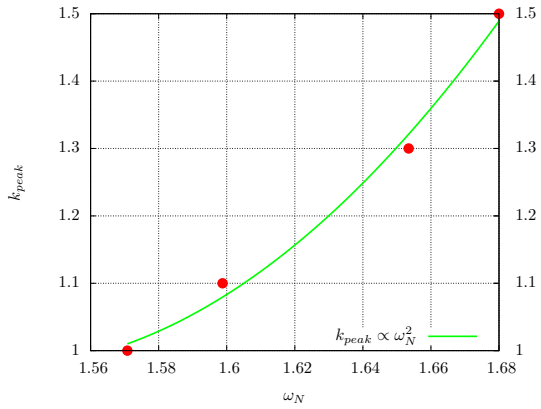

Figure 6.3.9: Relation between the natural oscillation pulsatance ω_N and the optimal spring stiffness k_{peak} as predicted by equation (6.3.1).

After considering the dynamics of the filament edges, we turn to energetic considerations. As stated in Section 6.3, this kind of device is a *self-sustained* energy harvester, in that no external power source is required to control the motion of the filament, and the harvested power will be provided by the oscillation of the leading edge, that will be linked with elastometers to external fixed boundaries. Thus, we can write the mean produced power over a period T as:

$$\bar{P} = \frac{1}{T}\int_T \mathbf{F}\cdot\mathbf{v}dt, \tag{6.3.3}$$

where $\mathbf{F}$ and $\mathbf{v}$ are respectively the force exerted by the external links and the velocity of the leading edge. Moreover we can write $\mathbf{F}$ from a simple force balance as

$$\mathbf{F} = k\mathbf{x} + \nu\dot{\mathbf{x}} + m\ddot{\mathbf{x}},$$

where k and ν are respectively the elastometer elastic and viscous constant while m is possible mass on the filament tip (usually mush greater than the filament mass itself). If we consider that the filament tip is compelled to move only in the span-wise direction we can write

$$\bar{P} = \frac{1}{T}\int_T \left(kx + \nu\dot{x} + m\ddot{x}\right)\dot{x}dt.$$

Given that the cyclic integral (line integral on a closed line) of the product between a quantity and its derivative is null, the above relation becomes

$$\bar{P} = \frac{\nu}{T}\int_T \dot{x}^2 dt. \tag{6.3.4}$$

Equation (6.3.4) clarifies the important of the elastometers viscous part: without it, it would be impossible to extract energy from this device since the force $\mathbf{F}$ and the velocity $\mathbf{v}$ (see equation 6.3.3) would be *in quadrature*. Unfortunately, the mean power extracted $\bar{P}$ does not scales linearly with the viscous coefficient ν in that the integral (i.e. the dynamics of the leading edge) will decay with higher ν.

Following equation (6.3.4) we are able to compare the device performance with different spring stiffness k. As an example, Figure 6.3.10 shows both the leading edge position and squared velocity during one oscillation cycle for $Re = 200$ and $k = 0.25$. The instantaneous extracted power ($\propto \dot{x}^2$) is null when the leading edge reaches one of the two oscillation extrema.

In Figure 6.3.11 the mean extracted power $\bar{P}$, normalized with its maximum value, is shown as a function of the spring stiffness k. As expected it resembles closely the flapping amplitude graph (see Figure 6.3.5, left), except that the mean power peak is found for $k = 1.5$ while the flapping amplitude peak was for $k = 1.3$.

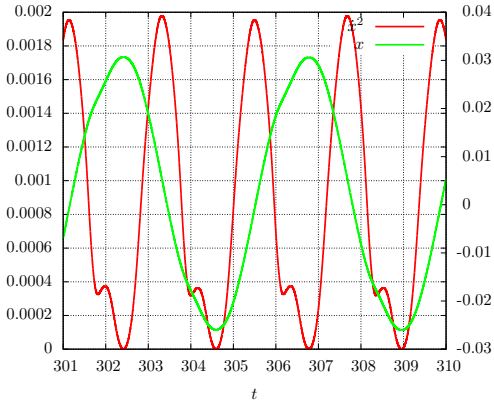

Figure 6.3.10: Position x and squared velocity $\dot{x}^2$ during one oscillation cycle for $Re = 200$ and $k = 0.25$

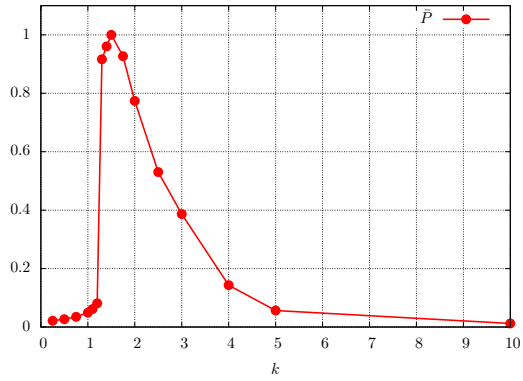

Figure 6.3.11: Mean extracted power $\bar{P}$ as a function of the spring stiffness k for $Re = 200$. The peak value is found for $k = 1.5$.

6.3.4 Conclusions

In this study we have applied our developed numerical code to a self-sustained flapping energy harvester. The working principle of this kind of device is the onset of a flutter instability between the elastic force of the connecting springs

and the fluid forces exerted by the incoming flow. In this way, the leading edge of the filament begins to oscillate in the span-wise direction making the connecting link to stretch, thus producing energy. Our primary aim is thus to find an optimal value for the spring stiffness k in order to trigger a resonant condition by making the spring natural frequency nearer and nearer to the fluid force frequency.

Through numerical simulations we have been able to follow (Figure 6.3.4) the time evolution of both the leading and the trailing edges. Once a steady self-sustained oscillation is reached, both the curve of oscillation amplitude and frequency versus bending stiffness (Figure 6.3.5) show a non-symmetric maximum for $k = 1.3$, confirmed also by the Fourier analysis shown in Figure 6.3.6.

As the incoming flow condition varies between $100 < Re < 200$ (Figures 6.3.7 and 6.3.8) the optimal value of k increases with the Reynolds number while its maximum oscillation amplitude decreases slightly. Interestingly, after the onset of the lock-in the oscillations of the spring-filament system have the same features for a given spring disregarding of the Reynolds number. In this range of Reynolds number the dependence of the optimal spring stiffness k with the Reynolds number can be predicted with the simple relation (6.3.2) proved in Section 2 (see Figure 6.3.9). If we further decrease the Reynolds numbers ($Re < 50$, Figures 6.3.7 and 6.3.8), however, the optimal k increases while its maximum oscillation amplitude decreases.

In the end, some energetic considerations are drawn. For a self-sustained flapping energy harvester the net mean power extracted for the wind can be computed following equation (6.3.4). Following this equation, Figure 6.3.11 shows the mean power $\bar{P}$ extracted from the device for different values of the spring stiffness k. Even if this curve resembles the one for the oscillation amplitude (Figure 6.3.5, left), the maximum value is found for a slightly higher spring stiffness, $k = 1.5$. Quite interestingly this value coincide with the location of the maximum for the trailing edge oscillation amplitude (Figure 6.3.5, right, green curve). This tell us that even if the power is extracted from the motion of the leading edge, it's the dynamics of the whole filament that determines its amount.

7

Conclusions and future developments

This thesis aims to be an original contribution to the understanding of how different structural parameters of biological surfaces (mass, bending stiffness and permeability) play a role in the overall fluid-dynamical behavior when exposed to the action of a flow. As we are taking into account slender and compliant structures, the common thread of the thesis is fluid-structure interaction, the two-way coupling between fluid and structure in terms of both forces and displacements.

The numerical investigation has been carried out through a finite volume code developed in the Matlab© environment. As for similar works, an immersed boundary approach has been exploited in order to efficiently handle elastic and compliant structures interacting with a viscous incompressible flow. In order to limit the required computational power, the developed code takes into account 1D structures surrounded by a 2D flow. This numerical tool fits well with the physical phenomenon under study in that feathers, hair and other biological appendages can be regarded as a 1D slender structure immersed in a surrounding 2D fluid. As a result, both the structure and the flow are supposed to be constant in the direction normal to the simulation plane.

Several methodologies considering mass and bending stiffness have been proposed in the literature. The original contribution of the present thesis is an innovative and numerically stable way to include permeability along with the other parameters. The resulting numerical code is thus able to consider mass, bending stiffness and permeability at the same time.

In particular this thesis focuses on the effects of permeability on the aerodynamical properties in terms of stability and transmitted forces. In this sense permeability can be regarded as a new control strategy of the fluid-structure interaction by allowing a mass flux and thus the modification of the pressure distribution on the surface.

The numerical tool developed during this thesis has also proven to be efficient

for simulating fluid-structure problems involving both fixed and moving rigid objects (such as free-falling bodies) with elastic and permeable appendages as in [70, 112]. Indeed it has been adapted to simulate the dynamics of retinal detachment, one of the most frequent causes of blindness in Western countries. For this application, two different detachment configurations ("tear" and "hole") have been taken into consideration in order to determine which one is more prone to further deterioration.

Finally the present code has been exploited to design the optimal parameters for a spring-filament system, a slender structure with the leading edge constrained to a spring, inspired by devices used to harvest energy. The operating principle of the optimized system consists of the triggering of a resonant behavior between the fluid forces acting on the filament and elastic forces exerted by the spring. In this way, the displacements of the leading edge and thus the energetic efficiency of the device are maximized.

A possible and straightforward development of the code would be the insertion of the 3-dimensional direction, although this step would involve a plan to overcome computational limits. Some possible strategies are (a) the migration from an interpreted language as Matlab© to a more efficient compiled language (C++, Fortran, ...), (b) the use of parallel computing.

An interesting development of the code, which would not necessarily involve previous extensive modifications, would be the implementation of 2-dimensional structures in a 2-dimensional flow as in [113, 114] by following an Immersed Boundary approach. This extension would permit not only the analysis of slender membranes but also compliant blunt elastic structures, thus multiplying the possible applications of the code.

DNS simulations are confined to low Reynolds numbers ($\sim o(10^2)$) by the spatial resolution of the grid. In order to simulate the behavior at higher Reynolds numbers, a possible solution would be to migrate from DNS to LES [115] or RANS [116] with the implementation of suitable turbulence models.

Aknowledgments

I have really enjoyed my PhD, and writing this thesis too. Here I would gratefully aknowledge some people without whom this would have not been possible, or at least not to this extent.

Therefore I would like to thank professor Alessandro Bottaro for believing in me doing a PhD in Fluid Dynamics, and for continuously supporting and encouraging worthy students.

Then we come to my guide in this long and exciting journey, professor Jan Pralits. For what he has taught me and for having been such an example to me, *tack*.

I am also greatly indebted to professor Andrea Mazzino for his enlightening explanations that more than once lighted the insidious pitfalls of my quest.

I would like to thank my external examiners, professors Alfredo Pinelli and Shervin Bagheri, for their precious observations on the thesis. In particular, I would like to thank professor Bagheri for tutoring me in the initial part of my PhD and during my period in Stockholm.

A special thank to Ms. Wendy McQuarrie for proofreading this thesis and finding out most of the errors you have not seen.

During every journey you need a shelter and true friends in there. For me it has been the *ex-Flubio* office and all the guys I met in there along these years.

Last but not least, *grazie alla mia π, mamma, papà e Marta*.

Bibliography

[1] d'Alembert, J. le R., "Essai d'une nouvelle théorie de la résistance des fluides", (1752).

[2] Prandtl, L., "Motion of fluids with very little viscosity", in *NACA Technical Memorandum*, **452** (1904).

[3] Flatt, J., "The History of Boundary Layer Control Research in the United States of America", in *Boundary Layer and Flow Control*, ed. G. V. Lachmann, 1:122-143, Pergamon Press, New York (1961).

[4] da Vinci, L., "Codex on the Flight of Birds", (circa 1505).

[5] Smithsonian National Air and Space Museum, in *airandspace.si.edu*, retrieved on September 17$^{\text{th}}$ November (2014).

[6] Velcro Industries B. V., in *velcro.co.uk*, retrieved on September 17$^{\text{th}}$ November (2014).

[7] Korb J., Linsenmair K. E., "The architecture of termite mounds: a result of a trade-off between thermoregulation and gas exchange?", in *Behavioral Ecology*, **10**, 3, 312-316 (1999).

[8] Hennighausen A., Roston E., "14 Smart Inventions Inspired by Nature: Biomimicry", in *bloomberg.com*, retrieved on September 17$^{\text{th}}$ November (2014).

[9] Wadia, A., P., McAdams, D., A., "Developing biomimetic guidelines for the highly optimized and robust design of complex products or their components", in *Proc. of the ASME 2010 International Design Engineering Technical Conferences & Computers and Information in Engineering Conference* (2010).

[10] Schlichting, H., Gersten, K., "Boundary Layer Theory", Springer-Verlag (2000).

[11] Bushnell, D. M., "Drag reduction in nature", in *Annu. Rev. Fluid Mech.*, **23**, 65-79 (1991).

[12] Favier, J., Dauptain, A., Basso, D., Bottaro, A., "Passive separation control using a self-adaptive hairy coating", in *J. Fluid Mech.*, **627**, 451-483 (2009).

[13] Dauptain, A., Favier, J., Bottaro, A., "Passive separation control using a self-adaptive hairy coating", in *Journal of Fluids and Structures*, **24**, 1156-1165 (2008).

[14] Bechert, D. W., Bruse, M., Hage, W., Meyer, R., "Biological Surfaces and their Technological Application - Laboratory and Flight Experiments on Drag Reduction and Separation Control", in *American Institute of Aeronautics and Astronautics* (1997).

[15] Fish, F. E., Lauder, G. V., "Passive and Active Flow Control by Swimming Fishes and Mammals", in *Annu. Rev. Fluid Mech.*, **38**, 193-224 (2006).

[16] Choi, H., Park, H., Sagong, W. and Lee, S., "Biomimetic flow control based on morphological features of living creatures", in *Physics of Fluids*, **24**, 121302 (2012).

[17] Bottaro, A., "Superhydrophobic surfaces for drag reduction" (2014).

[18] Bannash, R., "Experimental investigation on the boundary layer development in swimming penguins: mechanism of drag reduction and turbulence control", in *10^{th} European Drag Reduction Working Meeting* (1997).

[19] Schultz, M. P., "Effects of coating roughness and biofouling on ship resistance and powering", in *Biofouling*, **23**, 331-341 (2007).

[20] Sonak, S., "Implications of organotins in the marine environment and their prohibition", in *J. Environ. Manage.*, **90**, S1-S3 (2009).

[21] Whale Power, in *whalepower.com*, retrieved on September 17$^{\text{th}}$ November (2014).

[22] Todd, D. K., Mays, L. W., "Groundwater Hydrogeology", 3$^{\text{rd}}$ Ed., Wyley ed. (2005).

[23] Nunes, P. N., Peinemann, K-W., "Membrane technology in the Chemical Industry", 2$^{\text{nd}}$ Ed., Wyley-VCH ed. (2005).

[24] Kanwar, Y. S., Linker, A., Farquhar, M., G., "Increased permeability of the glomerular basement membrane to ferritin after removal of glycosaminoglycans (heparan sulfate) by enzyme digestion.", in *The Journal of cell biology*, **86**, 2, 688-693 (1980).

[25] Glück, M., Breuer, M., Durst, F., Halfmann, A., Rank, E., "Computation of fluid-structure interaction on light weight structures", in *J. of Wind Eng. and Indus. Aerody.*, **89**, 1352-1368 (2001).

[26] Schäfer, M., Sieber, G., Sieber, R., Teschauer, I., "Coupled fluid-solid problems: Examples and reliable numerical simulation", in *Proc. of Trends in Computational Structural Mechanics* (2001).

[27] Zhang, H., Liu, L., Dong, M., Sun, H., "Analysis of wind-induced vibration of fluid-structure interaction system for isolated aqueduct bridge" in *Engineering Structures*, **46**, 28-37 (2013).

[28] Weaver, D., S., "A review of cross-flow induced vibrations in heat exchanger tube arrays", in Journal of Fluids and Structures, **2**, 1, 73-93 (1988).

[29] Païdoussis, M., P., "A review of flow-induced vibrations in reactors and reactor components", in Nuclear Engineering and Design, **74**, 1, 31-60 (1983).

[30] Childs, D., W., "Fluid-Structure Interaction Forces at Pump-Impeller-Shroud Surfaces for Rotordynamic Calculations", in *Journal of Vibration and Acoustics*, **111**, 3, 216-225 (1989).

[31] Howe, M. S., "Elastic Blade-Vortex Interaction Noise", in *Journal of Sound and Vibration*, **177**, 3, 325-336 (1994).

[32] Lund, E., Møller, H., Jakobsen, L., A., "Shape design optimization of stationary fluid-structure interaction problems with large displacements and turbulence", in *Structural and Multidisciplinary Optimization*, **25**, 5-6, 383-392 (2003).

[33] Allen, M., Maute, K., "Reliability-based shape optimization of structures undergoing fluid-structure interaction phenomena", in *Computer Methods in Applied Mechanics and Engineering*, **194**, 30-33, 3472-3495 (2005).

[34] Bathe, M., Kamm, R., D., "A Fluid-Structure Interaction Finite Element Analysis of Pulsatile Blood Flow Through a Compliant Stenotic Artery", in *Journal of Biomechanical Engineering*, **121**, 4, 361-369 (1999).

[35] Toriia, R., Oshimab, M., Kobayashic, T., Takagib, K., Tezduyar, T., E., "Fluid-structure interaction modeling of blood flow and cerebral aneurysm: Significance of artery and aneurysm shapes", in *Computer Methods in Applied Mechanics and Engineering*, **198**, 45-46, 3613-3621 (2009).

[36] De Hart, J., Peters, G., W., M., Schreurs, P., J., G., Baaijens, F., P., T., "A three-dimensional computational analysis of fluid-structure interaction in the aortic valve", in *Journal of Biomechanics*, **36**, 1, 103-112 (2003).

[37] Wall, W., A., Rabczuk, T., "Fluid-structure interaction in lower airways of CT-based lung geometries", in *International Journal for Numerical Methods in Fluids*, **57**, 5, 653-675 (2008).

[38] Di Martino, E., S., Guadagni, G., Fumero, A., Ballerini, G., Spirito, R., Biglioli, P., Radaelli, A., "Fluid-structure interaction within realistic three-dimensional models of the aneurysmatic aorta as a guidance to assess the risk of rupture of the aneurysm", in *Medical Engineering & Physics*, **23**, 9, 647-655 (2008).

[39] Liu, Z., S., Luo, X., Y., Lee, H., P., Lu, C., "Snoring source identification and snoring noise prediction", in *Journal of Biomechanics*, **40**, 4, 861-870 (2007).

[40] Cengel, Y. A., Cimbala, J. M., "Fluid Mechanics. Fundamentals and applications", 4th ed. Mc Graw Hill, New York (2006).

[41] Gad-el-Hak, M., "Flow Control. Passive, Active, and Reactive Flow Management", University Press, Cambridge (2000).

[42] Luchini, P., Manzo, F., Pozzi, A., "Resistance of a grooved surface to parallel flow and cross-flow", in *J. Fluid Mech.*, **228**, 87-109 (1991).

[43] Lissaman, P., B., S., "Low-Reynolds-Number Airfoils", in *Annual Review of Fluid Mechanics*, **15**, 1, 223-239 (1983).

[44] Fomin, V., M., Zapryagaev, V., I., Lokotko, A., V., Volkov, V., F., Lutskii, A., E., Menshov, I., S., Maksimov, Yu. M., Kirdyashkin, A. I., "Aerodynamic characteristics of a body of revolution with gas-permeable surface areas", in *J. of Appl. Mech. and Tech. Phys.*, **51**, 1, 65-73 (2010).

[45] Collar, A. R., "The first fifty years of aeroelasticity", in *Aerospace 2*, **5**, 12-20 (1978).

[46] Chorin, A., J., "Numerical Solution of the Navier-Stokes Equations", in *Math. Comp.*, **22**, 104, 745-762 (1968).

[47] Ferziger, J., H., Perić, M, "Computational Methods for Fluid Dynamics", Springer ed. (2002).

[48] Griffith, B., E., "On the volume conservation of the immersed boundary method", in *Global Science Preprint*, submitted article.

[49] Perot, J., B., "An Analysis of the Fractional Step Method", in *J. Comp. Phys.*, **108**, 51-58 (1993).

[50] Peskin, C., S., "Flow patterns around heart valves: a numerical method", in *J. Comp. Phys.*, **10**, 252-271 (1972).

[51] Temam, R., "Une méthode d'approximation des solutions des équations Navier-Stokes", in *Bull. Soc. Math.*, **98**, 115-152 (1968).

[52] Huang, W.-X., Shin, S. J., and Sung, H. J., "Simulation of Flexible Filaments in a Uniform Flow by the Immersed Boundary Method", in *Journal of Computational Physics*, **226**, 2206-2228 (2007).

[53] Natali D., http://www.dicca.unige.it/natali/research.html

[54] Taira, K. & Colonius, T., "The immersed boundary method: A projection approach", in *Journal of Computational Physics*, **225**, 2118-2137 (2007).

[55] Kim, Y. & Peskin, C. S., "Penalty immersed boundary method for an elastic boundary with mass", in *Physics of Fluids*, **19**, 053103 (2007).

[56] Favier, J., Revell, A., and Pinelli, A., "A Lattice Boltzmann-Immersed Boundary method to simulate the fluid interaction with moving and slender flexible objects", in *Journal of Computational Physics*, **261**, 145-161 (2014).

[57] Pinelli, A., Naqavi, I., Z., Piomelli, U., and Favier, J., "Immersed-boundary methods for general finite-difference and finite-volume Navier-Stokes solvers", in *Journal of Computational Physics*, **229**, 24, 9073-9091 (2010).

[58] Uhlmann, M., "An immersed boundary method with direct forcing for the simulation of particulate flows", in *Journal of Computational Physics*, **209**, 2, 448 - 476 (2005).

[59] Goldstein, D., Handler, R., Sirovich, L., "Modeling a no-slip flow boundary with an external force field", in *J. Comput. Phys.*, **105**, 354-366 (1993).

[60] McKinney, W., and DeLaurier, J., "Windmill: An Oscillating-Wing Windmill", in *Journal of Energy*, **5**, 2 (1981).

[61] Xiao, Q., and Zhu, Q., "A review on flow energy harvesters based on flapping foils", in *Journal of Fluids and Structures*, **46**, 174-191 (2014).

[62] Boragno, C., Festa, R., and Mazzino, A., "Elastically bounded flapping wing for energy harvesting", in *Applied Physics Letters*, **100**, 253906 (2012).

[63] Orchini, A., Mazzino, A., Guerrero, J., and Boragno, C., "Flapping states of an elastically anchored plate in a uniform flow with applications to energy harvesting by fuid-structure interaction", in *Physics of Fluids*, **25**, 097105 (2013).

[64] Alinovi, E., "Un metodo originale ed innovativo per l'energy harvesting", Bachelor Thesis in Mechanical Engineering (2011).

[65] Rayleigh, L., "On the instability of jets", in *Proc. Lond. Math. Soc.*, **10**, 4-13 (1879).

[66] Zhu, L., and Peskin, C. S., "Simulation of a Flapping Flexible Filament in a Flowing Soap Film by the Immersed Boundary Method", in *Journal of Computational Physics*, **179**, 452-468 (2002).

[67] Peskin, C. S., "The Immersed Boundary Method", in *Acta Numerica*, 1-39 (2002).

[68] Kim, Y., and Peskin, C. S., "2-D Parachute Simulation by the Immersed Boundary Method", in *SIAM Journal on Scientific Computing*, **28** (6), 2294-2312 (2006).

[69] Roma, A. M., Peskin, C. S., Berger, M. J., "An adaptive version of the immersed boundary method", in *Journal of Computational Physics*, **153**, 509-534 (1999).

[70] Bagheri, S., Mazzino, A., and Bottaro, A., "Spontaneous Symmetry Breaking of a Hinged Flapping Filament Generates Lift", in *Physical Review Letters*, **109**, 154502 (2012).

[71] Connell, B. S. H., and Yue, D. K. P., "Flapping dynamics of a flag in a uniform stream", in *J. Fluid Mech.*, **581**, 33-67 (2007).

[72] Munk, M. M., "The aerodynamic forces on airship hulls", in *NACA Reports*, **184**, (1924).

[73] Lighthill, M. J., "Note on the swimming of slender fish", in *J. Fluid Mech.*, **581**, 33-67 (2007).

[74] Coene, R., "Flutter of slender bodies under axial strain", in *Appl. Sci. Res.*, **49**, 175-187 (1992).

[75] Argentina, M., Mahadevan, L., "Fluid-flow-induced flutter of a flag", in *Proc. N. A. S*, **102** (6), 1829-1834 (2005).

[76] Shelley, M. J., and Zhang, J., "Flapping and bending bodies interacting with fluid flows", in *Annu. Rev. Fluid Mech.*, **43**, 449-465 (2011).

[77] Kovacs, S. J., McQueen, D. M., and Peskin, C. S., "Modeling cardiac fluid dynamics and diastolic function", in *Philos. Trans. R. Soc. Lond. Ser. A*, **359**, 1299-1314 (2001).

[78] Fauci, L. J., and Peskin, C. S., "A computational model of aquatic animal locomotion", in *J. Comput. Phys.*, **77**, 85-105 (1988).

[79] Beyer, R. P., "A computational model of the cochlea using the immersed boundary method", in *J. Comput. Phys.*, **98**, 145-162 (1992).

[80] Procaccia, I., L'vov, V. S., Benzi, R., "Theory of drag reduction by polymer in wall-bounded turbulence", in *Rev. Mod. Phys.*, **80**, 225-247 (2008).

[81] Atkins, P., W., "Physical Chemistry", 5th ed. W. H. Freeman and Company, New York (1994).

[82] Gere, J. M., Timoshenko, S. P., "Mechanics of Materials", 4th ed., PWS Publishing Company, Boston (1997).

[83] Volterra, E., Zachmanoglou, E., C., "Dynamics of Vibrations", Charles E. Merrill Books inc., Columbus (1965).

[84] Winkler, E., "Die Lehre Von Elasticitaet Und Festigkeit", 1st Edn., H. Dominicus, Prague (1867).

[85] Repetto, R., Stocchino, A., Cafferata, C., "Experimental investigation of vitreous humour motion within a human eye model", in *Phys. Med. Biol.*, **50**, 4729-4743 (2005).

[86] Leveque, R. J., "Finite Difference Methods for Ordinary and Partial Differential Equations: Steady-state and Time-dependent Problems", Society for Industrial and Applied Mathematics (SIAM), Philadelphia (2007).

[87] David, T., Smye, S., Dabbs, T. and James, T., "A model for the fluid motion of vitreous humour of the human eye during saccadic movement", in *Phys. Med. Biol.*, **43**, 1385-99 (1998).

[88] Becker, W., "The Neurobiology of Saccadic Eye Movements", ed. R. H. Wurtz and M. E. Goldberg, Amsterdam (1989).

[89] Ghia, U., Ghia, K. N. and Shin, C. T., "High-Re Solutions for Incompressible Flow Using the Navier-Stokes Equations and a Multigrid Method", in *J. Comput. Phys.*, **48**, 387-411 (1982).

[90] Favier J., Dauptain A., Basso D. and Bottaro A., "Passive separation control using a self-adaptive hairy coating", *J. Fluid Mech.*, **627**, 451-483 (2009).

[91] Lundell, F., Söderberg, L. D. and Alfredsson, P. H., "Fluid Mechanics of Papermaking", *Annu. Rev. Fluid Mech.*, **43**, 195-217 (2011).

[92] Ryan, S.J. and Schachat, A.P. and Wilkinson, C.P. and Hinton, D.R. and Sadda, S.V.R. and Wiedemann, P., "Retina", Elsevier Health Sciences (2012).

[93] Sodhi, A., Leung, L., S., Do, D., V., Gower, E., W., Schein, O., D., and Handa, J., T., "Recent trends in the management of rhegmatogenous retinal detachment", in *Survey of Ophthalmology*, **53**, 50-67 (2008).

[94] Winkler, E., "Die Lehre von der Elastizitat und Festigkeit", Dominicus, Prague (1867).

[95] International Energy Agency, in *iea.org*, retrieved on November 17$^{\text{th}}$ (2014).

[96] "What is energy harvesting?", in *energyharvesting.net*, retrieved on September 21$^{\text{st}}$ November (2014).

[97] Qi, Y., and McAlpine, M., C., "Nanotechnology-enabled flexible and biocompatible energy harvesting", in *Energy Environ. Sci.*, **3**, 1275-1285 (2010).

[98] Tadesse, Y., Zhang, S., and Priya, S., "Multimodal Energy Harvesting System: Piezoelectric and Electromagnetic", in *J. Intell. Mater. Syst. and Struct.*, **20**, 5, 625-632 (2009).

[99] Kornbluha, R., D., Pelrinea, R., Prahlada, H., Wong-Foya, A., McCoya, B., Kima, S., Eckerlea, J., and Lowa, T., "Dielectric elastomers: Stretching the capabilities of energy harvesting", in *MRS Bulletin*, **37**, 3, 246-253 (2012).

[100] Duffy, M., and Carroll, D., "Electromagnetic generators for power harvesting", in *Power Electronics Specialists Conference*, **3**, 2075-2081 (2004).

[101] Sebald, G., Guyomar, D., and Agbossou, A., "On thermoelectric and pyroelectric energy harvesting", in *Smart Mater. Struct.*, **18**, 125006 (2009).

[102] Raghunathan, V., Kansal, A., Hsu, J., Friedman, J., Srivastava, M., B., "Design considerations for solar energy harvesting wireless embedded systems", in *IEEEIPSN*, 457-462 (2005).

[103] Khaligh, A.,Onar, O., C., "Energy harvesting: solar, wind, and ocean energy conversion systems", CRC Press ed. (2010).

[104] Parthasarathy, S., K., Ahmed, K., Z., Alexandrov, B., Kumar, S., Mukhopadhyay, S., "Energy efficient active cooling of integrated circuits using autonomous Peltier/Seebeck mode switching of a thermoelectric module", in *Semiconductor Thermal Measurement and Management Symposium (SEMI-THERM)*, 94-99 (2014).

[105] Thermal Electronics Corp., "TEG Power Generator & Thermoelectric Generator", in *espressomilkcooler.com*, retrieved on September 21st November (2014).

[106] SolePower Corp., "How It Works", in *solepowertech.com*, retrieved on September 21st November (2014).

[107] Carroll, C., B., "Energy harvesting eel", *US Patent 6,424,079* (2002).

[108] Robbins, W., P., Morris, D., Marusic, I., Novak, T., O., "Wind-generated electrical energy using flexible piezoelectric materials", in *Proceedings of IMECE2006* (2006).

[109] Wipedia, "Watermill", in *wikipedia.org*, retrieved on September 23st November (2014).

[110] Wipedia, "Windmill", in *wikipedia.org*, retrieved on September 23st November (2014).

[111] Bernstein, B., Hall, D., A., and Trent, H., M., "On the Dynamics of a Bull Whip ", in *J. Acoustical Soc. of America*, **30**, 12, 1112-1115 (1958).

[112] Lācis, U., Brosse, N., Ingremeau, F., Mazzino, A., Lundell, F., Kellay, H. and Bagheri, S., "Passive appendages generate drift through symmetry breaking", *Nature Communications*, **5**, 5310 (2014).

[113] Huang, W.-X., Sung, H., J., "An immersed boundary method for fluid-flexible structure interaction", *Comput. Methods Appl. Mech. Engrg.*, **198**, 2650-2661 (2009).

[114] Zhao, H., Freund, J., B., Moser, R., D., "A fixed-mesh method for incompressible flowstructure systems with finite solid deformations", *Journal of Computational Physics*, **227**, 3114-3140 (2008).

[115] Grigoriadis, D., G., E., Bartzis, J., G., Goulas, A., "LES of the flow past a rectangular cylinder using the immersed boundary concept", *International Journal for Numerical Methods in Fluids*, **41**, 6, 615-632 (2003).

[116] Iaccarino, G., Verzicco, R., "Immersed boundary technique for turbulent flow simulations", *Appl. Mech. Rev.*, **56**, 3, 331-347 (2003).